Betreuer

Technische
Universität
Wien
Vienna University of Technologie

DIPLOMARBEIT

Vortex lattice study of pristine and irradiated niobium diselenide by scanning tunneling microscopy

Ausgeführt am

Atominstitut

der Technischen Universität Wien

unter Anleitung von

Betreuer: Univ.Prof. Dr.phil. Dr.h.c. Harald W. Weber

Assistent: Dipl. Ing. Dr. Martin Zehetmayer

durch

Johannes Hecher

MNr.: 0625419

Steinfeldstraße 42

2731 St. Egyden

Wien, 21. Dezember 2011

Johannes Hecher

Abstract

The goal of this work was to study the so-called vortex lattice in conventional type II superconductors. One very important quantity that is determined by the vortex lattice distribution is the critical current density of a superconductor which is crucial for many technical applications. Therefore a more detailed understanding of the vortex lattice structure and a comparison between theory and experiment are important.

The details of the properties can best be understood by observing the vortex lattice in real space. This was done by *scanning tunneling microscopy*, since it is the only technique which allows detecting single vortices at arbitrary high magnetic field. In order to achieve high statistical significance a large number of about 1000 or more vortices was imaged.

Due to the fact that the vortex lattice structure may depend on the magnetic field, the vortex lattice was measured at different fields for pristine and irradiated $NbSe_2$ single crystals. The neutron irradiation of the single crystals introduces defects in the sample, which may act as pinning centers for the vortices. The main focus was placed on the region, where the macroscopic critical current the irradiated sample shows a second peak at a rather high magnetic field. In this region a highly disordered vortex lattice was observed, while in regions where the macroscopic current vanishes the lattice was found to be rather well ordered in the irradiated sample and close to perfectly ordered in the pristine sample. In this work the variation of the temperature was not an important criterion and thus the temperature at which the measurement was carried out was chosen to be 4.2 K, the boiling point of helium.

Before the measurements started, a control program for the power supply of the magnet of the scanning tunneling microscope had to be programmed, in order to create a computer interface to control the power supply with the computer. An important criterion was to set the charging rate of the power supply automatically to prevent an *overshoot* of the current (i. e. the field).

To analyze the lattice structure various algorithms for determining the exact vortex positions and calculating several order parameters and the corresponding correlation functions and lengths of the vortex system had to be written. With the evaluation of the relative vortex displacement, the Lindemann criterion was investigated to determine the Lindemann number. Additionally the data acquired by the scanning tunneling microscope had to be processed to improve the scan

images, i. e. to get rid of the noise and to increase the contrast of the images.

The control program for the power supply was written in C++ and enables the user to set the desired field and many other parameters (e. g. charging rate or units) with the program instead of a manual input at the power supply. For the processing of the vortex data various filters and algorithms were written in MATLAB.

For the analysis of the vortex lattice, the vortex lattice was imaged for different fields and up to 2000 vortex cores could be found. The comparison between theory and measurement showed generally good agreement.

Zusammenfassung

Das Ziel dieser Arbeit ist die Untersuchung des sogenannten Flussliniengitters in konventionellen Typ II Supraleitern. Eine wichtige Größe, die durch das Flussliniengitter bestimmt wird, ist die kritische Stromdichte, die essenziell für viele technische Anwendungen ist. Daher ist ein detailliertes Verständnis der Struktur des Flussliniengitters und eine Überprüfung bereits existierender Theorien wünschenswert.

Die Eigenschaften des Flussliniengitters können am besten durch direkte Bestimmung der Flusslinienpositionen untersucht werden. Dazu wird die Methode der Rastertunnelmikroskopie angewandt, da diese die einzige Technik ist, die es erlaubt einzelne Flusslinien bei beliebigen Feldern zu detektieren. Um gute statistische Aussagen treffen zu können, soll die Anzahl der Flusslinien pro Messung 1000 oder mehr betragen.

Da die Struktur des Flussliniengitters für verschiedene Felder unterschiedlich sein kann, sollen Messungen bei mehreren Feldern durchgeführt werden. Weiters sollen sowohl bestrahlte als auch unbestrahlte $NbSe_2$ Einkristalle gemessen werden. Nutronenbestrahlung erzeugt Materialdefekte in der Probe, die zur Verankerung der Flusslinien dienen können und somit das Flussliniengitter verändern. Insbesondere sollen die Veränderungen der Gitterstruktur in der sogenannten *second peak* Region der bestrahlten Probe untersucht werden (*fishtail effect*). In dieser Arbeit soll keine Temperaturabhängigkeit überprüft werden, weswegen alle Messungen bei 4.2 K ausgeführt werden (Siedetemperatur von Helium).

Bevor die Messungen begonnen wurden, sollte ein Programm zur Steuerung des *power supply* des Magneten geschrieben werden. Dieses Programm soll die manuelle Eingabe von Parametern ersetzen und in der Lage sein, automatisch die *charging rate* für verschiedene Stromstärke-Intervalle zu setzen, um einen *overshoot* des Stromes und damit des Feldes zu verhindern.

Zur Analyse der Gitterstruktur wurden verschiedene Algorithmen zur Berechnung der Ordnungsparameter und der entsprechenden Korrelationsfunktionen und Längen des Flussliniensystems geschrieben. Mit der Berechnung der relativen Versetzung der Flusslinien, sollte das Lindemann Kriterium untersucht und die Lindemann Zahl bestimmt werden. Zusätzlich sollten die Daten aus der Rastertunnelmikroskopie bearbeitet werden, um die Messbilder zu verbessern, d. h. das Rauschen herauszufiltern und den Kontrast zu erhöhen.

Das Steuerungsprogramm für den *power supply* wurde in C++ geschrieben und ermöglicht es dem Benutzer, das gewünschte Feld und andere Parameter (z. B.

charging rate oder die Messeinheiten) am Computer einzugeben anstatt dies manuell am *power supply* vornehmen zu müssen. Zur Bearbeitung der Flussliniendaten wurden verschiedene Algorithmen in MATLAB geschrieben.

Zur Analyse der Gitterstruktur der Flusslinien wurden Messungen bei verschiedenen Feldern durchgeführt, wo bis zu 2000 Flusslinien gefunden wurden. Der Vergleich von Theorie und Messung zeigte eine meist gute Übereinstimmung.

Table of Contents

1 Superconductivity

The starting point for the discovery of superconductivity was the discussion of the behavior of the electric resistivity R at low temperatures. It was found that the resistivity of some elements (e. g. mercury) disappeared abruptly at a certain temperature. This discovery in 1911, by Kamerlingh Onnes, was the beginning of superconductivity [1].

1.1 The Phenomena of Superconductivity

Shortly after the discovery of a critical transition temperature T_c below which $R = 0$, it was found that superconductors have additional characteristics. Applying high external magnetic fields may suppress superconductivity. The field value above which superconductivity is suppressed is called critical field and specified by $\boldsymbol{H}_c$. Given that it is irrelevant whether the field is applied externally or generated by a current on the surface the critical field is accompanied by a critical current density $\boldsymbol{j}_0$.

Additionally to the critical parameters, further phenomena of superconductors exist, which shall be discussed briefly in this section.*

1.1.1 Meissner Effect

The Meissner effect is the expulsion of a magnetic field from the inside of a superconductor during the transition from the normal conducting to the superconducting state [8]. Below the transition temperature T_c the superconductor behaves like an ideal diamagnet, meaning that no field or screening current enters the superconductor except for a small area of about 10 - 100 nm at the boundaries. The experiment demonstrates that superconductivity is more than just “perfect conductivity”, but a separate thermodynamical phase.

*The content of this chapter is based on [2, 3, 4, 5, 6, 7].

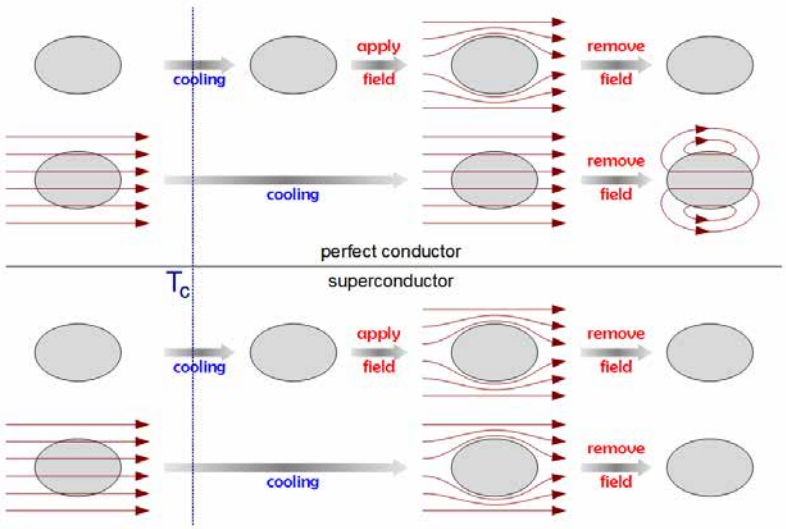

Fig. 1.1.1: Differences of a perfect conductor and a superconductor when cooled below T_c. (Slim arrows indicate an applied field.)

Fig. 1.1.1 shows the difference between superconductivity and perfect conductivity.

If a perfect conductor or a superconductor is cooled beneath T_c in a zero field environment and a field is applied afterwards, for both conductors the statement that no magnetic flux is inside the conductor is valid. Switching off the field recovers the initial state (no magnetic flux inside the material; but with $T < T_c$).

Another possibility is to apply the field before cooling the system. While the field does not change in a perfect conducting system when reaching a temperature lower than T_c, a superconductor screens its interior from the magnetic flux. After removing the field the perfect conductor keeps the field, whereas the superconductor again reaches the initial state.

Due to the fact that the superconductor stays field free at temperatures beneath T_c it can be described by the magnetic susceptibility $\chi = -1$ (Meissner state)

$$\begin{aligned} \vec{B}_{SC} &= \mu_0(\vec{H} + \vec{M}) = 0 \\ \vec{M} &= \chi\vec{H} = -\vec{H} \end{aligned} \tag{1.1.1}$$

where $\boldsymbol{M}$ is the magnetization of the superconductor, $\boldsymbol{H}$ is the magnetic field strength, and $\boldsymbol{B}_{SC}$ is the magnetic induction within the superconductor. The constant μ_0 is the vacuum permeability with the value $4\pi \cdot 10^{-7}\,\mathrm{Vs} \cdot \mathrm{A}^{-1}\mathrm{m}^{-1}$.

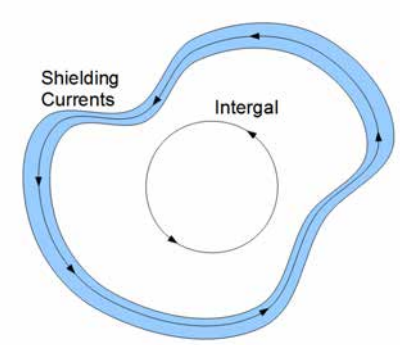

Fig. 1.1.2: Visualization of the line integral needed to calculate the flux quantization. Shielding currents only occur at the border. If the line integral is placed far away from the border the current part of the integral can be neglected.

1.1.2 Flux Quantization

The quantization of the magnetic flux indicates the existence of a coherent state over a macroscopic region, meaning that the wave function must be unique. Therefore the wave function must merge into itself in a closed circle:

$$\begin{aligned} \oint \mathrm{d}\boldsymbol{r} \cdot \frac{1}{\lambda} &= n, \\ \oint \mathrm{d}\boldsymbol{r} \cdot \boldsymbol{p} &= hn, \\ \oint \mathrm{d}\boldsymbol{r} \cdot (m\boldsymbol{v} - q\boldsymbol{A}) &= hn. \end{aligned} \tag{1.1.2}$$

λ is the wavelength, $\boldsymbol{p}$ the canonic momentum, $h = 6.626 \cdot 10^{-34}$ Js Planck's constant and n a natural number. The integral over $m\boldsymbol{v}$ describes a current. Due to the fact that there is no current in a superconductor, except for a small region at the boundaries (see Fig. 1.1.2 and Section 1.2.1) the integral is negligible and the result for the magnetic flux is

$$\Phi_n = \oint \mathrm{d}\boldsymbol{r} \cdot \boldsymbol{A} = -\frac{h}{q} n. \tag{1.1.3}$$

For $n = 1$ the flux is called *magnetic flux quantum* and has the value: $\Phi_0 = 2.07 \cdot 10^{-15}$ Wb. Experiments showed, that the electronic charge is $-2e$, where e is the positive elementary charge, which is a clear indication for the pairing of electrons in superconductors (see Section 1.3.1).

Aside of the so-called type I superconductors (most chemical elements), there exist also the type II superconductors (see Section 1.2.2). Type II superconductors

stay in the Meissner state up to a lower critical field $\boldsymbol{H}_{c1}$, but for larger fields type II superconductors allow the field to penetrate the material in the form of quantized flux vortices, until the upper critical field $\boldsymbol{H}_{c2}$ is reached and the superconductor becomes normal conducting.

1.1.3 Thermodynamics

To specify the thermodynamic properties of superconductors it is most useful to evaluate the free energy density:

$$f = f(0) - \mu_0 \int_0^{\boldsymbol{H}_a} \mathrm{d}\boldsymbol{H} \cdot \boldsymbol{M} \tag{1.1.4}$$

where $f(0)$ shall describe all terms of the free energy density at zero field. Except for a small diamagnetism, the magnetization is independent of the field in the normal conducting state and therefore

$$f_{nc}(\boldsymbol{H}) = f_{nc}(0). \tag{1.1.5}$$

Because a superconductor in the Meissner state is an ideal diamagnet ($\boldsymbol{M} = -\boldsymbol{H}$). The free energy of the superconducting state is

$$f_{sc}(\boldsymbol{H}) = f_{sc}(0) + \mu_0 \int_0^{\boldsymbol{H}_a} \mathrm{d}\boldsymbol{H} \cdot \boldsymbol{H} = f_{sc}(0) + \frac{\mu_0}{2}\boldsymbol{H}_a^2. \tag{1.1.6}$$

Comparing superconducting and normal state at a field $\boldsymbol{H}_c$, where the free energy of both states is equal ($f_{sc}(\boldsymbol{H}_c) = f_{nl}(\boldsymbol{H}_c) = f_{nl}(0)$), leads to

$$\Delta f = f_{sc}(0) - f_{nc}(0) = f_{sc}(\boldsymbol{H}_c) - \frac{\mu_0}{2}\boldsymbol{H}_c^2 - f_{nc}(\boldsymbol{H}_c) = -\frac{\mu_0}{2}\boldsymbol{H}_c^2. \tag{1.1.7}$$

Eq. (1.1.7) shows that the superconducting state is energetically lower than the normal conducting state and so a phase transition is possible. Δf is usually called condensation energy E_c (per unit volume).

In order to describe other thermodynamic variables, F (free energy) is evaluated:

$$\Delta F = \int \mathrm{d}V \cdot \Delta f, \tag{1.1.8}$$

where V is the volume of the sample. With ΔF, thermodynamic variables like

$$S = -\frac{\partial F}{\partial T} \qquad \text{or} \qquad C = T\frac{\partial S}{\partial T} \tag{1.1.9}$$

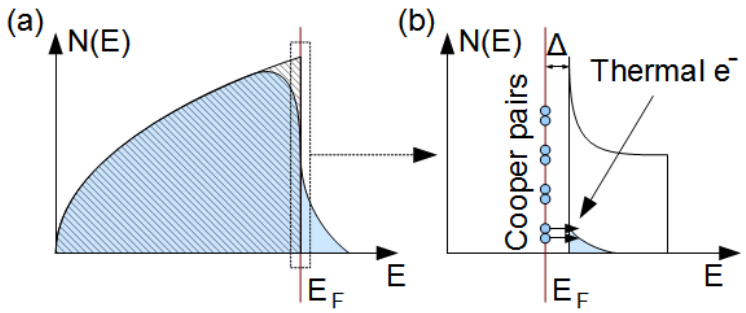

Fig. 1.1.3: Density of states of Cooper pairs (a) end excited particles (after breaking th Cooper pairs) in the superconducting state (b).

are defined, where S is the entropy of the system, which is lower in the superconducting state, meaning that the superconductor is better ordered than the normal conducting material. C is the specific heat. It shows a jump at T_c in zero field and an exponential behavior at low temperatures instead of a linear behavior as in normal conductors. This behavior is a clear indicator of the existence of an energy gap.

1.1.4 The Energy Gap

The energy gap Δ of the superconducting state is located at the Fermi level of the excitation spectrum of superconductors, meaning that excited particles created by destroying a Cooper pair exist within the range of the gap as shown in Fig. 1.1.3. L. Cooper showed that two electrons can gain energy if they condense to a boson like quasi particle and so forming a superconducting phase. In the ground state all electrons are bound to Cooper pairs. To "excite" electrons above the Fermi energy a Cooper pair has to be broken. The energy needed to break a Cooper pair is 2Δ, because two electrons have to overcome the gap (refer also to Section 1.3).

The energy gap has an approximate magnitude of $k_B T_c$ and corresponds to the energy difference between the electrons in the superconducting and normal state. Various methods to measure the existence and size of the gap are known. One of the most successful is tunneling spectroscopy (refer to Section 2.2.2). These measurements also helped to verify the theory on superconductors of Bardeen, Cooper and Schrieffer (Section 1.3.2).

1.2 Phenomenological Models

1.2.1 London Theory

F. and H. London used the classical equation of motion

$$m\frac{\mathrm{d}\boldsymbol{v}}{\mathrm{d}t} = \boldsymbol{F} - m\frac{\boldsymbol{v}}{\tau} \tag{1.2.1}$$

to describe the electronic properties of superconductors [9]. In this equation $\boldsymbol{v}$ denotes the velocity and m the mass of an electron. $\boldsymbol{F}$ is the force that acts on the electron. For the assumption of superconductivity, namely the disappearance of the resistivity, the mean free time for scattering of electrons at atomic lattice ions τ is infinite and the first London equation is gained

$$\frac{\mathrm{d}\boldsymbol{j}}{\mathrm{d}t} = \frac{ne^2}{m}\boldsymbol{E}. \tag{1.2.2}$$

To acquire this solution $\boldsymbol{j} = -en\boldsymbol{v}$ was used and only the electric field part of the force was included ($\boldsymbol{F} = -e\boldsymbol{E}$). The first London equation states that a stationary supercurrent enforces a zero electric field. To account for the magnetic induction part of the force, which describes the Meissner effect, a curl is applied to Eq. (1.2.2)

$$\frac{\mathrm{d}}{\mathrm{d}t}\left(\nabla \times \boldsymbol{j}\right) = \frac{ne^2}{m}\left(\nabla \times \boldsymbol{E}\right), \tag{1.2.3}$$

and subsequently Maxwell's equation $\mathbf{curl}(\boldsymbol{E}) = -\partial\boldsymbol{B}/\partial t$ is used

$$\frac{\mathrm{d}}{\mathrm{d}t}\left(\nabla \times \boldsymbol{j} + \frac{ne^2}{m}\boldsymbol{B}\right) = 0, \tag{1.2.4}$$

which leads to the second London equation

$$\nabla \times \boldsymbol{j} + \frac{ne^2}{m}\boldsymbol{B} = 0, \tag{1.2.5}$$

F. and H. London assumed that the bracket term in Eq. (1.2.4) is zero.

The second London equation describes the penetration of the magnetic induction into the superconductor. This is achieved by inserting Eq. (1.2.5) into Maxwell's equation

$$\nabla \times \boldsymbol{B} = \mu_0\boldsymbol{j} + \frac{\partial \boldsymbol{D}}{\partial t}. \tag{1.2.6}$$

Due to the fact that the electric displacement field $\boldsymbol{D}$ is negligible for low frequencies applying a curl yields

$$\begin{aligned} \nabla \times \nabla \times \boldsymbol{B} &= \mu_0 \nabla \times \boldsymbol{j}, \\ \nabla^2 \boldsymbol{B} &= \frac{\mu_0 n e^2}{m} \boldsymbol{B}, \end{aligned} \tag{1.2.7}$$

where the relations $\nabla \times \nabla \times \boldsymbol{B} = \nabla(\nabla \cdot \boldsymbol{B}) - \nabla^2 \boldsymbol{B}$ and $\nabla \cdot \boldsymbol{B} = 0$ were used.

Eq. (1.2.7) can also be written as

$$\nabla^2 \boldsymbol{B} = \frac{1}{\lambda_\mathrm{L}^2} \boldsymbol{B} \qquad \text{with} \qquad \lambda_\mathrm{L} = \sqrt{\frac{m}{\mu_0 n e^2}}, \tag{1.2.8}$$

with λ_L the London penetration depth. The London theory shows, that any external magnetic induction $\boldsymbol{B}$ is screened at the boundaries of a superconducting material within a surface layer of thickness λ_L (cf. Fig. 1.2.1).

1.2.2 Ginzburg-Landau Theory

In Landau's theory of second-order phase transitions the free energy density f is expanded in powers of a complex order parameter ψ. This theory is only valid in the vicinity of the transition. The free energy density in Landau's theory is given by

$$f_0 = f_\mathrm{nc} + \alpha |\psi|^2 + \frac{\beta}{2} |\psi|^4, \tag{1.2.9}$$

and f_nc is the free energy density of the normal conducting state. α and β are phenomenological parameters. To describe spatial inhomogeneities and magnetic effects Ginzburg introduced an additional term of the form of a kinetic energy

$$\boldsymbol{E} = \frac{\boldsymbol{p}^2}{2m} \leftrightarrow \boldsymbol{p} = -\mathrm{i}\hbar\nabla - q\boldsymbol{A}(\boldsymbol{r}), \tag{1.2.10}$$

thus modifying the Landau theory to

$$f = f_\mathrm{nc} + \alpha |\psi|^2 + \frac{\beta}{2} |\psi|^4 + \frac{1}{2m_\mathrm{q}} \left| \left(-\mathrm{i}\hbar\nabla - q\boldsymbol{A}(\boldsymbol{r})\right) \psi \right|^2 + \frac{1}{2\mu_0} \boldsymbol{B}^2(\boldsymbol{r}), \tag{1.2.11}$$

where the last term refers to the result of Section 1.1.3. With this equation Ginzburg was able to describe superconductivity in a phenomenological way [10]. By minimizing the free energy with respect to fluctuations of the order parameter, an

equation similar to a time-independent Schrödinger equation is reached

$$\frac{\partial f}{\partial \psi^*} = \alpha\psi + \frac{\beta}{2}|\psi|^2\psi + \frac{1}{2m_\mathrm{q}}\left(-\mathrm{i}\,\hbar\nabla - q\boldsymbol{A}(\boldsymbol{r})\right)^2\psi = 0 \tag{1.2.12}$$

in addition a minimization with respect to the vector potential leads to

$$\frac{\partial f}{\partial \boldsymbol{A}} = \frac{q\hbar}{2m_\mathrm{q}\,\mathrm{i}}\left(\psi^*\,\nabla\psi - \psi\nabla\psi^*\right) - \frac{q}{2m_\mathrm{q}}|\psi|^2\boldsymbol{A}(\boldsymbol{r}) = \boldsymbol{j} \tag{1.2.13}$$

which provides a quantum mechanical current density that describes the superconducting current.

With these so-called Ginzburg-Landau equations two characteristic lengths can be found. One is the penetration depth (see Section 1.2.1)

$$\lambda = \sqrt{\frac{m_\mathrm{q}}{q^2\mu_0|\psi_0|^2}}. \tag{1.2.14}$$

with ψ_0 the equilibrium value of the order parameter in the absence of an electromagnetic field. The second length is the Ginzburg-Landau coherence length

$$\xi = \frac{\hbar}{\sqrt{2m_\mathrm{q}|\alpha|}}. \tag{1.2.15}$$

While λ specifies the characteristic decay of an external magnetic field in the superconductor, ξ describes the increase of the order parameter from the surface into the superconductor (shown in Fig. 1.2.1).

The ratio of those two characteristic lengths

$$\kappa = \frac{\lambda}{\xi} \tag{1.2.16}$$

is the Ginzburg-Landau parameter. If this parameter has a value lower than $1/\sqrt{2}$ the surface energy is positive, meaning that energy is necessary to create a boundary surface between the normal conducting and superconducting phase. Consequently the superconductor will try to have as few boundary surfaces as possible. Superconductors that behave in such a way are refered to as type I superconductors. On the other hand, if κ is greater than $1/\sqrt{2}$ the surface energy is negative and the superconductor may form boundary surfaces, resulting in a mixed state, where magnetic flux penetrates the material ($\boldsymbol{H} > \boldsymbol{H}_{\mathrm{c}1}$). These superconductors are called type II superconductors.

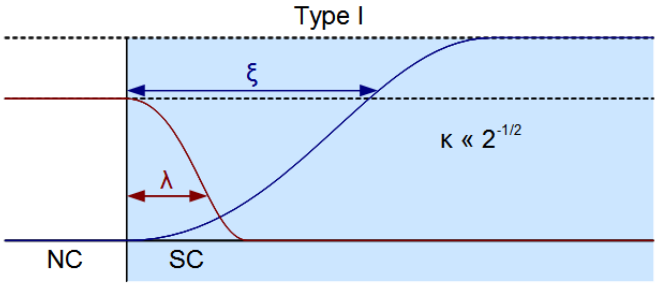

(a) Type I

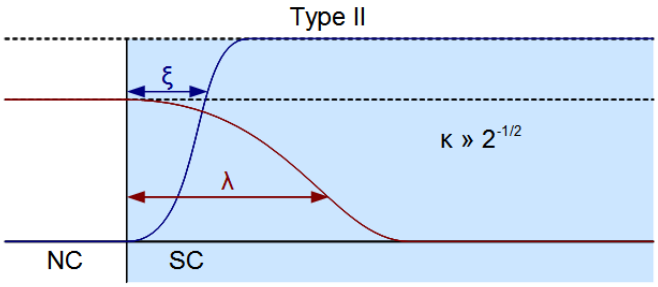

(b) Type II

Fig. 1.2.1: Difference between type I and type II superconductors.

In type II superconductors the (quantized) magnetic flux lines that penetrate the material are called flux vortices or simply vortices. The core of a vortex is normal conducting and surrounded by electric shielding currents. Tab. 1.2.1 shows the relation between κ and the type of a superconductor, as well as between the surface energy σ and the type of superconductors.

Tab. 1.2.1: Conditions that have to be met for the different superconductor types.

$\kappa < 1/\sqrt{2}$, $\sigma > 0$	no flux lines develop	→ type I SC
$\kappa > 1/\sqrt{2}$, $\sigma < 0$	development of flux lines	→ type II SC

The Ginzburg-Landau equations also show that the phase angle of the superconducting wave function of the Cooper pairs (see Section 1.3.1) is constant in the whole space (when $\boldsymbol{B} = 0$). This identifies the superconducting state as a coherent state. The resulting phase coherence is the main attribute that defines superconductivity.

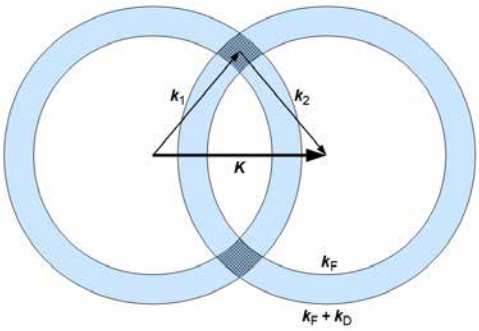

Fig. 1.3.1: Scheme of the effective electron-electron correlation. The overlapping parts are the areas where an interaction is possible.

1.3 Microscopic Theory of Superconductivity

1.3.1 Cooper problem

L. Cooper showed that two fermions can form a bound state, even if the attraction between the fermions is very weak [11].

A pair of fermions shall be able to interact close to a Fermi sphere mediated by phonons even in the presence of the screened Coulomb field. To take the vibrations of the lattice into account the Debye model is used, which assumes harmonic behavior of the oscillating lattice ions with a maximum angular frequency ω_D.

Cooper considered a Fermi gas in its ground state, where only two interacting electrons are inserted above the Fermi energy ε_F. These electrons shall not interact with the ground state so consequently states with $\varepsilon < \varepsilon_\mathrm{F}$ are forbidden for the electron pair. If an interaction between the two electrons occurs (through the potential V) an exchange of the momentum results in

$$|\boldsymbol{k}_1, \boldsymbol{k}_2\rangle \rightarrow |\boldsymbol{k}_1 + \boldsymbol{q}, \boldsymbol{k}_2 - \boldsymbol{q}\rangle \tag{1.3.1}$$

where the total momentum $\boldsymbol{K} = \boldsymbol{k}_1 + \boldsymbol{k}_2$ is conserved. Due to the fact that the momentum exchange is based on the electron phonon interaction the maximum of the transferable momentum is defined by $\boldsymbol{k}_\mathrm{D}$. Therefore a momentum exchange is only possible in a small region of the size $\boldsymbol{k}_\mathrm{D}$ above the Fermi level as is shown in Fig. 1.3.1. As is easily seen the probability of an interaction (overlapping parts) is largest for the case that $\boldsymbol{K} = 0$, or in other words $\boldsymbol{k}_1 = -\boldsymbol{k}_2$. Electrons with these attributes are called Cooper pairs.

Because the system is specified in a quantum mechanical way and the treated particles are fermions the total wave function has to be antisymmetric. For Cooper pairs the total spin is usually zero (singlet state), i. e. the spins of the electrons are opposing:

$$|1\rangle \to |\boldsymbol{k}, \uparrow\rangle \qquad \text{and} \qquad |2\rangle \to |-\boldsymbol{k}, \downarrow\rangle \tag{1.3.2}$$

1.3.2 Bardeen-Cooper-Schrieffer Theory

In the year 1957 Bardeen, Cooper and Schrieffer introduced their "Theory of Superconductivity" which came to be named the BCS theory. The theory is based on the interaction between electrons resulting from the exchange of virtual phonons [12]. The emission of a virtual phonon can be interpreted as a displacement of the ionic lattice of a crystal initiated by the Coulomb interaction with an electron. The displacement of the lattice results in a polarization of the lattice, i. e. the induction of a phonon. Owing to their greater mass the ions oscillate relatively slowly compared to the velocity of the electrons. When an electron gets in the vicinity of the polarization (phonon) the electron can "absorb" the polarization, which results in a change of the momentum and energy.

The Hamiltonian for the electrons is expressed by

$$\hat{\mathcal{H}}_{\mathrm{BCS}} = \sum_{k} (\varepsilon_k - \mu)(\hat{c}^{+}_{k\uparrow}\hat{c}_{k\uparrow} + \hat{c}^{+}_{-k\downarrow}\hat{c}_{-k\downarrow}) - \sum_{k,k'} \hat{c}^{+}_{k\uparrow}\hat{c}^{+}_{-k\downarrow} V_{kk'} \hat{c}_{k'\uparrow}\hat{c}_{-k'\downarrow}, \tag{1.3.3}$$

where the findings of Section 1.3.1 are already taken into account. The operators $\hat{c}^{+}$ and $\hat{c}$ are the fermion creation and annihilation operators and $V_{kk'}$ is the matrix element for effective electron-electron interaction (via phonons). Arrows give the spin of the particle where $\downarrow$ and $\uparrow$ refer to the values $s = -1/2$ and $s = 1/2$ respectively. μ is the chemical potential and ε_k the kinetic energy of the fermions. The influence of the phonons is only apparent through the assumption of a maximal transferable phonon energy.

The BCS-Hamiltonian is not analytically solvable and some simplifications are necessary (e.g. mean field approximation or a test function). Still the BCS theory is able to describe the phenomena of Section 1.1 very well. In the BCS ground state all electrons are condensed into Cooper pairs. The occupation probability of the BCS ground state and a normal conducting system is shown in Fig. 1.3.2.

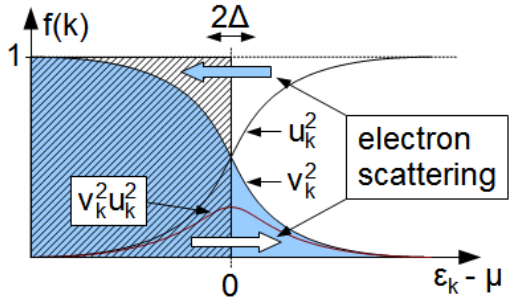

Fig. 1.3.2: Occupation probability of the BCS ground state (v_k^2) and a normal conducting system (hatched area). u_k^2 is the probability that the states $|\boldsymbol{k},\uparrow\rangle$ and $|-\boldsymbol{k},\downarrow\rangle$ are unoccupied. The probability of Cooper pair scattering is given by $v_k^2 u_{k'}^2$, i. e. the scattering from states $|-\boldsymbol{k}\rangle$ (occupied states) to $|-\boldsymbol{k}'\rangle$ (unoccupied states).

1.4 The Vortex Lattice

When a magnetic field is applied to a type II superconductor the magnetic flux may penetrate the material with quantized tubes, the so-called flux vortices (hereafter vortices; see Fig. 1.4.1). The type II superconductor excludes the penetration up to a lower critical field H_{c1}. Then the vortices enter the material. This process continues until an upper critical field H_{c2} is reached.

A vortex is roughly a cylindrical structure parallel to the field. The term "cylindrical" may be misleading, because the transition from the superconducting phase to the normal conducting phase is actually continuous. The center of this structure is normal conducting. The normal conducting core gradually merges with the superconducting phase until finally only the superconducting phase remains (cf. Fig. 1.2.1). If the field is raised, the vortices get closer to each other and the normal conducting cores start to overlap as can be seen in Fig. 1.4.2(a). The radius of the vortex core has the magnitude of some nanometers ($\sim \xi$). In the transition region, circulating electric currents "shield" the superconducting parts. At the center of the vortex, the density of superconducting particles (Cooper pairs; order parameter in the Ginzburg-Landau theory) vanishes, whereas it is maximal in the superconducting phase. The opposite is true for the field and the current density, which approach zero in the superconducting region and have a maximum in the vortex center.

A vortex is not formed at an arbitrary position in the superconductor, but at

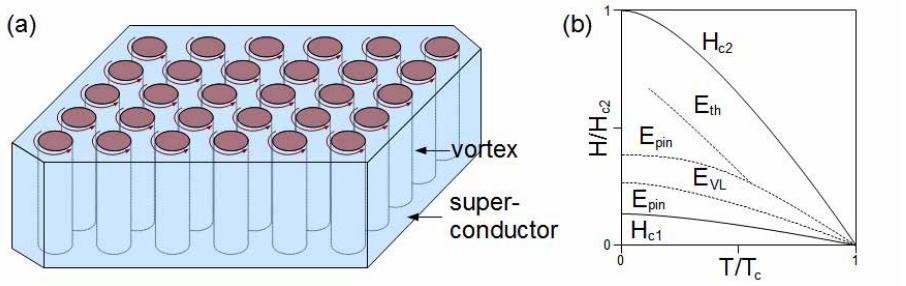

Fig. 1.4.1: Image (a): Hexagonal structure of the vortex lattice in a type II superconductor. Note that the currents around the vortices have the same orientation for every vortex.
Image (b): Phase diagram of a type II superconductor with the critical fields H_{c1} and H_{c2} (solid lines). The diagram is separated into different regions where different pinning energies predominate.

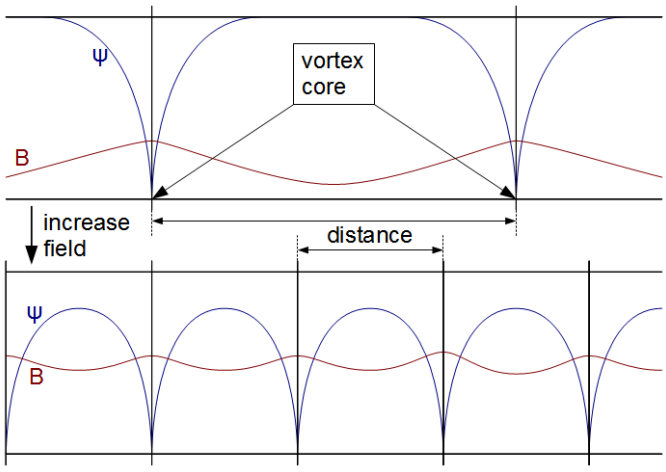

Fig. 1.4.2: Schematic picture of the overlap of vortices when the field is increased. B indicates the field dependence and ψ indicates the dependence of the order parameter.

the boundary of the material. The occurrence of a shielding current around the vortex is the reason for the repulsive interaction between different vortices, thus by increasing the field more vortices will start to penetrate the superconductor near the boundaries and consequently "push" the vortices, which are already inside the material, further inside.

If a superconductor is very homogeneous (i. e. without defects) the vortices will build a hexagonal lattice due to the earlier mentioned repulsive interaction. A theoretical nearest neighbor distance, dependent on B, is given by

$$a_0 = \sqrt{\frac{2}{\sqrt{3}}\frac{\Phi_0}{B}}, \tag{1.4.1}$$

where Φ_0 is the magnetic flux quantum of Eq. (1.1.3).

Due to the fact that flux lines also interact with the inhomogeneities of the material, e. g. the defects, an additional force prevents the flux lines to move freely throughout the sample. This can be understood if the defects in the material are assumed to be normal conducting. The superconductor looses condensation energy for every normal conducting area (i. e. vortex cores and defects). Accordingly, a superconductor gains energy if a vortex is at the position of a normal conducting defect, because the loss of condensation energy of the defect is saved.

An easy way to illustrate the penetration of vortices with changing applied field is the Bean model shown in Fig. 1.5.1.

The figure shows the graphical interpretation of the Bean model for $T < T_c$. H^* is the field at which the first vortex (i. e. the flux front) reaches the center of the bulk. The value of H^* depends on the gradient of the field, i. e. the critical current density, which is assumed to be linear in the Bean model.

If the field is increased, the pinning energy works against the penetration of the vortices. When the field is decreased the pinning energy works against the leaving of the vortices. The lower images show the remaining flux density gradients.

The vortices only totally leave the bulk, if the temperature is increased above T_c. On the other hand, if a field is applied at $T > T_c$ (Fig. 1.5.1(b)) the pinning forces have no effect. The field penetrates the bulk uniformly. Cooling the type II superconductor below T_c and turning off the field results in approximately the same states as shown in Fig. 1.5.1(a).

Various energies are responsible for the vortex matter behavior in a superconductor. Each energy dominates in a distinct area of the phase diagram (see Fig. 1.4.2(b)). The term E_{pin} describes the field and temperature part near the lower critical field.

Here the mean distance of the separate vortices is large so that the repulsive interaction of the local currents around the vortices is small. Every vortex can arrange itself in such a way, that the pinning centers are optimally occupied. This leads to a disordered lattice, in which the individual shielding currents are not extinguished by each other, as is the case in a perfect lattice. Hence, a macroscopic current, which is proportional to the vortex density gradient, can flow.

The occurrence of E_{pin} at higher fields results from the same fact, although the vortices are much closer together. The macroscopic effect that is observed in this region is again a macroscopic current, known as the second peak or fishtail effect.

In the area where the conventional hexagonal lattice predominates (E_{VL}) the repulsion of the vortices among each other compels them to form a lattice with maximized distance, namely a hexagonal arrangement. In the fully ordered alignment no current exists, because the local currents extinguish each other.

The thermal energy (E_{th}) leads to fluctuations around the equilibrium of the vortex position.

1.5 Critical Current Density $\boldsymbol{j_c}$ and Peak Effect

To describe history effects in type II superconductors the model of a "critical state" was introduced. This model was first proposed by H. London and Bean. The magnetization in a superconductor is described by a single parameter, the "critical current density" $\boldsymbol{j}_{\mathrm{c}}$. The critical current density is induced at local inhomogeneities in the material by vortex pinning. The critical state or $\boldsymbol{j}_{\mathrm{c}}$ is achieved at a certain field, if the Lorentz force $\boldsymbol{F}_{\mathrm{L}}$ working on the vortices is equal to the pinning force $\boldsymbol{F}_{\mathrm{V}}$ of the inhomogeneities in the crystal. In other words: The critical state is an equilibrium of Lorentz and pinning forces.

The determination of $\boldsymbol{j}_{\mathrm{c}}$ is defined by the integral

$$\boldsymbol{m}_{\mathrm{irr}} = -\frac{1}{2}\int \mathrm{d}^3 r \boldsymbol{j} \times \boldsymbol{r}. \tag{1.5.1}$$

Here m_{irr} is the irreversible magnetic moment. It is assumed, that the current density is constant in the whole sample (Bean model). With these simplifications the absolute value of the current density can be written outside the integral so that only the spatial part of $\boldsymbol{j}$ is inside the integral. If the geometry of the sample is known, the integral can be solved for $\boldsymbol{j}$. For example, if the geometry is a cuboid

the solution is

$$|\boldsymbol{j}_c| = \frac{|\boldsymbol{m}_{irr}|}{V} \frac{4}{b\left(1 - \frac{b}{3a}\right)} \quad \text{with} \quad a \geq b, \tag{1.5.2}$$

where a and b are the dimensions perpendicular to the field direction and V the volume of the sample.

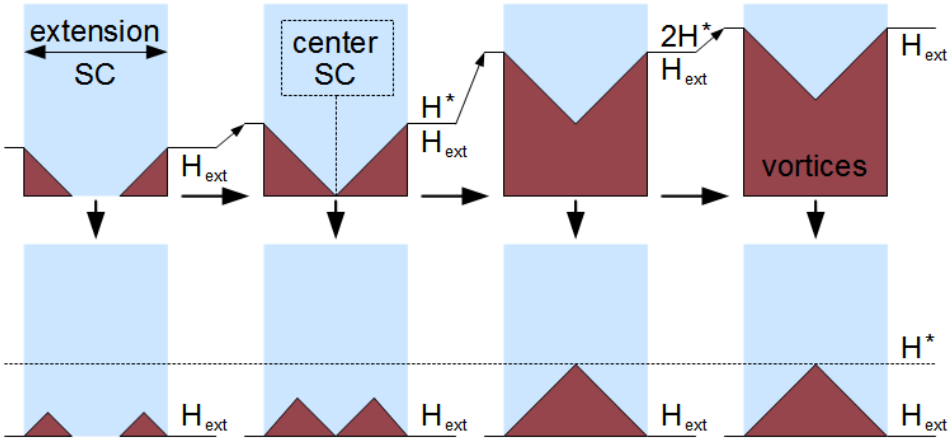

(a) Graphical interpretation of the Bean model for $T < T_c$.

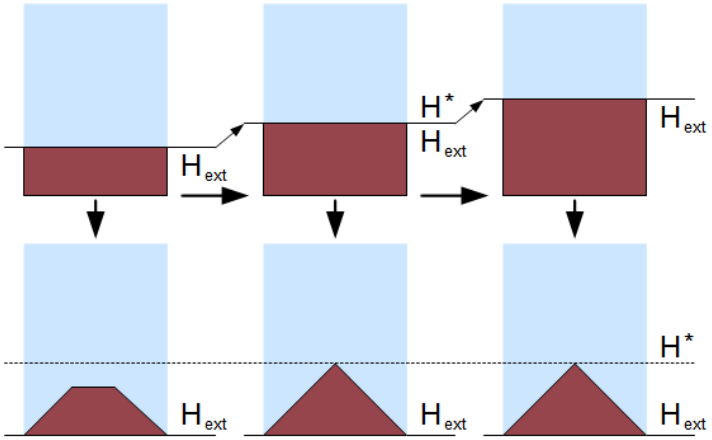

(b) Bean model for field cooling.

Fig. 1.5.1: Bean model for two cases. In the upper part of both images the external field $\boldsymbol{H}_{\text{ext}}$ is gradually increased from the left to the right. The arrows from top to bottom indicate the deactivation of $\boldsymbol{H}_{\text{ext}}$. The superconducting bulk is indicated by the x-axis and the density of vortices is given by the z-axis.

2 Scanning Tunneling Microscopy

The Scanning Tunneling Microscope (STM)* was invented by G. Binnig and H. Rohrer in 1982 [16, 17], which earned them the Nobel prize for physics in 1986. The original idea was not to build a microscope but to perform spectroscopy locally on a surface. The operating STM resembles the stylus profilometry, where a diamond stylus is in contact with a sample while it is moved across the surface. In the STM instead of a tip in mechanical contact to a surface, a small gap of a few nm between tip and sample is maintained. This gap is maintained by keeping the electron tunneling current between sample and tip at a constant value.

Originally, the Abrikosov flux lattices was observed by Bitter patterns, where fine magnetic particles are deposited on a superconductor to mark the position of the flux lines. That technique is constrained to relatively low magnetic fields, since the vortices get to close to each other to be distinguishable at higher fields (because of the overlap of the magnetic field, see Fig. 1.4.2). The magnetic particles are attracted by places on the surface with higher magnetic fields and "condensate" in those regions. If the sample is analyzed in an electron microscope, the regions where the vortex cores had been (i. e. the area with the highest field), can be clearly seen, because the particles are attached to the surface by Van der Waals forces even after the superconductor is heated to room temperature.

Another possibility is neutron diffraction which is based on the interaction of the magnetic moment of neutrons and the spatial variation of the magnetic field. Due to the fact, that the distances in the vortex lattice are much larger than the distances in the crystal structure, neutrons with a long wave length and small angle scattering arrangements are necessary. The STM, with the more direct technique of tunneling into states in the region of the superconducting gap, allows observation of the lattice over the full range of magnetic fields [18].

Due to the large variety of sample-tip interactions, many similar microscope types have been invented, such as the magnetic force microscope (MFM) or the

*The content of this chapter is based on [13, 14, 15, 6].

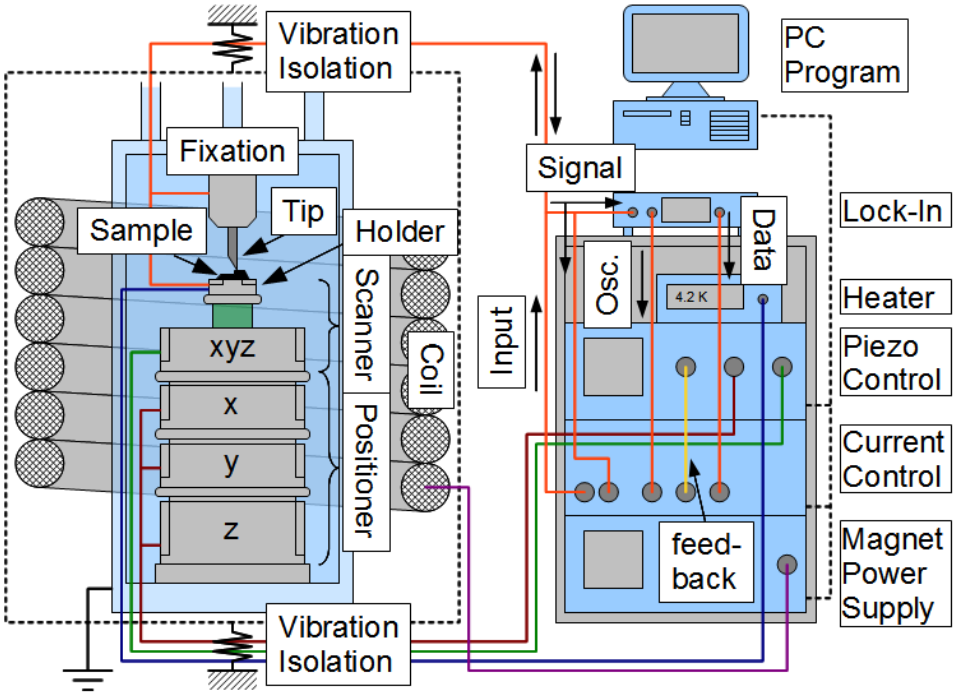

Fig. 2.0.1: Drawing of an STM with the control units. To the left of the image the components which are inserted into the cryostat can be seen. The right part shows the main instruments of the control system.

Atomic Force Microscope (AFM). In the AFM instrument, the gap is controlled through the atomic force between sample and tip. While the use of an STM is restricted to conducting samples, the AFM even works on insulating surfaces.

Instruments based on the interaction between sample and tip do not map the actual topography of the surface. The STM, for example, scans the density of states (DOS) which may differ from the real geometric topography.

Fig. 2.0.1 shows the basic layout of an STM. The whole instrument is controlled by a computer interface. The positioners are used for a course approach (see also Section 3.2.1). With the computer interface the tunneling current is set for the measurement (*constant current* mode). Through a feedback system this current is kept at a constant level by adjusting the z-axis deflection of the scanner independent of the xy scanning process (this is not valid for the *constant distance* mode; see Section 2.1 and 2.1.2). In this work, the STM scanner adjusts the sample when scanning and the tip is fixed above the sample so it cannot be moved once it is put

into the holder.

The sample is glued onto a sample holder. Liquid silver past is used as glue. Due to its conducting properties which are essential, because the current has to flow through the sample to the sample holder and from the sample holder back to the control system. The sample holder includes also a heater to permit measurements at different temperatures and a temperature sensor.

The cryostat of the STM has to be isolated from vibrations, otherwise atomic resolution would not be possible, because even the slightest noise introduces small deflections to the tip, or the sample.

For spectroscopic measurements a lock-in amplifier is connected to the system. First, the lock-in amplifier superimposes a small oscillating current with a defined frequency. The output signal from the current is reverted to the lock-in amplifier, from which the data is acquired.

2.1 Basic Concepts

The basic principle of an STM is the interaction between the scanning probe and the sample. A probe tip, usually made of W or (like in our case) of Pt-Ir alloy, is attached to a piezoelectric scanner. This scanner in combination with a coarse (piezoelectric) positioner is used to bring the tip within about a nanometer to the sample surface. At this distance the electron wavefunctions of tip and surface overlap and a finite tunneling conductance is generated (cf. Section 2.1.3, 2.1.4 and 2.2.1).

In scanning tunneling microscopy a small bias voltage is applied, thus electrons may tunnel from tip to sample (or in the reverse direction depending on the voltage) and a tunneling current is generated as shown in Fig. 2.1.4.

The most widely used convention for the polarity of the bias voltage is that the tip is virtually grounded. The bias voltage is the sample voltage. If the sample voltage is positive, the electrons are tunneling from the occupied states of the tip to the empty states of the sample. If the voltage is negative, the electrons are tunneling from the sample to the tip. The tunneling current changes rapidly as a function of the distance in the vicinity of the surface (see Eq. (2.1.5)) and therefore provides a very sensitive indicator of the tip-sample distance.

Two methods for measuring the surface topography by STM can be distinguished: *constant current* and *constant distance* mode. The first method uses an electronic feedback system to keep the tip-sample distance constant. The feedback loop

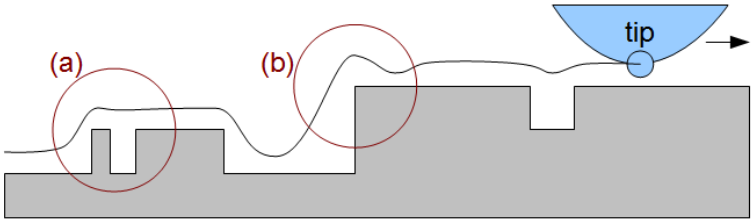

Fig. 2.1.1: Resolution limits of STM. Circle (a) shows that if the tip radius is too large small gaps on the surface can not be resolved. Circle (b) shows the overshoot of the tip if a step in the surface is too steep.

responds by moving the tip normal to the surface (z-axis), thereby tracing the surface topography at constant current, i. e. at a constant distance. The resulting adjustment of the tip position is monitored, which provides the surface topography (i. e. the z-deflection of the scanner as a function of x and y). In the other method the tip is moved while the z-position is not adjusted to the surface. Therefore, the detected tunneling current varies depending on the distance, i. e. it gets stronger when the distance is smaller and a weaker current when the distance is greater. Monitoring the current while scanning laterally results again in a surface topography. The disadvantage of this method is the risk of accidentally crashing into the sample or the distance becoming too large [19].

The resolution of an STM is limited, among other things, by the geometrical shape of the probe tip. If the sample has a step (or peek) on the surface with walls steeper than the opening angle of the tip, then the shape of the step will be smeared out. Holes with a width smaller than the tip radius are also blurred and not imaged at all if the hole is much smaller than the tip radius (see Fig. 2.1.1). Additionally, image artifacts can occur if the tip has two separate tips at the end rather than a single atom. This leads to “double-tip imaging”, a situation in which both tips contribute to the tunneling. To achieve atomic resolution, vibration isolation is essential.

2.1.1 Piezoelectric Positioning

Since the tip needs to be moved over large distances, it is necessary to use a coarse and a fine positioner. The fine positioner is also used as a scanner. Both are usually made of a piezo crystal or a piezo ceramic material (in the following referred to as piezo).

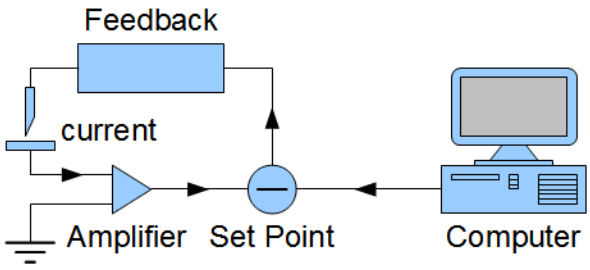

Fig. 2.1.2: Electronic circuit for measuring in the constant current mode.

The piezoelectric effect is a linear electromechanical interaction between the mechanical and the electrical state in crystalline materials and usually reversible. A material with no inversion symmetry generates an electric voltage when the internal electrical charges are displaced by an external force. The opposite effect is called reverse piezoelectric effect. In this case an applied electrical field results in a mechanical deformation of the crystal.

The coarse positioner of our instrument consists of three separated, orthogonal piezos, whereas the fine positioner is a tube scanner. A tube scanner is a piezo-cylinder that is covered with electrodes inside and outside. The outer electrode is divided into four symmetric sectors. To initiate a deflection in xy-direction a voltage is applied to the two opposite electrodes. A deflection in z-direction is generated by applying a voltage between the inner and the outer electrode.

2.1.2 Electronic Circuit

A bias voltage between tip and sample causes electrons to tunnel through the barrier. The tunneling current is in the range from pA to nA and is converted into a voltage by a current amplifier. The output of the amplifier is compared with a predetermined voltage which is used as a reference current. The error signal of this comparison is passed on to a feedback loop, which is designed to keep the tunneling current constant during the scanning process. Thus the phase of the amplifier is chosen to provide a negative feedback: if the absolute value of the tunneling current is larger than the reference value, then the voltage applied to the z-piezo withdraws the tip from the sample surface, and *vice versa*.

Care has to be taken to keep the noise to signal ratio on a low level. Also the response time of the feedback has to be minimized without loosing accuracy. To

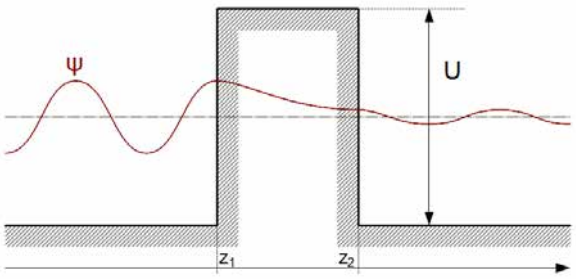

Fig. 2.1.3: Potential barrier.

achieve atomic resolution the vibration isolation is essential. This is realized by making the STM as rigid as possible and reducing the influence of environmental vibrations.

2.1.3 Tunneling Effect

In a simplified case the barrier between sample and tip is assumed to be a rectangular barrier as shown in Fig. 2.1.3. The corresponding Schrödinger equation is given by:

$$\left(-\frac{\hbar^2}{2m}\frac{\partial^2}{\partial z^2} + U(z)\right)\psi(z) = E\psi(z), \tag{2.1.1}$$

where the potential barrier $U(z) = 0$ for $z < z_1$ and $z > z_2$, and $U(z) > 0$ for $z_1 < z < z_2$. E is the eigenvalue of the spatial wavefunction $\psi(z)$ [20]. To solve this problem the wavefunction is separated into three parts:

$$\begin{aligned}
\psi_{\mathrm{I}} &= A_{\mathrm{I}}\,\mathrm{e}^{\mathrm{i}kz} + B_{\mathrm{I}}\,\mathrm{e}^{-\mathrm{i}kz} && \text{for} && z < z_1,\\
\psi_{\mathrm{II}} &= A_{\mathrm{II}}\,\mathrm{e}^{\kappa z} + B_{\mathrm{II}}\,\mathrm{e}^{-\kappa z} && \text{for} && z_1 < z < z_2,\\
\psi_{\mathrm{III}} &= A_{\mathrm{III}}\,\mathrm{e}^{\mathrm{i}kz} + B_{\mathrm{III}}\,\mathrm{e}^{-\mathrm{i}kz} && \text{for} && z_2 < z.
\end{aligned} \tag{2.1.2}$$

where k refers to a traveling wave solution if $E > U(z)$. In case that $E < U(z)$, k is replaced by κ, which quantifies the decay of the wave inside the barrier:

$$\begin{aligned}
k &= \frac{1}{\hbar}\sqrt{2m(E - U(z))}\\
\kappa = \mathrm{i}\,k &= \frac{1}{\hbar}\sqrt{2m(U(z) - E)}.
\end{aligned} \tag{2.1.3}$$

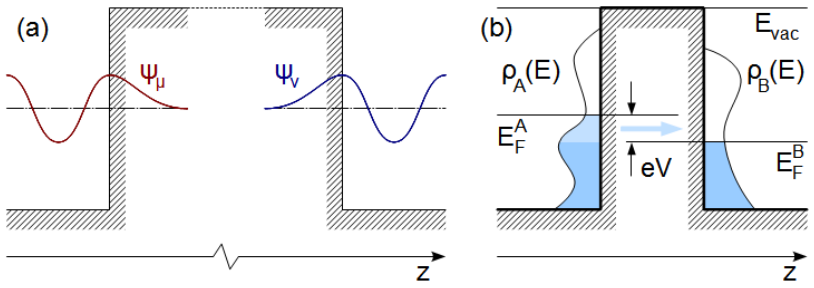

Fig. 2.1.4: The Bardeen tunneling theory in one dimension.

m is the mass of the particle and $\hbar = 1.05 \cdot 10^{-34}$ Js (see also Section 2.1.4). The square of the wave function can be interpreted as a current of particles traveling in $+z$-direction (or *vice versa*) and thus A_{III} is zero, because no particles travel in $-z$-direction in this part (*vice versa*: $B_I = 0$). With the boundary conditions:

$$\begin{aligned} \psi_{\text{I}}(z_1) &= \psi_{\text{II}}(z_1), \qquad \psi_{\text{II}}(z_2) = \psi_{\text{III}}(z_2) \\ \psi'_{\text{I}}(z_1) &= \psi'_{\text{II}}(z_1), \qquad \psi'_{\text{II}}(z_2) = \psi'_{\text{III}}(z_2) \end{aligned} \tag{2.1.4}$$

the Schrödinger equation can be solved (ψ' denotes the derivative). The probability of finding an electron behind the barrier of width $d = |z_2 - z_1|$ is

$$P(d) \propto \mathrm{e}^{-2\kappa d}. \tag{2.1.5}$$

For the STM d characterizes the distance between sample and tip.

2.1.4 Quantum-Mechanical Concept of Tunneling in an STM

A simplified tunneling junction is shown in Fig. 2.1.4. When the two electrodes (sample and tip) are far apart (Fig. 2.1.4(a)), the wave function of electrode A satisfies the Schrödinger equation: [13]

$$\hat{\mathcal{H}}_{\text{A}} \Psi(\boldsymbol{r}, t) = \left(-\frac{\hbar^2}{2m} \nabla^2 + U_{\text{A}} \right) \Psi(\boldsymbol{r}, t) = -\mathrm{i}\hbar \frac{\partial}{\partial t} \Psi(z, t), \tag{2.1.6}$$

with

$$\Psi(\boldsymbol{r}, t) = \psi_\mu(\boldsymbol{r})\, \mathrm{e}^{-\mathrm{i} E_\mu t/\hbar}, \tag{2.1.7}$$

where the spatial wave function $\psi_\mu(\boldsymbol{r})$ has the same structure as in Eq. (2.1.2). Similarly, the Schrödinger equation for electrode B is

$$\hat{\mathcal{H}}_\mathrm{B}\,\Psi(\boldsymbol{r},t) = \left(-\frac{\hbar^2}{2m}\nabla^2 + U_\mathrm{B}\right)\Psi(\boldsymbol{r},t) = -\mathrm{i}\,\hbar\frac{\partial}{\partial t}\Psi(z,t), \tag{2.1.8}$$

and the state function is

$$\Psi(\boldsymbol{r},t) = \psi_\nu(\boldsymbol{r})\,\mathrm{e}^{-\mathrm{i}\,E_\nu t/\hbar}\,. \tag{2.1.9}$$

In the space between the electrodes, the wave functions of both decay into the vacuum. Due to the fact, that the electrodes are far apart it is assumed that $\psi_\mu = 0$ in the vicinity of electrode B and $\psi_\nu = 0$ in the vicinity of electrode A. Thus, instead of treating the combined surface-tip system as one quantum mechanical system, the Bardeen approach assumes the electronic structures of the two to be independent.

The method is based on the following assumptions: [21]

1. the surface-tip interactions are very weak,
2. the electron-electron interactions can be neglected,
3. the occupation probabilities of the surface and the STM tip are independent from each other and do not change during tunneling, and
4. the eigenstates of the two electrodes are approximately orthogonal.

When bringing the two electrodes together these assumptions allow to assume the following single-electron Hamiltonian:

$$\hat{\mathcal{H}} = \hat{\mathcal{H}}_\mathrm{A} + \hat{\mathcal{H}}_\mathrm{B} + \hat{\mathcal{H}}_\mathrm{T}\,. \tag{2.1.10}$$

$\hat{\mathcal{H}}_\mathrm{T}$ is called the "transfer Hamiltonian" which describes the transfer (tunneling) of electrons. The probability of an electron in the state ψ_μ at E_μ to tunnel into the state ψ_ν with E_ν is given by Fermi's Golden Rule

$$p_\mu = \frac{2\pi}{\hbar}\sum_\nu |M_{\mu\nu}|^2\delta(E_\mu - E_\nu) \tag{2.1.11}$$

The tunneling matrix $M_{\mu\nu}$ can be written as:

$$M_{\mu\nu} = \frac{\hbar}{2m}\int_\Omega \mathrm{d}\boldsymbol{S}\cdot(\psi_\mu\nabla\psi_\nu^* - \psi_\nu^*\nabla\psi_\mu). \tag{2.1.12}$$

Here, Ω represents the enclosed surface surrounding the STM tip. In practice it can be replaced by the interface between the two electrodes. Taking occupation probabilities into account, Bardeen showed that the tunneling current between two electrodes separated by an insulator is given by [22]

(2.1.13)
$$I = \frac{4\pi e}{\hbar} \int_{-\infty}^{\infty} \mathrm{d}\varepsilon \cdot [f(E_\mathrm{F} - eV + \varepsilon) - f(E_\mathrm{F} + \varepsilon)]\, \rho_\mathrm{s}(E_\mathrm{F} - eV + \varepsilon)\rho_\mathrm{t}(E_\mathrm{F} + \varepsilon)|M_{\mu\nu}|^2,$$

where $f(x)$ is the Fermi function and E_F is the Fermi energy, ρ_s and ρ_t are the density of states of the sample and the tip, respectively, and e is the electron charge. ε is the integration variable [15].

For low voltages Eq. (2.1.13) simplifies to

(2.1.14)
$$I = \frac{4\pi e}{\hbar} \int_{0}^{eV} \mathrm{d}\varepsilon \cdot \rho_\mathrm{s}(E_\mathrm{F} - eV + \varepsilon)\rho_\mathrm{t}(E_\mathrm{F} + \varepsilon)|M_{\mu\nu}|^2.$$

In case of a flat density of states (DOS) of the tip, which means that ρ_t is constant in the studied energy range, the energy dependent part of the tunneling current is determined by the sample alone:

(2.1.15)
$$I \propto V\rho_\mathrm{s}(E_\mathrm{F} - eV).$$

This leads to the fact, that the tunneling current is described by the local density of (electronic) states (LDOS) of the sample at the Fermi energy.

2.2 Scanning Tunneling Spectroscopy

Scanning Tunneling Spectroscopy (STS) is the measurement of the LDOS of surfaces using an STM [23]. Thereby the tip is moved to a point of interest on the sample. When that point is reached, both x- and y-values of the scanning position are held constant. By interrupting the feedback loop the distance between sample and tip (z-axis) is kept constant.

To measure the characteristics of the surface at a specific point, two main operation modes may be applied. In the so called current-distance mode (I-z), the current is measured as a function of distance between sample and tip. Throughout this process the bias voltage is kept constant.

The second possibility is the current-bias mode (I-V), where the tunneling current I is measured as a function of the tunneling voltage V. In this mode the distance of

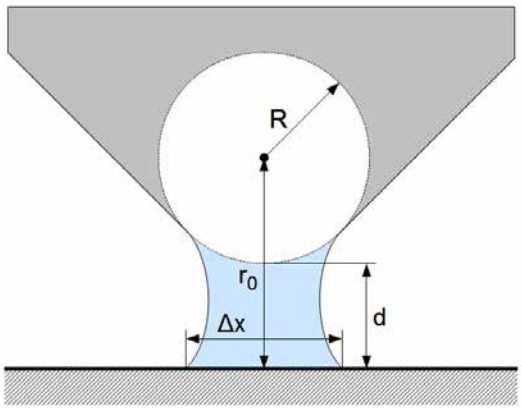

Fig. 2.2.1: Geometry assumed by that Tersoff and Hamann to solve the tunneling current. Δx indicates the spatial resolution of the tip. It is easily seen, that the resolution is better if the tip radius is small (ideally the radius of one atom).

sample and tip is not varied. The variation of the bias current is accomplished by putting an additional voltage ramp to the tunneling junction. The tunneling current as a function of the bias provides the information on the LDOS (see Section 2.2.2).

Since the tunneling current in an STM mainly flows in a region with a diameter of one atom (tip), STS allows a very localized surface analysis.

STS experiments attempt to probe the sample DOS, but Eq. (2.1.13) shows that the tip DOS must be known in order to make the measurement meaningful. The measurement of the DOS can also be realized by superimposing a small, high frequency sinusoidal modulation voltage to the D.C. bias. The A.C. component of the tunneling current is recorded using a lock-in amplifier, and the in-phase component with the tip-sample bias modulation gives $\mathrm{d}I/\mathrm{d}V$ directly.

2.2.1 Tersoff-Hamann Model

In the Tersoff-Hamann model the geometry of the tip is presumed as a local spherical potential well with radius R with the center of curvature at $\boldsymbol{r}_0 = (0, 0, z_0)$ as shown in Fig. 2.2.1 [24, 25]. The surface of the sample is the $z = 0$ plane. In the vacuum region both wave functions satisfy the equation

$$\nabla^2\psi(\boldsymbol{r}) = \kappa^2\psi(\boldsymbol{r}), \tag{2.2.1}$$

where $\kappa = \sqrt{2m\phi}/\hbar$ with ϕ the so-called work function.

This equation can be solved by a two-dimensional Fourier expansion:

$$\psi(\boldsymbol{r}) = \int \mathrm{d}^2\boldsymbol{q} \cdot f(\boldsymbol{q}, z)\, \mathrm{e}^{\mathrm{i}\,\boldsymbol{q}\cdot\boldsymbol{x}}, \tag{2.2.2}$$

where $\boldsymbol{q} = (k_x, k_y)$ and $\boldsymbol{x} = (x, y)$. Solving Eq. (2.2.1) for $\psi(\boldsymbol{r})$, gives

$$\begin{aligned} \int \mathrm{d}^2\boldsymbol{q} \cdot \left[-\boldsymbol{q}^2 f(\boldsymbol{q}, z) + \frac{\mathrm{d}^2}{\mathrm{d}z^2} f(\boldsymbol{q}, z) \right] \mathrm{e}^{\mathrm{i}\,\boldsymbol{q}\cdot\boldsymbol{x}} &= \kappa^2 \int \mathrm{d}^2\boldsymbol{q} \cdot f(\boldsymbol{q}, z)\, \mathrm{e}^{\mathrm{i}\,\boldsymbol{q}\cdot\boldsymbol{x}} \\ \frac{\mathrm{d}^2}{\mathrm{d}z^2} f(\boldsymbol{q}, z) &= \left(\boldsymbol{q}^2 + \kappa^2\right) f(\boldsymbol{q}, z) \end{aligned} \tag{2.2.3}$$

The solution for $f(\boldsymbol{q}, z)$ is a slightly modified form of the original solution of Eq. (2.2.1), namely

$$f(\boldsymbol{q}, z) = a(\boldsymbol{q})\, \mathrm{e}^{-\sqrt{\boldsymbol{q}^2 + \kappa^2}}, \tag{2.2.4}$$

where $a(\boldsymbol{q})$ are the Fourier components of the sample surface wave function at $z = 0$, which contain the information on the electronic structure of the surface.

Inserting the solution in Eq. (2.2.2) gives

$$\psi(\boldsymbol{r}) = \int \mathrm{d}^2\boldsymbol{q} \cdot a(\boldsymbol{q})\, \mathrm{e}^{-\sqrt{\boldsymbol{q}^2 + \kappa^2}}\, \mathrm{e}^{\mathrm{i}\,\boldsymbol{q}\cdot\boldsymbol{x}}. \tag{2.2.5}$$

The STM tip wave function is approximated by an s-wave that is spherically symmetric with respect to the center of the curvature. Thus spherical coordinates are introduced in Eq. (2.1.2). The Laplace operator in spherical coordinates is given by

$$\Delta = \nabla^2 = \frac{1}{r^2 \sin\theta} \left[\frac{\partial}{\partial r} \left(r^2 \sin\theta \frac{\partial}{\partial r} \right) + \frac{\partial}{\partial \theta} \left(\sin\theta \frac{\partial}{\partial \theta} \right) + \frac{\partial}{\partial \varphi} \left(\frac{1}{\sin\theta} \frac{\partial}{\partial \varphi} \right) \right], \tag{2.2.6}$$

which is reduced to

$$\Delta f(r) = \frac{1}{r^2} \frac{\partial}{\partial r} \left(r^2 \frac{\partial}{\partial r} f(r) \right) = \frac{\partial^2}{\partial r^2} f(r) + \frac{2}{r} \frac{\partial}{\partial r} f(r) = \frac{1}{r} \frac{\partial^2}{\partial r^2} \left(r f(r) \right), \tag{2.2.7}$$

if spherical symmetry is assumed, with $r^2 = x^2 + y^2 + (z - z_0)^2$. With this assumption the tip wavefunction can be written as

$$\frac{1}{r} \frac{\partial^2}{\partial r^2} \left(r\chi(r) \right) = \kappa^2 \chi(r). \tag{2.2.8}$$

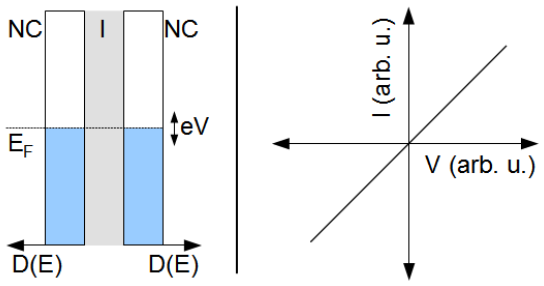

Fig. 2.2.2: Normal metal/insulator/normal metal junctions (left) and the corresponding current.

Up to a constant, the solution is

$$\chi(r) = \frac{1}{r}\,\mathrm{e}^{-\kappa r}, \tag{2.2.9}$$

which is again Fourier transformed for the region $z < z_0$:

$$\chi(r) = \frac{1}{2\pi}\int \mathrm{d}^2\boldsymbol{p}\cdot\frac{1}{\sqrt{\kappa^2+\boldsymbol{p}^2}}\,\mathrm{e}^{\sqrt{\kappa^2+\boldsymbol{p}^2}(z-z_0)}\,\mathrm{e}^{\mathrm{i}\,\boldsymbol{p}\cdot\boldsymbol{x}}, \tag{2.2.10}$$

and $\boldsymbol{p}$ is like $\boldsymbol{q}$ a two dimensional variable. With the functions $\psi(\boldsymbol{r})$ and $\chi(r)$ the Bardeen tunneling matrix element can be evaluated (Eq. (2.1.12)). As a result Tersoff and Hamann found, that the tunneling matrix element is the value of the sample wavefunction at $x = y = 0, z = z_0$ (center of curvature of the tip)

$$M_{\mu\nu} \propto \psi(\boldsymbol{r}_0) \tag{2.2.11}$$

The consequence of this solution is that all wave functions except the tip wave function can be neglected.

2.2.2 Scanning Tunneling Spectroscopy of Superconductors

The superconducting gap Δ can be observed by the $\mathrm{d}I/\mathrm{d}V$ spectra obtained by numerical differentiation of $I(V)$ or by a lock-in amplifier technique. The lock-in technique superimposes a small ac-voltage modulation $V_{\mathrm{ac}}\cos\omega t$ to the sample bias V, and the corresponding modulation in the tunneling current is measured. By

expanding the tunneling current into a Taylor series

$$I = I(V) + \left(\frac{\mathrm{d}I}{\mathrm{d}V}\right) V_{\mathrm{ac}} \cos \omega t + \mathcal{O}(V_{\mathrm{ac}}^2) \tag{2.2.12}$$

one finds that the component at frequency ω is proportional to $\mathrm{d}I/\mathrm{d}V$ if $V_{\mathrm{ac}} \ll V$ and $I(V)$ is sufficiently smooth. The $\mathrm{d}I/\mathrm{d}V$ spectrum represents the LDOS of the excited, unpaired electrons. For voltages $|V| < \Delta$ the Cooper pairs are not broken and thus the LDOS in this energy range is zero (for $T = \boldsymbol{B} = 0$). The advantage offered by the lock-in technique is that the sampling frequency ω can be selected outside the typical frequency domains of mechanical vibrations or electronic noise, thus considerably enhancing the measurement sensitivity [23].

Originally, the superconducting gap was studied in superconductor/insulator/normal metal junctions [26]. The basic theory of such junctions is approximately the same as described in Section 2.1.4. In a superconductor, the density of states changes rapidly in a narrow energy range centered at the Fermi level, so that the voltage-current characteristic becomes nonlinear, as shown in Fig. 2.2.3. The slopes of those curves are displayed on the right-hand-side of Fig. 2.2.3(b). If we assume that tunneling is proportional to the DOS, these curves express the DOS in a superconductor relative to the DOS at its normal conducting state, as a function of energy (measured from the Fermi energy). It is clear that the density of states at the Fermi level is drastically changed when a metal becomes a superconductor, the change being symmetric with respect to the Fermi level. The change in the DOS resembles the BCS theory for quasi-particle excitations.

A more accurate measurement of the energy gap is possible when electrons tunnel between two superconductors [27]. In Fig. 2.2.4 no voltage is applied (leftmost image). When a voltage is applied at $T = 0\,\mathrm{K}$, the tunneling current is equivalent to the tunneling current discussed previously for a superconductor/insulator/normal metal junction (compare Fig. 2.2.3(b) curve (c) and Fig. 2.2.4(c) curve (c)). The only difference in the superconductor/insulator/superconductor junction is that the current increases when $|eV|$ has reached a value greater than $\Delta_1 + \Delta_2$ instead of only Δ.

The case of thermally excited electrons and holes ($T > 0$) is shown in Fig. 2.2.4(b). For the smaller gap thermal excitations are more probable, while for the larger gap there will be relatively few thermally excited electrons (Fig. 2.2.4(b) left image). When a voltage is applied, a current will flow and increase steadily with voltage, because more and more of the thermally excited electrons in the left-hand

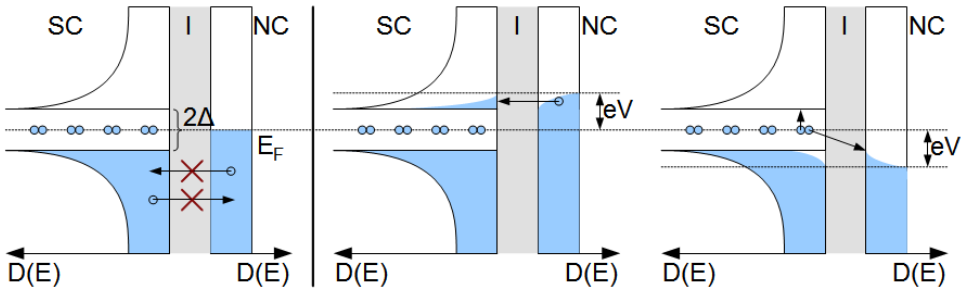

(a) DOS of a superconductor (left) and normal conductor (right). If the energy $|eV|$ exceeds the value of the gap Δ a current flows. Cooper pairs are marked by two attached circles.

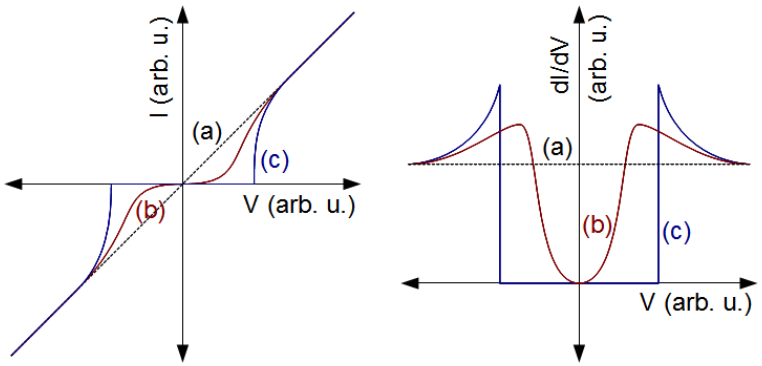

(b) Measured currents $I(V)$ (left image) and their corresponding slope $\mathrm{d}I/\mathrm{d}V$.
(a) normal conductor; (b) superconductor at $T > 0\,\mathrm{K}$; (c) superconductor at $T = 0\,\mathrm{K}$.

Fig. 2.2.3: Schematic view of a superconductor/insulator/normal metal junction. (Combination of semiconductor and superconductor model.)

superconductor can tunnel into unoccupied states above Δ_2 of the right-hand superconductor (compare with Fig. 2.2.4(c) curve (b) the region where $|eV| < |\Delta_2 - \Delta_1|$).

When the applied voltage corresponds to the difference of the two energy gaps, $|\Delta_2 - \Delta_1|$, it is energetically possible for all the thermally excited electrons to tunnel through the insulator and a local maximum in the tunneling current is reached.

When the voltage is further increased, only the same number of electrons can tunnel, and since they now face a less favorable (lower) DOS, the current will decrease (region $|\Delta_2 - \Delta_1| < |eV| < |\Delta_1 + \Delta_2|$). Finally, when a voltage greater than

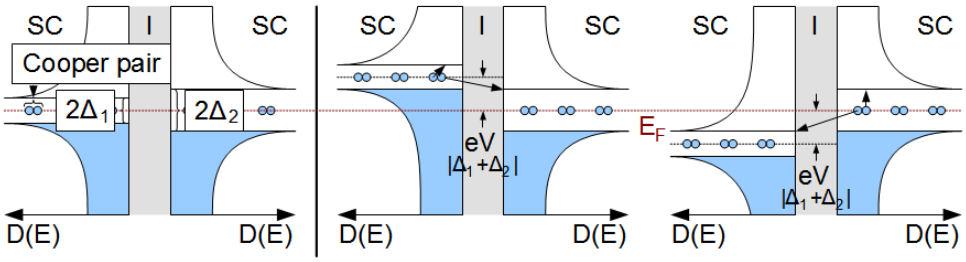

(a) DOS of two different superconductors (i. e. two different gap sizes). Cooper pairs are marked through two attached circles.

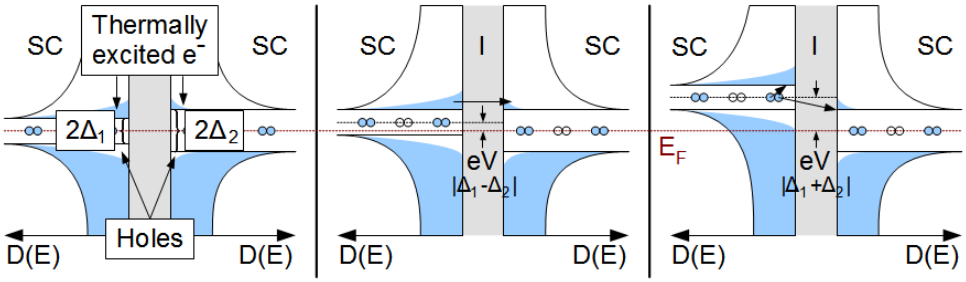

(b) Same as Fig. 2.2.4(a) only at $T > 0\,\mathrm{K}$.

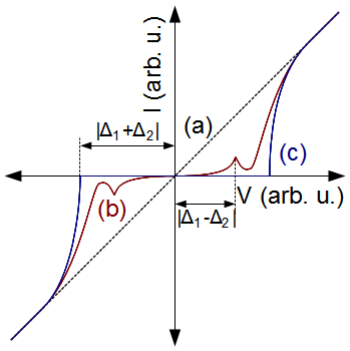

(c) Measured currents $I(V)$.
(a) normal conductor;
(b) superconductor at $T > 0\,\mathrm{K}$;
(c) superconductor at $T = 0\,\mathrm{K}$.

Fig. 2.2.4: Schematic view of a superconductor/insulator/superconductor junction. The images show a combination of the semiconductor model for energy gaps and a superconducting model with Cooper pairs located at the Fermi energy.

the sum of the two energy gaps is applied, the current will increase rapidly because electrons below the gap can begin to tunnel.

To image the Abrikosov flux lattice of type II superconductors one part of the junction is either in the normal conducting state or in the superconducting state. The insulator is the vacuum between sample and tip. The tip can be a normal conducting material or a superconductor. For example, if the tip is normal conducting and located at a normal conducting vortex core then Fig. 2.2.2 describes the system. If the sample is superconducting at the position of the tip Fig. 2.2.3 describes the system.

3 Sample and Experiment

3.1 Sample

The sample used for the investigations of the vortex lattice was niobium diselenide ($NbSe_2$). $NbSe_2$ has a surface that is easy to prepare by simply putting a glue strip on the sample and then removing it. Thereby a small part of the sample is removed and the generated surface is very clean and smooth.

$NbSe_2$ belongs to the family of the AB_2 dichalcogenides, which consist of a stacked triple layer structure as shown in Fig. 3.1.1. These crystals have the property, that while inside each layer strong ionic and covalent bonding predominates, the bonding of neighboring layers is dominated by relatively weak van der Waals forces. Therefore, the layers perpendicular to each other are less well bound. Each layer consists of a highly correlated system of Se-Nb-Se triple bonds and is therefore very well ordered. $NbSe_2$ has a hexagonal lattice with the niobium atoms at the center of trigonal selenium prisms. The unit cell lattice parameters are approximately $a = 0.34\,\mathrm{nm}$ and $c = 1.25\,\mathrm{nm}$ [28]. The niobium ions of different layers are in line with each other along the c-axis.

Large high quality and almost defect free single crystals of $NbSe_2$ can be grown, which have reversible magnetic properties over most of the phase diagram. Defects can be introduced by doping or neutron irradiation usually resulting in the emergence of a second $\boldsymbol{j}_\mathrm{c}$ peak. Neutron irradiation is a very controlled way to modify the defect density, since the defect density is proportional to the irradiation time.

In recent years $NbSe_2$ has become the standard superconducting sample for STM and STS mostly due to the attributes that have already been discussed. Additionally $NbSe_2$ is an inert material, i. e. it hardly reacts with oxygen. At low temperatures $NbSe_2$ can be used to calibrate the STM. The atomic resolution of the layer structure can be applied to calibrate the piezo-scanner for small resolutions and the vortex lattice gives the possibility to calibrate for larger distances [29].

The phase transition from the normal conducting to the superconducting phase occurs at a temperature of about 7 K in $NbSe_2$. The upper critical field is about 4 T

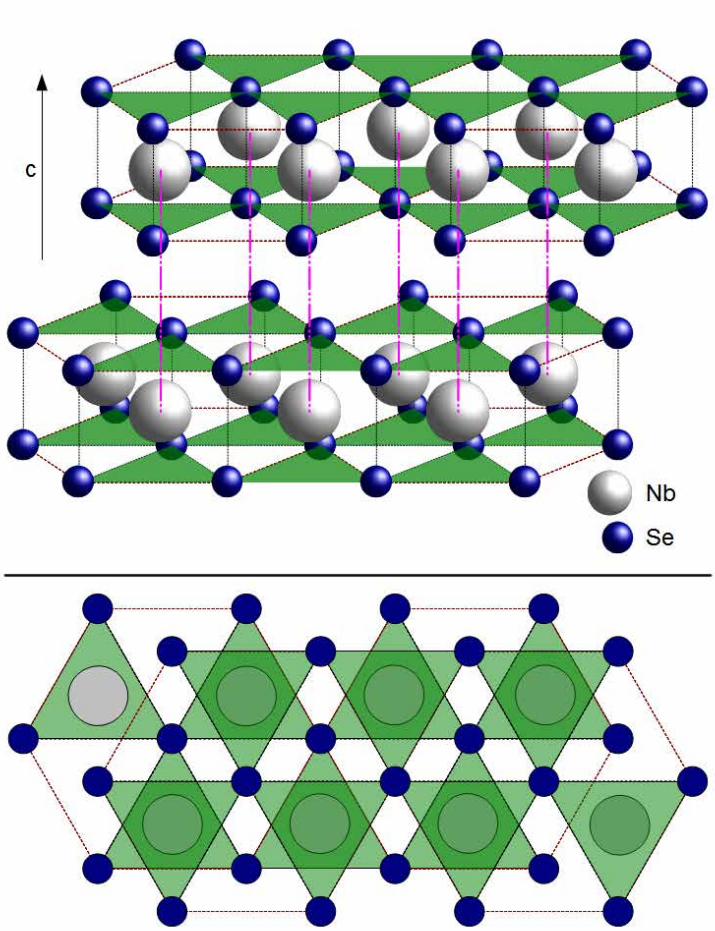

Fig. 3.1.1: Image of the structure of $NbSe_2$ in three dimensions (upper image) and in the a-b plane (lower image). The c-axis is indicated by an arrow.

perpendicular (B_{c2}^{c}) and 12 T parallel (B_{c2}^{ab}) to the Nb plane. Furthermore, $NbSe_2$ shows evidence for a two-band superconducting state [30].

3.1.1 Irradiated Sample

One sample was irradiated in the TRIGA Mark II research reactor of the Atominstitut in Vienna. The thermal neutron flux density of the reactor is $6.1 \cdot 10^{16}\,\mathrm{m^{-2}s^{-1}}$ and the fast neutron flux density is $7.6 \cdot 10^{16}\,\mathrm{m^{-2}s^{-1}}$. The irradiated sample was exposed to the neutron radiation for 220 min.

Fig. 3.1.2(a) shows the critical current density (j_c) of the irradiated sample at 4.22 K, measured in a SQUID and evaluated with an algorithm written by Martin

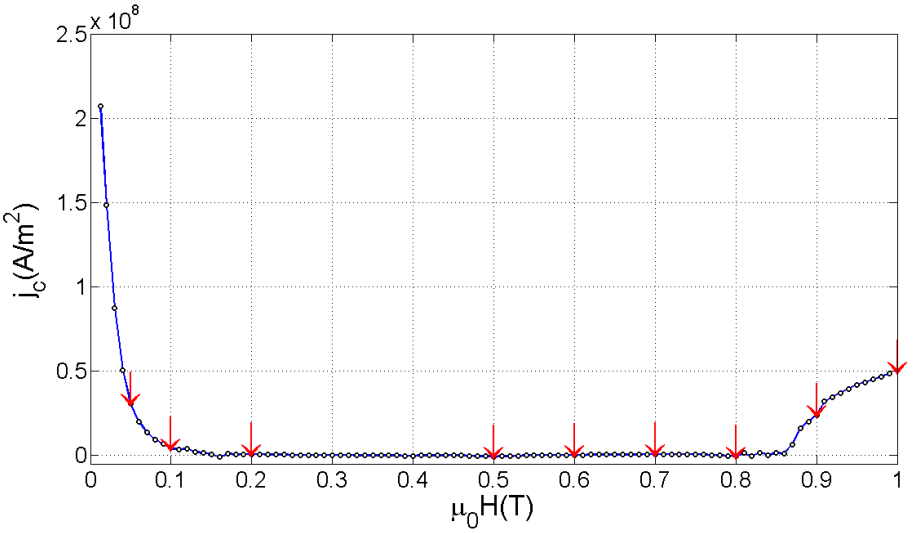

(a) Critical current density at 4.22 K. (Evaluated with an algorithm written by Martin Zehetmayer.) Arrows indicate the fields, at which STM measurements were performed.

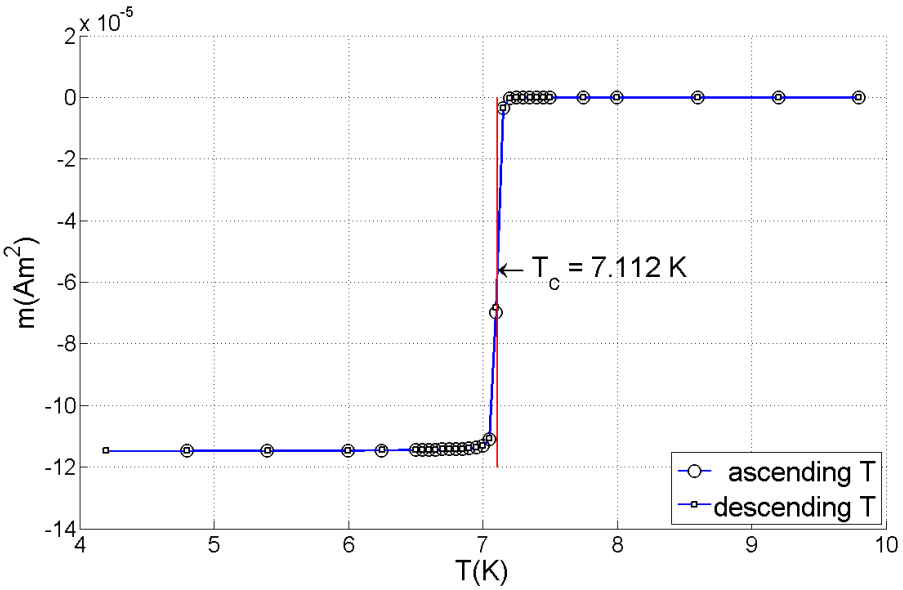

(b) Critical temperature. The value of T_c is approximately 7.1 K.

Fig. 3.1.2: Properties of the irradiated $NbSe_2$ sample, measured in a 1 T SQUID.

Zehetmayer using Eq. (1.5.2) (see [31] for more details on the measuring procedure and evaluation). At high fields the second peak effect is observed which is not present in the pristine sample. Between approximately 0.15 and 0.86 T, j_c is nearly zero, i. e. the magnetization is reversible in this region. The second peak effect first occurs at about 0.86 T. Fig. 3.1.2(b) shows the measurement of the critical temperature (T_c). The transition region was found from about 7.05 to 7.15 K, which is relatively small and indicated a high sample quality. The value of T_c is approximately 7.11 K measured at half of the Meissner value. These are almost the same results as found in the pristine sample.

3.2 Assembling the Sample

3.2.1 Arrangements at Room Temperature

Before starting a measurement a proper sample has to be found. It is most desirable to have very flat and parallel surfaces on both the glued side and the scanning side. A flat surface of the surface in contact with the sample holder is necessary for a stable fixation of the sample. Conductive silver was used as a glue, which has conducting properties, that are essential, because the tunneling current flows through the sample to the holder. Unfortunately, conductive silver does not glue strongly, but the flat surface helps to achieve more stability, which is important for the next step, the cleaving.

After the sample has been fixed on the sample plate for one or two hours, a glue-tape is placed on the upper surface of the sample. A cotton bud is used to rub the glue-tape with a light pressure on the $NbSe_2$ surface. Afterwards the tape is carefully removed. In an ideal case a thin layer of the sample is separated from the sample and the remaining surface is very clean and flat. If this is not the case, the cleaving process has to be repeated.

The advantage of a flat surface is simply the fact, that the measurement can only achieve high resolution if the surface consists of just one atomic plane instead of steps of the size of many atoms, since steps make the measurement worse (see Section 2.1). Furthermore the resulting data is better, if the region where the scan is carried out is not tilted. If the slope of the surface is too steep, it is more probable that the actual measuring atom (the tip) changes during the scan.

The next step is to cut a tip from a Pt-Ir alloy wire. The wire, the tweezers and the side-cutting pliers are cleaned before the preparation. The wire is held with the tweezers while cutting an appropriate tip. During cutting stress is applied by

the side-cutting pliers, so the wire is not cut through, but rather torn apart. This technique improves the probability of having only a single atom working as the tip.

When the sample and tip are arranged satisfactorily, the tunneling current should be tested. Thus the tip is approached "manually" to the sample (still at room temperature). When the tip is near the surface the approach is continued with a computer program (a more detailed description on the program based approach can be found in Section 3.2.2).

When the tunneling current has the desired quality, the sample rod is put into a steel tube. This tube is then evacuated to a pressure of about 10^{-5} to 10^{-4} mbar. Following the evacuation He gas is filled into the tube until a pressure of about 10 to 20 mbar is reached. He should prevent foreign atoms to condense on the sample surface and enable thermal conductivity. Without a thermal contact the heat from the heater cannot be transferred from the sample holder and the quality of the sample may suffer or in the worst case the sample may be burned. Additionally, the heater itself can be damaged.

Finally the steel cylinder is put into the cryostat. While the system is cooling down the heater is turned on. This is an additional precaution to ensure that no foreign atoms condense on the sample surface, but rather on the cylinder face. After the cooling, some days are necessary for the STM to operate correctly, i. e. to stabilize the temperature and get rid of most vibrations.

3.2.2 Low Temperature Preparations

At the end of the cooling process the approach of the tip can proceed. This should not be done manually, because there is a great risk of crashing into the sample surface by accident. Instead a computer program* carries out this step.

The software supplies a sequence for approaching the sample. Before starting the process some parameters have to be specified:

PI-Controller: The proportional part (P) has no real effect on the approaching process, so it can be set to the value needed for the scan (normally the P-value is in the range of 10^{-3} (1 m)). In contrast to this the integral part (I) is the main parameter for the approach. It determines the speed with which the scanner runs through its scanning range, i. e. travels from zero to its maximum. The typical value of I lies between 1 and 5 Hz.

*The program is a commercial software called *Daisy*.

Steps per Approach: This value specifies the number of steps the z-positioner moves towards the sample surface when a complete run of the z-scan-range of the scanner brought no contact with the sample. The overall distance of all steps should not exceed the total scan-range of the scanner. Characteristically, one step of the positioner is about 350 nm, while the scan-range of the scanner is 1200 nm. To be on the safe side the value of *Steps per Approach* is usually set to two or three.

Setpoint: In the approach process the *setpoint* indicates the value of the tunneling current that is not allowed to be exceeded. If the tunneling current is larger than the *setpoint* the process stops. This value has to be larger than the noise or the approach will stop although the sample surface was not reached. A typical amplitude of the noise is about 0.2 nA. On the other hand, the current has to be low enough so that the tip does not crash into the sample accidentally, because of thermal, mechanical or electric fluctuations. Typical values are 0.5 to 1 nA.

Voltage: The voltage defines the bias voltage as described in Section 2.2.2 and is typically set to some mV.

When the above parameters are set, the automatic approach can start. Thereby the scanner checks if a tunneling current occurs in the scanning range of the scanner. If that is the case the process stops. Otherwise the scanner is retracted and the positioner moves the sample nearer to the tip (distance depends on the value of *Steps per Approach*) then the scanner searches again for a tunneling current. Depending on the tip-sample distance the process can take a few hours.

If the approach is finished a magnetic field can be set to generate the vortex lattice in the type II superconductor. The field can be charged either manually with the power supply or by using the program *MPSusb.exe** executable.

3.3 Setting the parameters for an STM-Scan

Before starting an xy-scan the details of the scan have to be specified. The following parameters set the number of the data points (or rather the size of the image; see Fig. 3.3.1).

*This program was written for the purpose of this Diploma thesis.

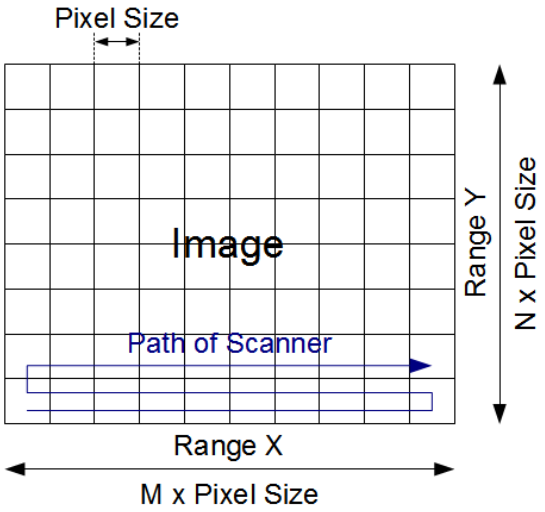

Fig. 3.3.1: Diagram of an STM image with the parameters for specifying the image. The path of the scanner is also indicated.

Pixel Size: Represents the distance between two data points (for x as well as y-direction). For example a *Pixel Size* of 2 nm means, that the scan area is divided into a grid with $M \times N$ squares with 2 nm edge length and every square represents a data point. (M and N are given by *Scan Lines* and *Scan Columns* parameters.)

Scan Lines/Columns: Number of lines (x) and columns (y) of an image.

Range: Defines the scanning area. *Range X* is the space in x-direction in nm and *Range Y* the space in y-direction covered be the scan.

Speed: There are different options available: *Sample Time* is the duration of the measurement for one data point. *Line frequency* is the time for one line. By using the option *Scan Speed* the space (nm) which is covered per time (s) by the scanner is set. Finally *Time per Frame* specifies the time for a whole measurement.

Rotation: To rotate the scan area by a given angle. If the angle is zero, the *Scan Lines* are measured in x-direction.

When the parameters are set, the next step is to compensate the slope of the sample surface. Therefore the *Loop On* condition is enabled and the tip approaches

the surface until the *setpoint* current is reached. By starting a scan in x-direction (*Rotation* is zero) the slope can be compensated through the *Slope Compensation* menu, where the slope has to be indicated (in %). After rotating the scan area by 90° the same is done for the y-direction.

The compensation of the slope does not have to be too precise but when the sample surface shows a prominent slope, the results of the STM measurement may suffer considerably.

3.4 Positioner and Scanner

The nanopositioners and scanner are products of the *attocube* company. The products used are listed below with some specifications for each element.

ANPx101:

travel:	5 mm
scan range:	0.8 µm at 4 K
resolution:	sub nm
size:	24 × 24 × 11 mm
typical minimum step size:	10 nm at 4 K

ANPz101:

travel:	5 mm
scan range:	0.8 µm at 4 K
resolution:	sub nm
size:	24 × 24 × 20 mm
typical minimum step size:	10 nm at 4 K

ANSxyz101:

scan range (xy):	4 × 4 µm at 4 K
scan range (z):	2 µm at 4 K
resolution:	sub nm
size:	24 × 24 × 35 mm

4 Evaluation of Vortex Images

The vortex image of an STM measurement is a data file, where the x and y coordinates of a data point are represented by their location in the data matrix (compare with Fig. 3.3.1). In the topographic image the z-position of the scanner and in case of the spectroscopy image the DOS is saved. Due to the fact that the STM system records data in forward and backward direction there are always two images per scan. These images differ from each other due to a slight hysteresis of the piezo scanner when changing from forward ($+x$) to backward ($-x$) measuring direction.

The data matrix can be converted into an image. This image is the starting point for the analysis of the vortex lattice.

4.1 Preprocessing the Image

The preparation of the data matrix is not a straightforward process. For every image a different way may lead to the best result at the end. In this section different methods which can be applied shall be discussed.

Leveling: If whole rows or columns are significantly out of range compared with the global mean-value of the input-matrix, it is reasonable to add or subtract a constant value for every data point so the mean value of the row is the same as the global mean value.

Trimming: Especially at high fields edges or peaks in the topography of the sample surface lead to strong oscillations in the spectroscopy. The peaks of these oscillations are often many times larger than the actual value of the DOS. To enhance the contrast in the image those values have to be cut off. Firstly, the mean value of all data points is evaluated (global mean value $\bar{z}$). All values that lie outside of the confidence interval $\pm 3 \cdot \sigma$ (with respect to the global mean value of the image) are set to the value $\bar{z} \pm 3 \cdot \sigma$ depending on whether a value is greater (+) or lower (−). At low fields the oscillations are of the

same magnitude as the DOS, so trimming cannot be recommended in this case.

Adjusting: Adjusts the image intensity values to new values between zero and one, such that 1% of the data is saturated at low and high intensities. This means, that 1% of the data points, which have the highest and lowest values are set to one and zero respectifely. This increases the contrast of the output image.

4.1.1 Filtering Images

The platform on which the image processing was carried out is the software MATLAB from "The MathWorks Inc.". The term "filtering" refers to the artificial manipulation of image data to achieve a better visibility of the image. Filtering (or *denoising*) of images is usually done by a conversion between the spatial and frequency domains.

Applying a filter in the spatial domain means to employ a small matrix (called mask or kernel; typically of the size of 3×3 or 5×5 elements) on every input pixel separately and carrying out a convolution with the surrounding pixels. Thereby the matrix is utilized in such a way, that the surrounding pixels are weighted with the values of the matrix elements and then the weighted mean value of the area is determined. The result is an output pixel in the filtered image. The simplest filter would be a matrix with only ones, so that the output pixel is the mean value of all pixels within the area.

Any operation in the spatial domain corresponds to a particular operation in the frequency domain. A filter in the frequency domain normally proceeds as follows: The image is transformed from the spatial domain into the frequency domain (two dimensional Fourier transformation). After the transformation a threshold operation for the frequency is applied to remove the noise. Finally, the transformation is reversed to reconstruct the image.

Fig. 4.1.1(d) shows the results of a two dimensional Fourier transformation for which a so-called *fast Fourier transformation* algorithm was used. The image is reduced into patterns which have a sinusoidal variation along each axis. The low-frequency components are located at the corners of the image and the high-frequencies in the middle. Since a threshold operation for the frequency usually "cuts-off" all frequencies inside or outside a certain frequency (*high-pass* and *low-pass* filter, respectively), a shift of the zero-frequency component to the center of the spectrum allows the definition of a circle at the center of the image with a

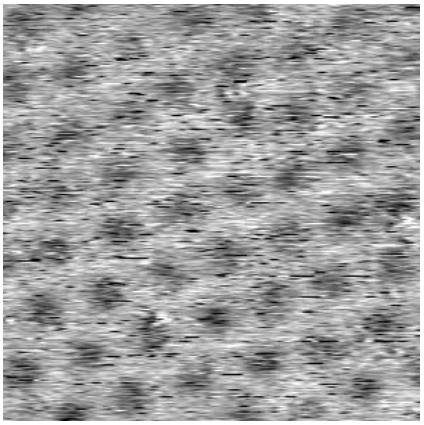

(a) Original Image.

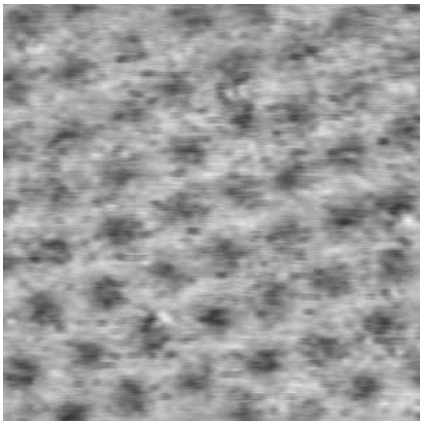

(b) Gauss filtered image.

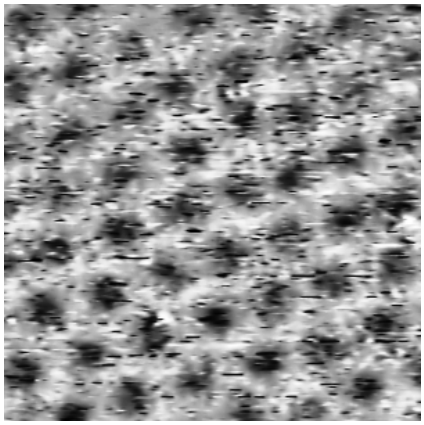

(c) *log-Gabor* filtered image.

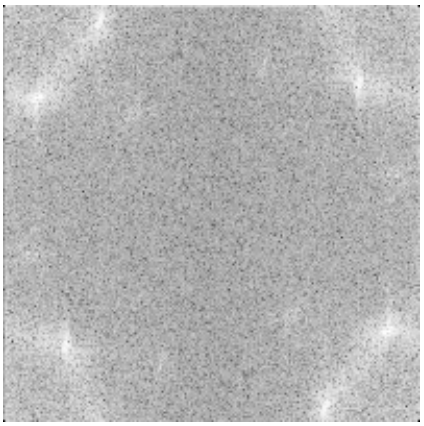

(d) Fourier transformed image (in logarithmic scaling) of Fig. 4.1.1(a).

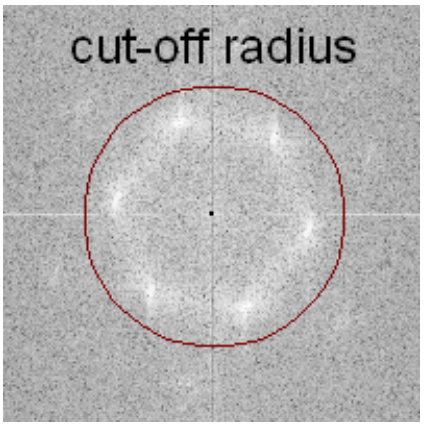

(e) Fig. 4.1.1(d) after shifting low frequencies to the center.

Fig. 4.1.1: STM data on an irradiated sample at 0.8 T.

cut-off-radius (Fig. 4.1.1(e)). Additionally to a *cut-off-radius* a weighted matrix as described above can be applied (e. g. *Butterworth* or *Gauss* filters; see Fig. 4.1.1(b)).

In the Fourier transformed images the brightness corresponds to the amplitudes of the Fourier components. The logarithm scales exhibit more details of the Fourier transformed image. In Fig. 4.1.1(d) and (e) bright maxima at lower frequencies are observed, which indicate that these frequencies occur most often.

In this work a *log-Gabor* filter [32] was used because of the slightly better results and the freedom of varying many different parameters without using different filter algorithms to get satisfying results (Fig. 4.1.1(c)).

4.2 Locating the Position of Vortices

To find the position of vortices in the filtered image, the minima of the image data have to be found. This is done by searching for data points below a certain threshold value. The coordinates of these data points are used to construct a *binary image* (black-and-white image) of the same size as the original image, by setting the points below the threshold to one and those above to zero.

In the next step, "holes" in the vortices of the *binary image* are filled (if they occur), resulting in an image with a black background and white circle-like shapes which indicate the vortex positions. Furthermore the image is eroded (i. e. scaled down) to a certain size (e. g. to half of the original size) to get rid of smaller defect "clusters", that are not vortex positions (Fig. 4.2.1(a)). A cluster is an artifact that usually shows up when the sample surface is uneven (see Fig. 2.1.1). Subsequently the eroded image is returned to its original size.

It is possible, that vortices or the tip (respectively the scanner) suddenly move by a small distance during a measurement. If a vortex "jumps" to a different position, only this vortex would be located at a different position in the image (Fig. 4.2.1(b)) and is therefore easy distinguishable from a "jump" of the tip, where all vortices seem to have moved by a certain distance. Single vortex "jumps" were only observed at low fields, e. g. 0 T.

The final operation is to label every vortex position, i. e. to construct an array for each "shape" (i. e. the vortex), and measure the properties of these shapes. The center of a vortex is determined by the center of the shape.

In images with a good contrast and with small clusters about 95 - 100 % of the vortex positions can be found. If a vortex position is not found but is clearly visible in the image the position can be marked manually. Another error, that

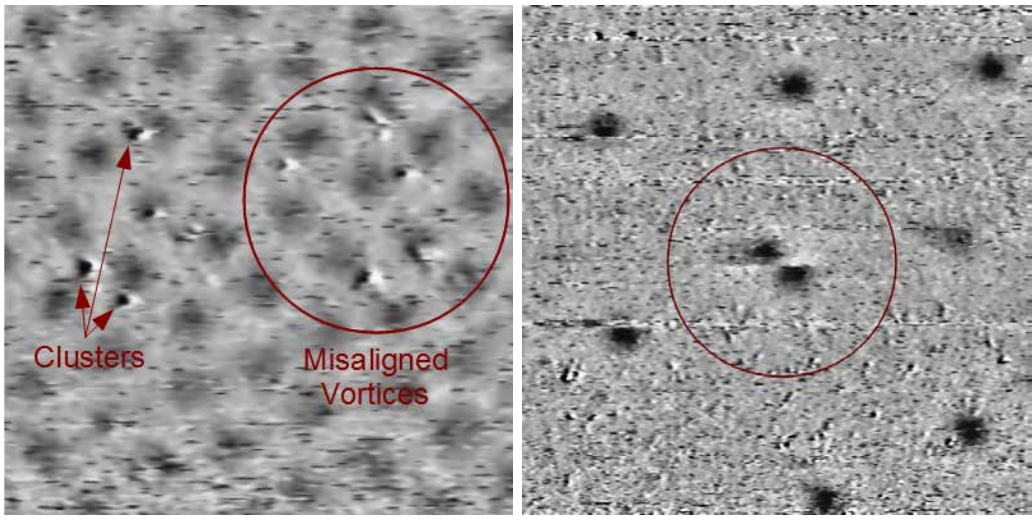

(a) Surface defect clusters in an STM image (0.6 T).

(b) "Jump" of a vortex core (at 0 T in the remanent field state).

Fig. 4.2.1: Different errors that may occur in an STM measurement.

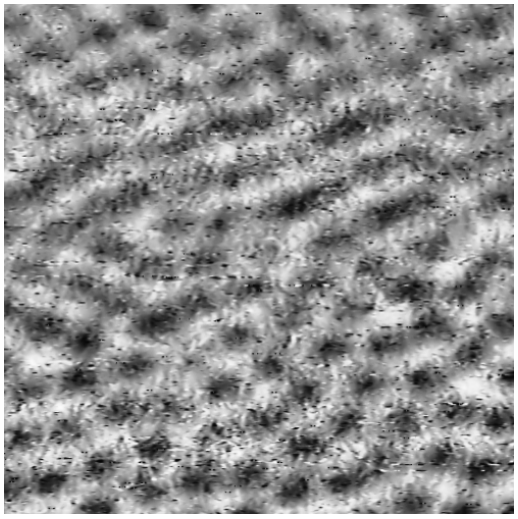

Fig. 4.2.2: Merging of vortices at high fields. (1.0 T irradiated sample)

mainly occurs at high fields, is that two separate vortices appear merged to a single vortex that is stretched in a certain direction, or that a defect cluster is close to the evaluated vortex making it difficult to resolve the correct vortex position.

When all vortices are found and placed correctly various numerical analysis methods can be carried out.

4.3 Dislocations

A real vortex lattice differs from the ideal hexagonal lattice structure. Deviations from of the ideal lattice can be illustrated by counting the nearest neighbors of each vortex. In an ideal hexagonal lattice a vortex would always have six neighbors, however, a real vortex may have more or less neighbors. A vortex with a nearest neighbor number that is different from six defines a defect.

The easiest way to find the nearest neighbors is a Delaunay triangulation (see Fig. 4.3.1) where three points are connected with a triangle if they are nearest neighbors. Note, that in some cases small displacements of a vortex position may cause or annihilate a defect (called "critical defect" from now on). The defects can usually be seen as pairs of vortices with one having five neighbors while the second possesses seven (so-called *twisted bond* configuration). Fig. 4.3.2 shows that small variations in the vortex position can lead to defects.

To see how many such critical cases exist in a measurement a Voronoi diagram can be built. In a Voronoi diagram a critical defect can emerge, where one or more borders of a Voronoi cell are very small.

Fig. 4.3.3 shows the results of the search for nearest neighbors at 0.6 and 0.9 T. The defects on the edges of the image occur due to the limited range of the original measurement and are therefore not included in the evaluation of the images.

4.3.1 Lindemann Criterion

A simple phenomenological rule for the melting of systems is the Lindemann criterion. The Lindemann criterion states that a system melts, when the ratio of the root of the mean square of the displacement $\sqrt{\langle u^2 \rangle}$ and the lattice parameter (a) reaches a certain value c_L (Lindemann's constant):

$$\frac{\sqrt{\langle u^2 \rangle}}{a} \leftrightarrow c_\mathrm{L}. \tag{4.3.1}$$

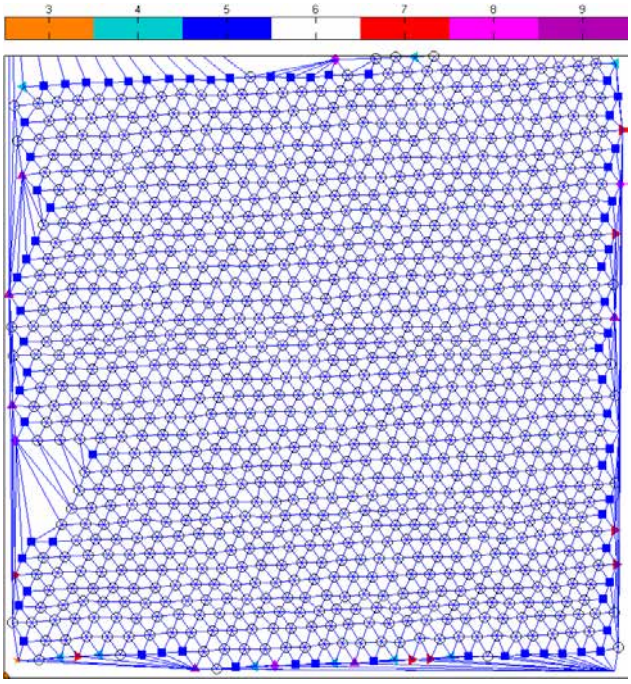

Fig. 4.3.1: Delaunay diagram of the pristine sample at 1.0 T. Vortex positions are given by the crossing points of the lines. ◀ indicates four, ■ five, ∘ six, ▶ seven and ◆ eight nearest neighbors.

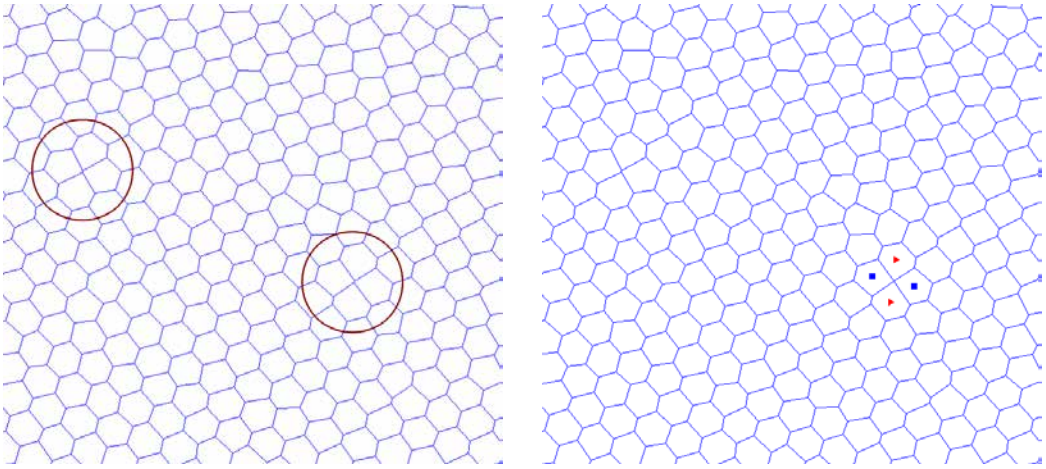

Fig. 4.3.2: Illustration of *twisted bonds* in the irradiated sample:
Left image: Voronoi diagram for an STM image. Only vortices with six neighbors are found. "Critical defects" are marked by a circle.
Right image: The same data as in the left image is displayed, with the difference, that one vortex (the right square in the image) was moved by 4 nm (two pixels in the image) to the right, resulting in two *twisted bonds* configurations.

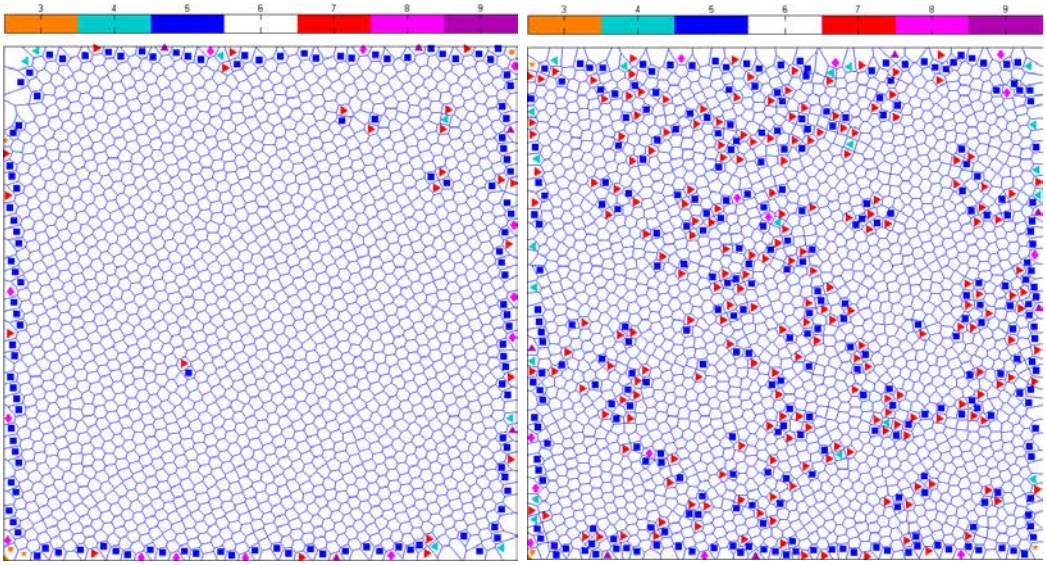

Fig. 4.3.3: Vortex lattice of irradiated $NbSe_2$ (compare also with Fig. 3.1.2(a)). Each vortex sits in the center of a closed area. ◀ indicates four, ■ five, ▶ seven and ◆ eight nearest neighbors:
Left image: Voronoi diagram of an STM image at 0.6 T. Almost no defects occur (except for the edges). The visible defects are "critical defects".
Right image: Voronoi diagram of the same sample at 0.9 T. The field 0.9 T lies in the region of the second peak effect, it is clearly seen that many defects occur.

If the ratio is smaller than c_L the system is assumed to be in the crystalline state. Above c_L the system is melting. The value of c_L depends on the characteristics of the system, like the unit cell structure. A typical value for a metal is 0.12. For the vortex lattice transition a Lindemann number of ≈ 0.2 is suggested [33].

In solids u is the amplitude of the thermal oscillations of a particle in the lattice:

$$u = |\boldsymbol{r} - \boldsymbol{a}|, \tag{4.3.2}$$

where $\boldsymbol{a}$ is the position of the ideal lattice and $\boldsymbol{r}$ is the measured position of the particle. In the vortex lattice, u is the displacement of the vortex center from the ideal lattice position. Due to the fact that the vortex lattice is strongly disordered at high fields, it is very complicated to identify the location and orientation of the ideal lattice in the STM image. Therefore, instead of comparing the vortex core with an ideal lattice position, the distribution of the nearest neighbor distance is used:

$$u_r = |\boldsymbol{r} - \boldsymbol{r}_j| - a_0. \tag{4.3.3}$$

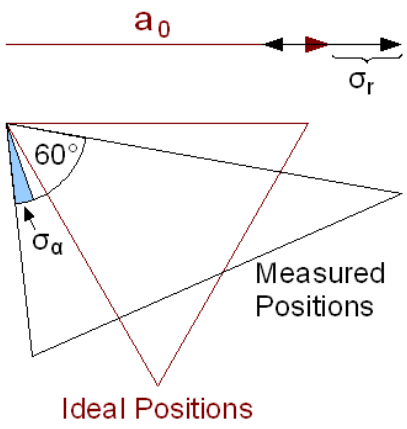

Fig. 4.3.4: Graphical definition of σ_r and σ_α.

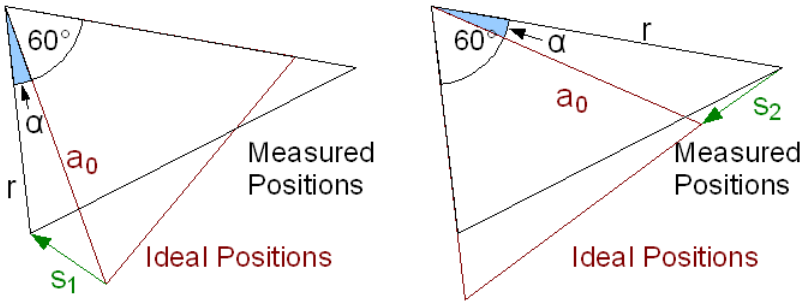

Fig. 4.3.5: Combination of the radial and spatial distribution.

Here $\boldsymbol{r}_j$ defines the location of a nearest neighbor, accordingly $|\boldsymbol{r}-\boldsymbol{r}_j|$ is the distance between the vortex cores (in an ideal lattice a_0). The distances are assumed to be normal distributed and can be fitted with the Gauss function

$$f(r) = \frac{N}{\sqrt{\pi}} \frac{1}{\sqrt{2\sigma^2}} \mathrm{e}^{-\frac{(r-\bar{r})^2}{2\sigma^2}}, \tag{4.3.4}$$

where N is a constant to normalize the function, $\bar{r}$ is the expectation value of r and σ is the standard deviation.

Another distribution that describes the lattice disorder is the angle included between nearest neighbors in the Delaunay diagram. The distribution of the angles (u_α) can also be described with a Gauss function. The Gauss functions of u_r and

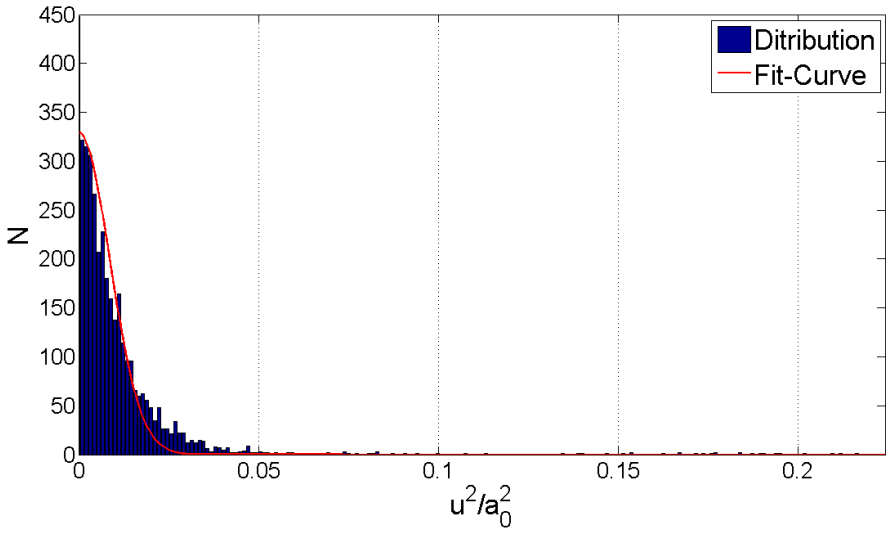

Fig. 4.3.6: Distribution of u^2 for the combination of spatial and radial part of the 0.8 T measurement of the irradiated sample. The distribution was fitted with a Gauss function, where the maximum of the function is located at $\boldsymbol{u}^2 = 0$.

u_α yield standard deviations that help to describe the characteristics of the system (e. g. crystalline). The square standard deviation of the Gauss function is equal to $\langle u^2 \rangle$, thus:

$$\langle u_r^2 \rangle = \sigma_r^2 \quad \text{and} \quad \langle u_\alpha^2 \rangle = \sigma_\alpha^2. \tag{4.3.5}$$

A distribution of u, where the angular and radial parts are combined, is shown in Fig. 4.3.5: The starting point of the evaluation is the result of the Delaunay triangulation, where every vortex $v_{i,3}$ has two nearest neighbors $v_{i,1}$ and $v_{i,2}$. These three vortices define a triangle. For every vortex two s-values (s_1, s_2) are calculated as shown in the figure. The possible values of s are evaluated with the cosine rule:

$$s^2 = a_0^2 + r^2 + 2ra_0 \cos(\alpha). \tag{4.3.6}$$

The angle α is the deviation of the opening angle compared to $\pi/3$. The third value (s_3) is zero because it is assumed that the vortex for which the evaluation is carried out $(v_{i,3})$ is located at an ideal vortex position. Consequently the mean value of

$u^2_{i,3}$ for the vortex $v_{i,3}$ is:

$$u^2_{i,3} = \frac{1}{3}(s_1^2 + s_2^2 + s_3^2) = \frac{1}{3}(s_1^2 + s_2^2). \tag{4.3.7}$$

The same evaluation process is carried out for the vortices $v_{i,1}$ and $v_{i,2}$ yielding $u^2_{i,1}$ and $u^2_{i,2}$, respectively. The mean value of all three vortices is given by:

$$u_i^2 = \frac{1}{3}\sum_{j=1}^{3} u^2_{i,j}. \tag{4.3.8}$$

Fig. 4.3.6 shows the distribution of u^2 for the 0.8 T measurement. The distribution has a maximum at zero. This behavior can be described with a Gauss distribution (fit-curve). The last step is to evaluate the mean value of u_i^2 for the STM measurement:

$$\langle u^2 \rangle = \frac{\sum u_i^2 N_i}{\sum N_i}, \tag{4.3.9}$$

where N_i is the number of how often the value u_i^2 occurs (i. e. N_i is the partition function). With Eq. (4.3.9) a value δ can be evaluated:

$$\frac{\sqrt{\langle u^2 \rangle}}{a_0} = \delta. \tag{4.3.10}$$

which can be compared with c_L to determine the state of the lattice.

4.4 Correlations in the Vortex Lattice

Once the positions of the vortices and the number of the nearest neighbors are found, the correlation functions of the lattice can be evaluated. Correlation functions help to find the behavior of variables that describe the lattice. In a measurement of the vortex lattice we are interested in the kind of order (short or long) of the vortex positions as a function of the magnetic fields and the irradiation time.

One important correlation function is the *translation correlation function* $C_{\boldsymbol{G}}$, a second the so-called *orientation correlation function* C_6, where "6" refers to the hexagonal structure of the ideal vortex lattice. Both correlation functions were first defined by D. Nelson [34] and help to quantify how strongly the lattice is correlated.

The *translation correlation function* is defined through:

$$C_{\boldsymbol{G}}(\boldsymbol{r}) = \frac{1}{n(\boldsymbol{r})} \langle \psi_{\boldsymbol{G}}(\boldsymbol{r}) \psi^*_{\boldsymbol{G}}(0) \rangle \,, \tag{4.4.1}$$

with the translational order parameter $\psi_{\boldsymbol{G}}(\boldsymbol{r}) = \exp(\mathrm{i}\,\boldsymbol{G}\boldsymbol{r})$. $\boldsymbol{r}$ is the distance between two points and $\boldsymbol{G}$ is a reciprocal vector of the ideal lattice, normally the most distinct reciprocal vector in the Fourier space of the vortex positions (Section 4.4.2). $n(\boldsymbol{r})$ is the number of pairs $\psi_{\boldsymbol{G}}(\boldsymbol{r})\psi^*_{\boldsymbol{G}}(0)$ separated by the distance $\boldsymbol{r}$.

For a real vortex lattice $C_{\boldsymbol{G}}$ can be evaluated as follows

$$C_{\boldsymbol{G}}(r) = \frac{1}{n(r)} \sum_{i=1}^{N} \sum_{j=i+1}^{N} \psi_{\boldsymbol{G}}(\boldsymbol{r}_j) \psi^*_{\boldsymbol{G}}(\boldsymbol{r}_i) \delta(r - |\boldsymbol{r}_j - \boldsymbol{r}_i|), \tag{4.4.2}$$

where $\boldsymbol{r}_i$ characterizes the absolute vortex positions in the STM image. N is the number of vortices found in the image and $n(r)$ is the number of vortices separated by the distance r. If the lattice is disordered, i. e. the vortex cores are displaced randomly, $C_{\boldsymbol{G}}$ converges to a constant greater than zero.

In the Delaunay diagram every vortex at the position $\boldsymbol{r}_i$ is connected with its nearest neighbors (indexed with j). Those nearest neighbors can be characterized through their relative distances $\boldsymbol{r}_i - \boldsymbol{r}_j$ and the corresponding angle $\theta_j(\boldsymbol{r}_i)$ in relation to an arbitrary axis (e. g. x-axis). The order parameter (or *bond order parameter*) of this constellation is defined by

$$b(\boldsymbol{r}_i) = \frac{1}{s} \sum_{j=1}^{s} \mathrm{e}^{\mathrm{i}\,6\theta_j(\boldsymbol{r}_i)}, \tag{4.4.3}$$

where s is the number of nearest neighbors of the vortex located at $\boldsymbol{r}_i$. In an ideal hexagonal lattice this number is six. For defects the number is lower or greater. For an ideal hexagonal lattice, with a angle α to the x-axis, the correlation order is given by

$$b(\boldsymbol{r}_i) = \mathrm{e}^{\mathrm{i}\,6\alpha} \frac{1}{s} \sum_{j=1}^{s} \mathrm{e}^{\mathrm{i}\,6 \cdot j \frac{\pi}{3}} = \mathrm{e}^{\mathrm{i}\,6\alpha} = \text{const}\,. \tag{4.4.4}$$

Using b, the *orientation correlation function* for a real lattice can be similarly defined as Eq. (4.4.2):

$$C_6(r) = \frac{1}{n(r)} \sum_{i=1}^{N} \sum_{j=i+1}^{N} b(\boldsymbol{r}_j) b^*(\boldsymbol{r}_i) \delta(r - |\boldsymbol{r}_j - \boldsymbol{r}_i|). \tag{4.4.5}$$

For the ideal lattice $b(\boldsymbol{r}_j) = b(\boldsymbol{r}_i)$ is fulfilled for all i and j and therefor $C_6(r) = \delta(r - |\boldsymbol{r}_j - \boldsymbol{r}_i|)$. The *orientation correlation function* describes the decay of the orientation order with increasing distance r.

Both, *translation* and *orientation correlation function* are important to describe intrinsic properties of the lattice structure. One advantage is that the decay of the functions is not significantly affected by small evaluation errors of the vortex positions. Thus the vortex structure can be compared with macroscopic parameters such as the temperature or pinning strength (not part of this work).

Another correlation function is the so-called *pair correlation function* $g(\boldsymbol{r})$. This function can be interpreted as the probability of finding the center of a vortex at a given distance away from the center of a different vortex position. For the ideal lattice $g(\boldsymbol{r})$ would be a superposition of delta functions (for the two dimensional lattice):

$$g(\boldsymbol{r}) = \sum_{\boldsymbol{a}} \delta(\boldsymbol{r} - \boldsymbol{a}) \quad \text{with} \quad \boldsymbol{a} = \sum_{h,k} h \cdot \boldsymbol{a}_1 + k \cdot \boldsymbol{a}_2 \tag{4.4.6}$$

where $\boldsymbol{a}_1$ and $\boldsymbol{a}_2$ are the base-vectors of the lattice. When a real lattice is considered the delta peaks widen due to statistical errors or displacements. If the system is completely uncorrelated $g(\boldsymbol{r})$ becomes constant. In two dimensions the *pair correlation function* can be described by:

$$g(r) = \frac{1}{N(N-1)} \cdot \frac{F}{\mathrm{d}A} \sum_{i=1}^{N} \sum_{j=1}^{N} \delta(r - |\boldsymbol{r}_j - \boldsymbol{r}_i|) \quad \text{with} \quad j \neq i. \tag{4.4.7}$$

F denotes the size of the image (e. g. $3 \times 3\,\mu\mathrm{m}$) and r is the absolute value of the distance of two points. The circular area, in which a search for other vortex centers is carried out, is

$$\mathrm{d}A = \pi r^2 - \pi(r - \mathrm{d}r)^2, \tag{4.4.8}$$

with $\mathrm{d}r$ the step width of the search. Since the total number of vortices in a typical measurement is relatively small (1000 - 2000) compared to the image size, a visible error is observed for high r values (Fig. 4.4.1(a)). The error occurs because Eq. (4.4.7) does not take the borders of the image into account. In Fig. 4.4.1(b) a scaling of $1/(1 - r/\sqrt{F})$ is applied. The scaling is an approximation which leads to a divergence at $r = \sqrt{F}$. The result is the known feature of $g(r)$ to converge to one at great distances.

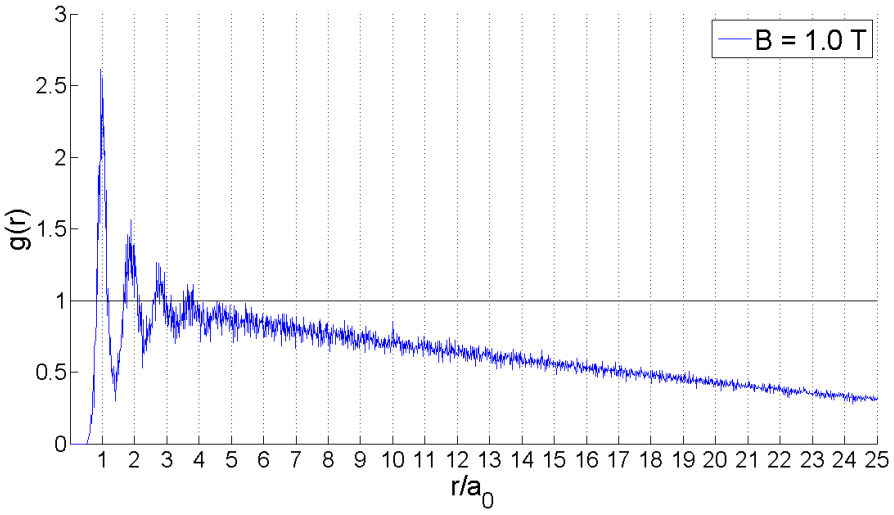

(a) Evaluation of $g(r)$ with Eq. (4.4.7). The reduction for increasing r is caused by the fact that for a vortex near the border of the image, some vortices at a distance r lie outside the image. This means that $\mathrm{d}A(r)$ has to be reduced accordingly.

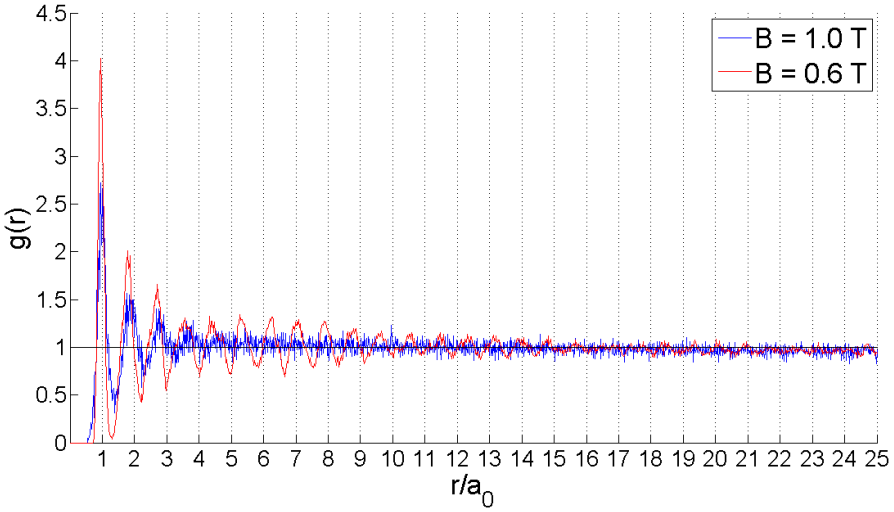

(b) Evaluation of $g(r)$ with scaling for 0.6 T and 1 T. For both fields the same irradiated sample was used.

Fig. 4.4.1: *Pair correlation function* $g(r)$ for the irradiated sample.

4.4.1 Construction of a Two-Dimensional Reciprocal Lattice

The base-vectors of the normal ($\boldsymbol{a}$) and reciprocal lattice ($\boldsymbol{g}$) must satisfy the condition

$$\boldsymbol{a}_i \cdot \boldsymbol{g}_j = 2\pi\delta_{ij} \quad \text{with} \quad i,j = 1,2, \tag{4.4.9}$$

which can also be written as the matrix product

$$A_{i,k} \cdot G_{k,j} = 2\pi\delta_{ij} \tag{4.4.10}$$

where the matrices are defined by

$$A_{i,k} = A^{\mathrm{T}} = \begin{bmatrix} (a_{11}, a_{12}) \\ (a_{21}, a_{22}) \end{bmatrix} = \begin{bmatrix} a_{11} & a_{12} \\ a_{21} & a_{22} \end{bmatrix} \tag{4.4.11}$$

and

$$G_{k,j} = G = \begin{bmatrix} \begin{pmatrix} g_{11} \\ g_{12} \end{pmatrix} \begin{pmatrix} g_{12} \\ g_{22} \end{pmatrix} \end{bmatrix} = \begin{bmatrix} g_{11} & g_{21} \\ g_{12} & g_{22} \end{bmatrix}. \tag{4.4.12}$$

By multiplying the inverse matrix of A, Eq. (4.4.10) can be written as

$$G_{k,j} = 2\pi A^{-1}_{i,k} \cdot \delta_{ij} = 2\pi A^{-1}_{j,k}. \tag{4.4.13}$$

The solution of this linear system of equations for the reciprocal lattice vectors (in two dimensions) is

$$\boldsymbol{g}_1 = \frac{2\pi}{\det(A)} \begin{pmatrix} a_{22} \\ -a_{21} \end{pmatrix} \quad \text{and} \quad \boldsymbol{g}_2 = \frac{2\pi}{\det(A)} \begin{pmatrix} -a_{12} \\ a_{11} \end{pmatrix}. \tag{4.4.14}$$

The reciprocal lattice vectors are evaluated through a scaling ($\det(A)$) and an angle of the lattice vectors. For a hexagonal lattice a possible set of lattice vectors is realized by

$$\boldsymbol{a}'_1 = a_0 \begin{pmatrix} 1 \\ 0 \end{pmatrix} \quad \text{and} \quad \boldsymbol{a}'_2 = a_0 \begin{pmatrix} 1/2 \\ \sqrt{3}/2 \end{pmatrix} \tag{4.4.15}$$

and give the determinant

$$\det(A) = a_0^2 \frac{\sqrt{3}}{2}. \tag{4.4.16}$$

The reciprocal lattice vectors for a two dimensional hexagonal lattice are evaluated to

$$\boldsymbol{g}_1 = \frac{4\pi}{a_0\sqrt{3}} \begin{pmatrix} \sqrt{3}/2 \\ -1/2 \end{pmatrix} \quad \text{and} \quad \boldsymbol{g}_2 = \frac{4\pi}{a_0\sqrt{3}} \begin{pmatrix} 0 \\ 1 \end{pmatrix}. \tag{4.4.17}$$

The measured lattice is usually not aligned with an axis but arranged at a certain angle ϕ. This can be taken into account by a single Euler rotation:

$$\begin{pmatrix} a_{i1} \\ a_{i2} \end{pmatrix} = \begin{bmatrix} \cos(\phi) & -\sin(\phi) \\ \sin(\phi) & \cos(\phi) \end{bmatrix} \begin{pmatrix} a'_{i1} \\ a'_{i2} \end{pmatrix}, \tag{4.4.18}$$

which leads to the reciprocal lattice vectors

$$\boldsymbol{g}_1 = \frac{2\pi}{\det(A)} \begin{pmatrix} a'_{21}\sin(\phi) + a'_{22}\cos(\phi) \\ a'_{22}\sin(\phi) - a'_{21}\cos(\phi) \end{pmatrix} = \frac{4\pi}{a_0\sqrt{3}} \frac{1}{2} \begin{pmatrix} \sin(\phi) + \sqrt{3}\cos(\phi) \\ \sqrt{3}\sin(\phi) - \cos(\phi) \end{pmatrix} \tag{4.4.19}$$

and

$$\boldsymbol{g}_2 = \frac{2\pi}{\det(A)} \begin{pmatrix} a'_{12}\sin(\phi) - a'_{11}\cos(\phi) \\ a'_{11}\sin(\phi) + a'_{12}\cos(\phi) \end{pmatrix} = \frac{4\pi}{a_0\sqrt{3}} \begin{pmatrix} -\cos(\phi) \\ \sin(\phi) \end{pmatrix}. \tag{4.4.20}$$

4.4.2 Fourier Transformation of the Vortex Lattice

With a Fourier transformation such as shown in Fig. 4.1.1(e) the reciprocal lattice vectors can be determined. The reciprocal lattice vectors are needed for the calculation presented in Section 4.4. Since only one vector is necessary for the equations the "brightest" spot in Fig. 4.1.1(e) is used (i. e. the area where many reciprocal lattice vectors point at the same point of the image).

It is also possible to find the nearest neighbor distance a_0 by evaluating the absolute value of Eq. (4.4.19) or (4.4.20) with the found reciprocal lattice vectors. Additionally, the angle ϕ can be evaluated with the same equations.

Another use of Fourier transformed images is to illustrate the order of the lattice. Fig. 4.4.2 shows the Fourier transformation of the vortex cores for the ordered and

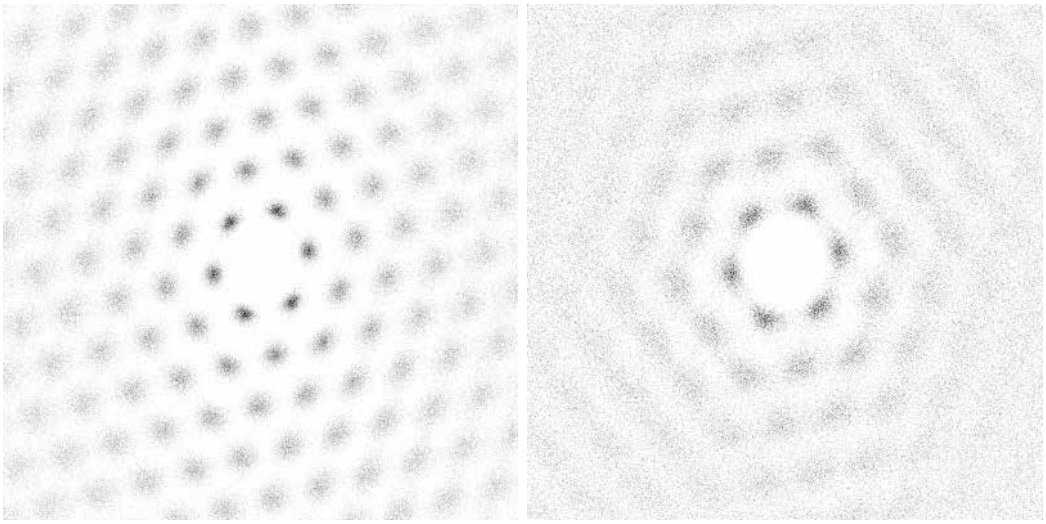

Fig. 4.4.2: Two dimensional Fourier transformation of the vortex core positions for 0.7 T (left image; ordered lattice) and 0.9 T (right image; disordered lattice) of the irradiated sample.

the disordered case. The difference of these cases is easily seen: At 0.7 T the lattice is more ordered than at 0.9 T, where the dark spots are smeared out and the image is only a homogeneous gray far away from the center.

5 Results and Discussion

5.1 Distortions and Vortex Locations

The state of order or disorder in a vortex lattice can be seen in many characteristic parameters. In the context of this Diploma thesis, some mathematical algorithms were written to help interpreting the vortex images. In the following chapter a summary of the results is given.

In Tab. 5.1.1 some parameters are given that indicate the number of defects in the lattice.

Tab. 5.1.1: Characteristics of STM images for various applied fields $\mu_0 H$ for the irradiated sample. N gives the number of vortices found in the image. a_0^{M} and a_0^{T} are the expectation values of the nearest neighbor distance, where the superscript M indicates the value found in the measurement while T indicates the value of the theory (Eq. (1.4.1)). Δa_0 is the difference between measurement and theory. (The values of a_0 and the pixel size are given in nm.) ϕ denotes to the smallest angle between the x-axis and the lattice bond direction in degrees (values from 0° to 60° are possible).

$\mu_0 H$ (T)	N	$a_0^{\mathrm{M}}(nm)$	$a_0^{\mathrm{T}}(nm)$	$\Delta a_0(nm)$	Pixel size (nm)	$\phi(^\circ)$
0.05	205	211.8	218.6	-6.8	2.1	18.5°
0.1	261	153.5	154.6	-0.9	2.0	22.6°
0.2	737	107.3	109.3	-2.0	2.1	18.8°
0.5	1219	70.7	69.1	1.6	2.0	19.6°
0.6	1958	62.8	63.1	-0.3	2.0	17.9°
0.7	2397	58.7	58.4	0.3	1.9	19.9°
0.8	1913	56.4	54.7	1.7	1.6	20.5°
0.9	2163	52.2	51.5	0.7	1.5	20.5°
1.0	1669	50.9	48.9	2.0	1.3	21.2°

The size of one pixel is given to help estimating uncertainties of the results. The pixel size can be roughly seen as the maximal possible error of a vortex position. If the difference $|\Delta a_0|$, found in the STM measurement, is smaller or about the same value as the pixel size, it is not possible to say if the value of a_0^{M} is the "real" nearest neighbor distance or just an error due to the pixel size. For example, at

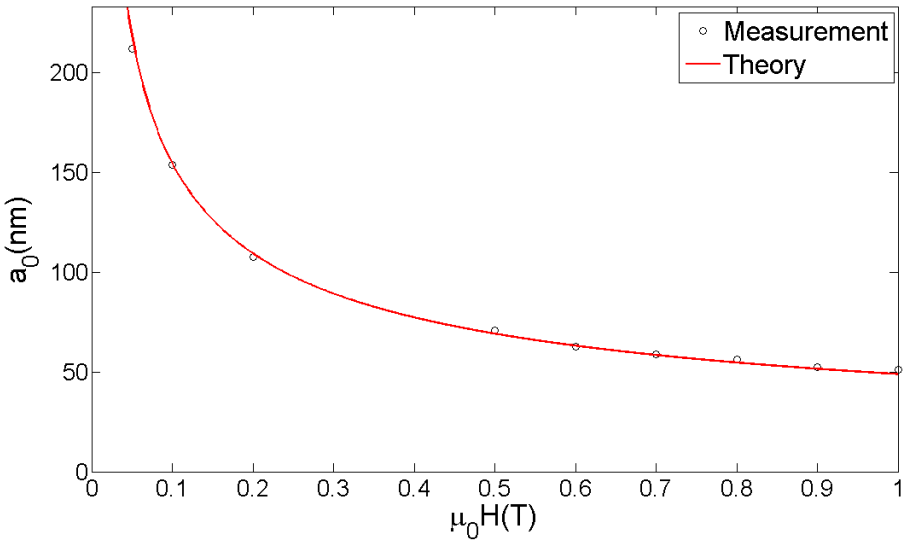

Fig. 5.1.1: Plot of the measured nearest neighbor distances and theory for the irradiated sample.

0.05 T Δa_0 is three times lower than the pixel size, therefore the value of a_0^{M} may indicates that theory and measurement do not match. Whereas at 0.7 T the value of Δa_0 is near zero, so theory and measurement agree.

Tab. 5.1.1 and Fig. 5.1.1* show, that theory values (a_0^{T}) and measurement values (a_0^{M}) agree relatively well, although there are small differences at low and high fields. Even if the deviations are small, it should be noted that in the second peak effect region the observed distance of the vortices is larger than according to theory, while at low fields, where the remanent magnetization is observed, the distance is lower. These regions also exhibit the most disordered lattice. That the vortex distance in the second peak region of the irradiated sample is larger than expected from theory is not the anticipated behavior. The anticipated behavior was that the vortex cores get closer together, as is the case at low fields. A possible explanation is, that the applied field $\mu_0 H$ is unequal to B in regions of high j_{c} (cf. Fig. 5.1.6(a)). This is particularly important at low fields.

A problem that was observed in some measurements, was that a tilted surface of the sample led to unequal nearest neighbor distances. E. g. if the slope in x-direction is 0 nm per 100 nm and the slope in y-direction is 10 nm per 100 nm, the value of

*The values of a_0^{M} were scaled with a factor 1.2895, to take into account the difference of the distance of the scanner and the theoretical value.

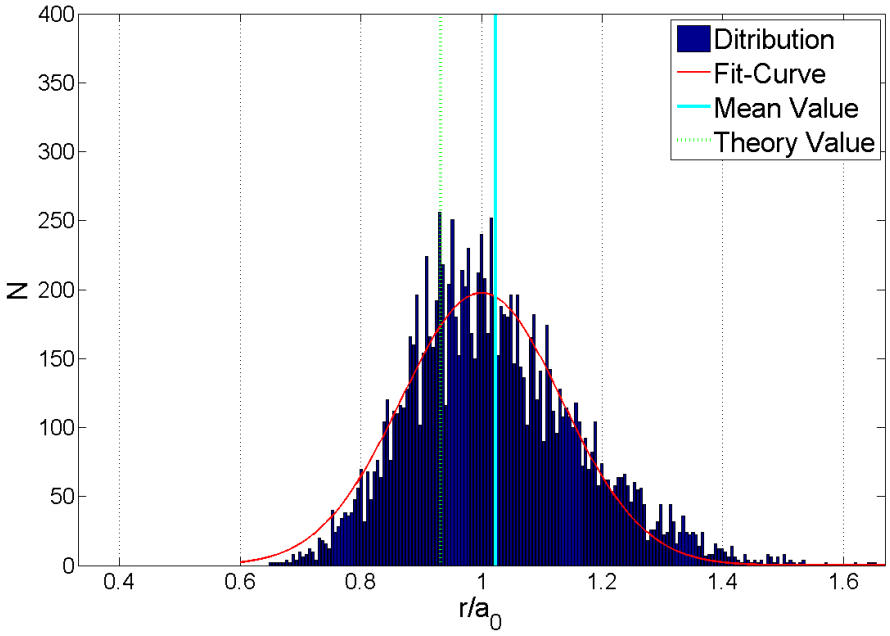

Fig. 5.1.2: Distribution of nearest neighbor distance (r) at a field of 0.9 T for the irradiated sample. The fit-curve is the Gauss function Eq. (4.3.4). The x-axis is normalized with the maximum value of the Gauss function. The theoretical value is a bit lower than the maximum value of the fit and the expectation value of the distribution of r is a bit larger.

the nearest neighbor distance in x-direction would be larger than in y-direction. A detailed study of this behavior was not made in this work, but it is suspected, that the slope and the inequality of x and y-direction are linked.

Another observation related to a_0 is, that the distribution of the nearest neighbor distance shows that a dislocation has the tendency to be farther away from the ideal lattice position at high fields (0.9 T), as seen in Fig. 5.1.2. The fit-curve is a Gauss function (Eq. (4.3.4)) that describes the expected distribution of r. For values smaller than the maximum of the fit curve the number of found vortices is distinctly lower than the Gauss fit. On the other hand more vortices are found with a greater distance to their nearest neighbors. As a consequence, the expectancy value is a bit above the maximum value

$$\langle r \rangle = \frac{\sum r_i N_i}{\sum N_i} \tag{5.1.1}$$

of the Gauss function.

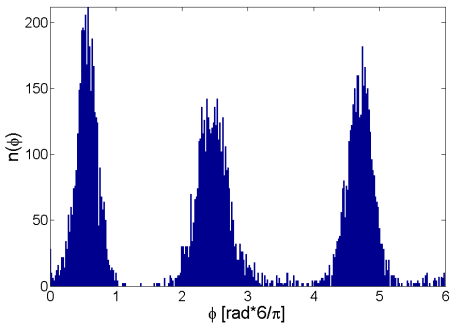

(a) Absolute angular distribution: 0.6 T

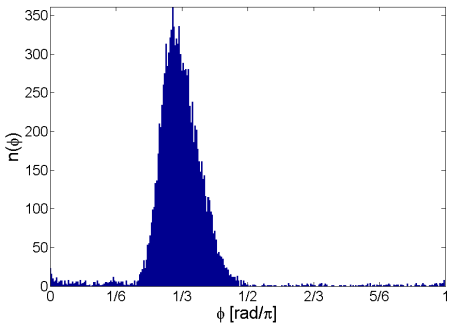

(b) Relative angular distribution: 0.6 T

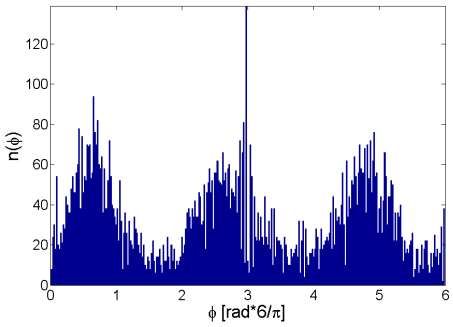

(c) Absolute angular distribution: 1.0 T

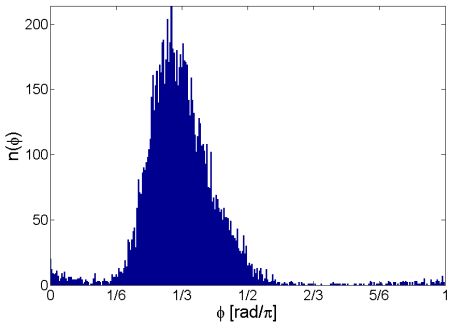

(d) Relative angular distribution: 1.0 T

Fig. 5.1.3: Distribution of the absolute angles compared to the x-axis and the relative distribution of the angle between nearest neighbors (i. e. the distribution of the included angles of the Delaunay diagram) for the irradiated sample.

The parameter ϕ which describes the angle between the x-axis and the orientation of the lattice is similar for all measured fields (about 20°). Fig. 5.1.3(a) and (c) show the distribution of the angles to the x-axis (only nearest neighbors were considered). (b) and (c) show the relative angular distribution, i. e. the distribution of the included angles of the Delaunay diagram. For an ordered hexagonal lattice the peaks are higher and narrower (0.6 T) than in the disordered case (1.0 T). The similar orientation of the lattice for different fields indicates that the vortices are aligned to border like structures in the sample, e. g. the sample borders or grain boundaries.

Fig. 5.1.4 indicates such an alignment as well. The image in Fig. 5.1.4(a) shows a step in the sample surface, that partly follows the vortex orientation. Fig. 5.1.4(b) is the z-scan of Fig. 5.1.4(a). The step has a magnitude of 1 to 1.5 nm, which is about the same size as the crystal lattice parameter c (1.25 nm). It is very likely, that only one triple layer (Se-Nb-Se; cf. Section 3.1) was “removed” at this location.

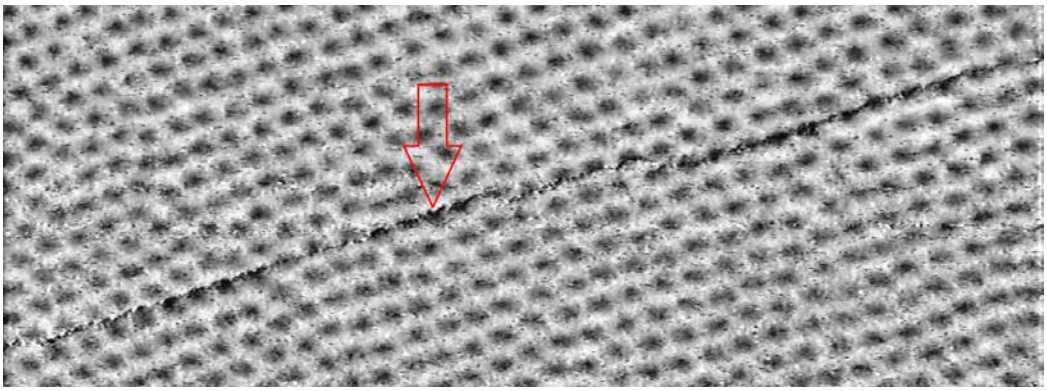

(a) Step of the sample surface observed in STS measurement. The vortices seem to be aligned at the step.

(b) z-scan of the same step as in Fig. 5.1.4. The step has the height of about 1 to 1.5 nm. (The unit cell lattice parameter in z-direction is $c = 1.25$ nm.)

Fig. 5.1.4: Observed alignment of vortices in $NbSe_2$ at 0.5 T in the irradiated sample.

Fig. 5.2.5 and 5.2.6 (page 72 and 73) display Voronoi diagrams at the measured fields in the irradiated sample. Each closed area shows the reciprocal unit cell of one vortex position at the center of this area. Defects are indicated by different symbols (and colors). A vortex with six nearest neighbors is assigned white in order to make the defects in the images more visible. In the field regions where the magnetization is not reversible (0.1, 0.9 and 1.0 T) the disorder of the lattice and the defects can be seen. At 0.1 T the number of vortex cores that form defects is 14 while the total number is 261, so about 5% of the vortices build up defects (defect density; see Fig. 5.1.6(b)). For a field of 0.9 T this value is 16% and at 1.0 T 21%. This is in agreement with j_c (or rather with the magnetization measurement). For the fields, where the j_c curve is (nearly) zero, a well ordered lattice is expected. The Voronoi diagrams confirm this assumption, although there are still defects found and if the

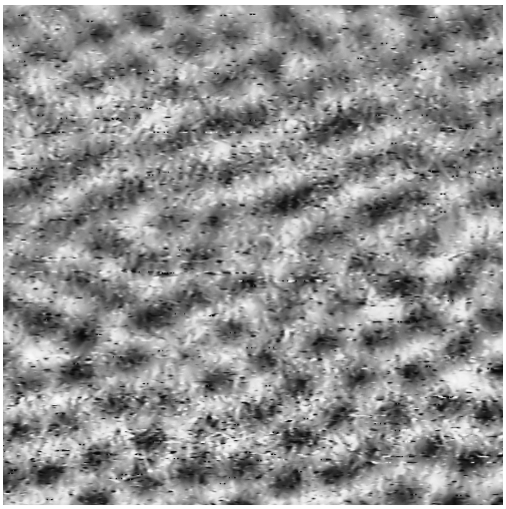

Fig. 5.1.5: "Merging" of vortices at a field of 1.0 T inthe irradiated sample

lattice is studied closely, the vortices are not that precisely aligned as in a pristine sample as can be seen in Fig. 5.2.7 on page 74 (refer also to Section 5.1.1).

At 1.0 T a region is found, where the vortices seem to merge along a certain lattice vector (see Fig. 5.1.5). This behavior could be observed more than once and the orientation of the "merging" was not always the same but pointed in different directions (e. g. once along the x-axis and another time along the y-axis; the scan lines were always measured in x-direction). In such regions it is very difficult to identify the positions of the individual vortex cores. This can be explained by the smaller distances between the vortex cores and therefore a lower contrast between normal conducting and superconducting areas in the lock-in signal (cf. Fig. 1.4.2).

In Fig. 5.1.6 the critical current density (j_c) is compared with the defect density and the fit parameter ξ_G of Eq. (5.2.1). The defect density was evaluated by summing up all vortex cores that have more or fewer neighbors than six and are not located at the border of the image.

The defect density shows good agreement with j_c, especially at high fields, where about 2000 vortices could be detected. Compared with j_c at 0.7 and 0.8 T the defect density shows a small increase that is not seen in j_c. At small fields (i. e. 0.05 and 0.1 T) too few vortices could be imaged to allow a good statistical statement. Still a slight increase of the defect density is observed at 0.1 T, but at 0.05 T only two defects could be found among a total number of 205 vortices, which results in a lower density than at 0.1 T and is not expected by theory.

The decay parameter ξ_G that describes the translation correlation length is also

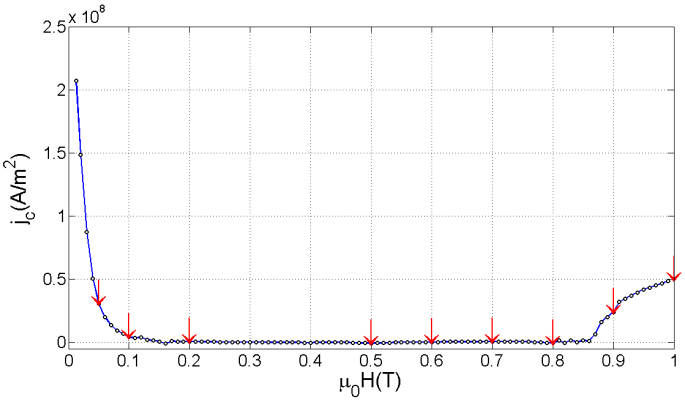

(a) j_c evaluation.

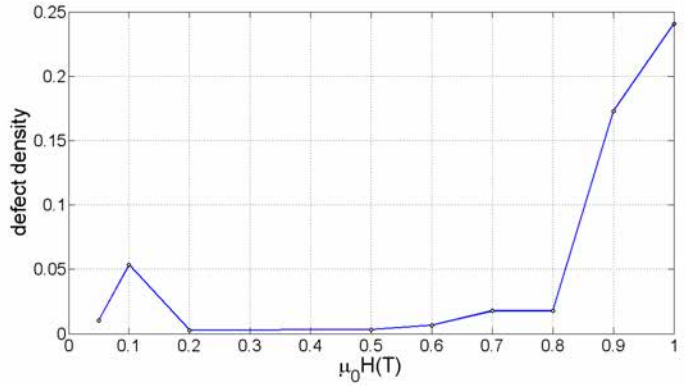

(b) Defect density: Number of vortices that are involved in defects divided by the number of all vortices.

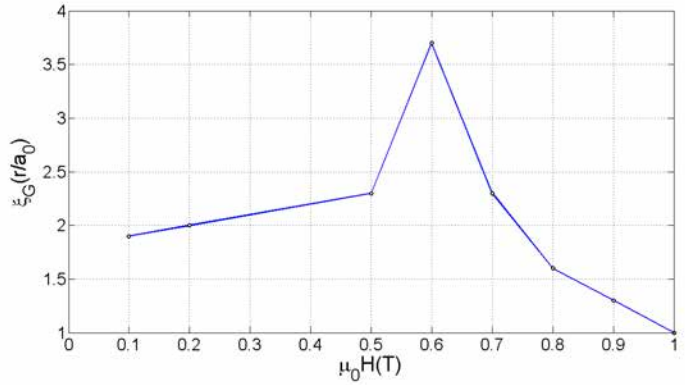

(c) Values of ξ_G in Fig. 5.2.4.

Fig. 5.1.6: Comparison of j_c with the defect density and the decay parameter ξ_G of the fit function (Eq. (5.2.1)) for the irradiated sample.

in good agreement with j_c, with the exception of the results at 0.6 T. The larger ξ_G the slower the translational order decays. Fig. 5.1.6(c) shows that at high j_c the value of ξ_G is small as was suspected, but at 0.8 T ξ_G seems smaller than we would suggest from j_c.

5.1.1 Evaluation of Lindemann Criterion

Tab. 5.1.2: Dependence of the standard deviation of the Gauss fit for the angular and the radial distribution of the vortex positions (σ_r and σ_α respectively), as well as the relative disorder of the combination of angular and radial part, Section 4.3.1 (Lindemann criterion; δ).

$\mu_0 H\,[T]$	σ_r	σ_α	σ_r/a_0	σ_α/α_0	δ
Irradiated Sample					
0.05	21.2243	0.1354	0.0913	0.1293	0.0945
0.1	16.4630	0.1605	0.0977	0.1533	0.1152
0.2	10.1823	0.1287	0.0865	0.1230	0.0900
0.5	7.6475	0.1386	0.0994	0.1324	0.1029
0.6	6.2834	0.1435	0.0914	0.1370	0.1020
0.7	6.5165	0.1569	0.1011	0.1498	0.1097
0.8	5.4497	0.1275	0.0880	0.1218	0.0944
0.9	6.9332	0.1916	0.1209	0.1830	0.1425
1.0	7.8694	0.2194	0.1407	0.2095	0.1543
Pristine Sample					
0.5	6.6003	0.0769	0.0638	0.0385	0.0560
1.0	4.9001	0.0949	0.0733	0.0475	0.0671

Tab. 5.1.2 shows that the relative disorder of the spatial distribution (σ_r/a_0) is higher than the angular part (σ_α/α_0) for every field. σ_r/a_0 at 0.1 T is not distinctively higher than at the fields where j_c is nearly zero, but in the radial part a clear rise of σ_α/α_0 is observed. At 0.7 T the disorder for the radial and angular distribution are larger than expected. A comparison with the values of ξ_G and the defect density (Section 5.2) shows, that this is not coincidental because the defect density also rises at this point. But the same is true for 0.8 T and at this value the relative disorder of the angular and radial distribution is one of the smallest. A possible explanation could be the relatively large pixel size of the image in relation to a_0. In Fig. 5.1.7 the values of Tab. 5.1.2 are plotted.

In the pristine sample the values of σ_r/a_0 and σ_α/α_0 are much lower than in

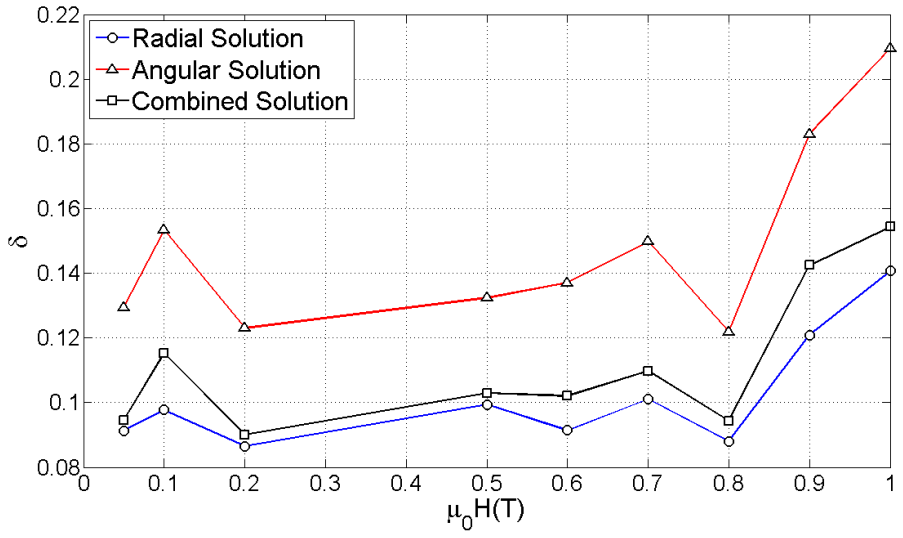

Fig. 5.1.7: Plot of the values in Tab. 5.1.2 (irradiated sample). Dependence of the standard derivation of the Gauss fit for the angular and the radial distribution of the vortex positions (σ_r and σ_α respectively), as well as the relative disorder of the combination of angular and radial part, Section 4.3.1 (Lindemann criterion; δ).

the irradiated sample. This indicates, that in spite of no observed macroscopic current in the SQUID measurement (i. e. the magnetization is reversible since the microscopic currents erase each other) the vortex cores are more dislocated in the irradiated sample to utilize the defects in an optimal way.

If Fig. 5.1.7 is compared with the critical current (Fig. 5.1.6(a)), where the second peak effect first occurs at 0.86 T, it is seen, that the Lindemann number has a magnitude of 0.13 at this field (combined solution). The vortex lattice transition number of approximately 0.2 as suggested in [33] was not reached in the combined solution for the Lindemann criterion.

5.2 Correlation Functions

In Fig. 5.2.1 the pair correlation functions at 0.5 to 1.0 T are imaged. The evaluated curves for the fields show good agreement between theory and experiment up to about three a_0, with the best agreement at 0.7 T, where a small step at $3a_0$ is visible. In general the lattices of the irradiated sample do not show such distinct peaks in $g(r)$ as the pristine sample. Thus the transversal correlation of the vortex lattice is higher in the pristine material (cf. Fig. 5.2.2).

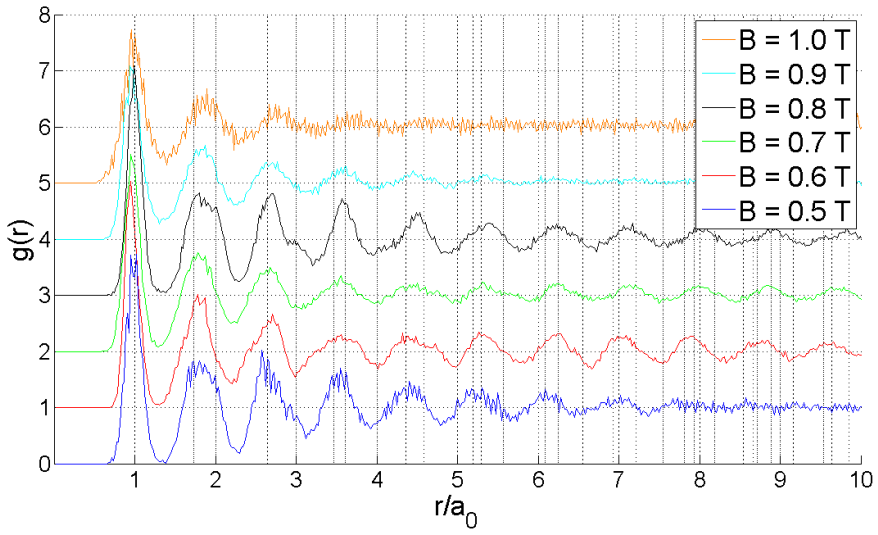

Fig. 5.2.1: Pair correlation functions from 0.5 to 1.0 T (from bottom to top) of the irradiated sample. Vertical lines indicate the distances in a perfect lattice. For increasing field values the curves were raised by one.

In both the irradiated and the pristine sample $g(r)$ has a periodic oscillating behavior, where lattice order dominates. The observed periodicity is not equal to a_0, but slightly lower. In a lattice with many defects (e. g. 1.0 T) this periodicity is no longer visible beyond about $3a_0$. The disappearance of the $g(r)$ periodicity is also observed at 0.7 and 0.5 T, which is not predicted because of the ordered vortex positions and the low value of j_c. At 0.5 T the oscillations vanish between 8 and $11a_0$. For distances greater than $11a_0$ the oscillations reoccur.

Fig. 5.2.2 displays the pair correlation of the pristine sample at 0.5 T. If this figure is compared with the 0.5 T curve of Fig. 5.2.1 (i. e. the irradiated sample) it is found, that the peaks are more pronounced. Especially the peak at a_0 nearly reaches the value of 6, which would be the value of a perfect lattice. While $g(r)$ of the irradiated sample hardly shows any separate peaks aside from the oscillating maxima, the pristine sample has separate peaks up to $10a_0$.

The orientation correlation functions shown in Fig. 5.2.3(a) describe the deviation of angles in the vortex lattice. The figure indicates that the long range order of C_6 is preserved for all field values except 1.0 T. The oscillations have a very low amplitude at 0.9 T but can by clearly seen in a scaled image (Fig. 5.2.3(b)), whereas they vanish at 1.0 T (Fig. 5.2.3(c)). Another difference between higher and lower field is that C_6 is lower at higher fields. At 0.5 to 0.8 T the value of C_6 at great

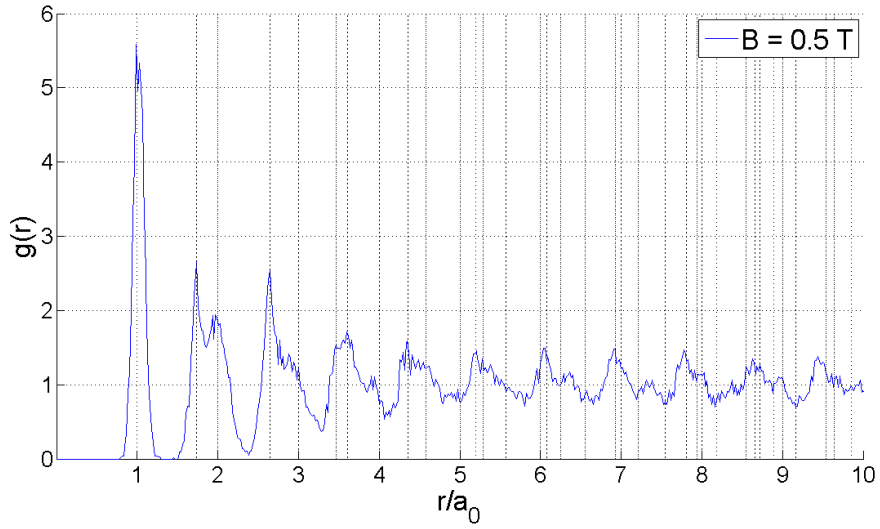

Fig. 5.2.2: Pair correlation functions at 0.5 T for the pristine sample. Vertical lines indicate the distances in a perfect lattice.

distances ($> 5a_0$) is above 0.5, while for 0.9 an 1.0 T it is beneath 0.5 (maximal value of C_6 is one for an ordered lattice).

The translation correlation functions of Fig. 5.2.4 were fitted with the exponential function

$$C_{\boldsymbol{G}}(r) = \mathrm{e}^{-r/\xi_{\mathrm{G}}} + c \tag{5.2.1}$$

where ξ_{G} denotes the decay of $C_{\boldsymbol{G}}$ and c is a constant to which the function converges. At 0.9 and 1.0 T, ξ_{G} has a smaller value than at lower fields, meaning that $C_{\boldsymbol{G}}$ decays more rapidly at 0.9 and 1.0 T as expected in a more disordered lattice. Although ξ_{G} varies for different fields, the constant c is approximately the same for all fields.

Long order oscillations in $C_{\boldsymbol{G}}$ are observed at 0.5 to 0.8 T, while at 0.9 and 1.0 T the oscillations vanish at a value of about $6a_0$ and $3a_0$, respectively. It should be noted, that the peaks in $C_{\boldsymbol{G}}$ do not correspond very well to the ideal lattice positions (vertical grid).

The fact, that at 0.9 T the orientation correlation function shows a long range order behavior while the translation correlation function has a shorter order, may indicate that the vortex lattice has a “hexatic” behavior. The “hexatic” state is characterized by the absence of a long range order in $C_{\boldsymbol{G}}$, but an appearance of

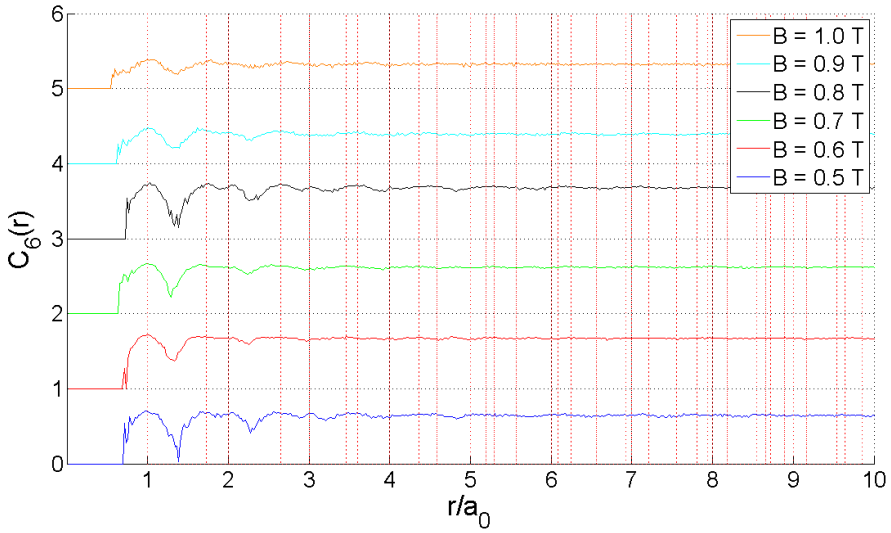

(a) Orientation correlation functions from 0.5 to 1.0 T (from bottom to top). Vertical lines indicate the distances of a perfect lattice. For increasing field values the curves were displaced by 0.5.

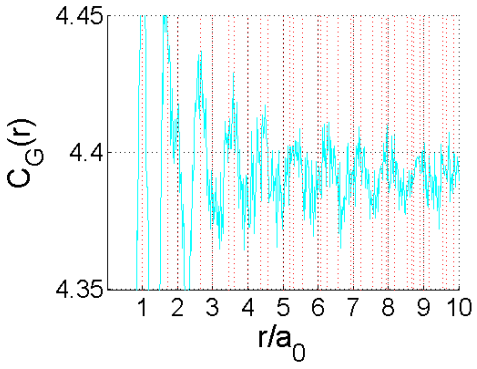

(b) 0.9 T scaled.

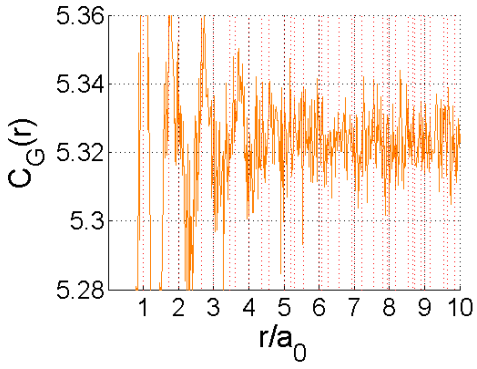

(c) 1.0 T scaled.

Fig. 5.2.3: Orientation correlation functions from 0.5 to 1.0 T for the irradiated sample.

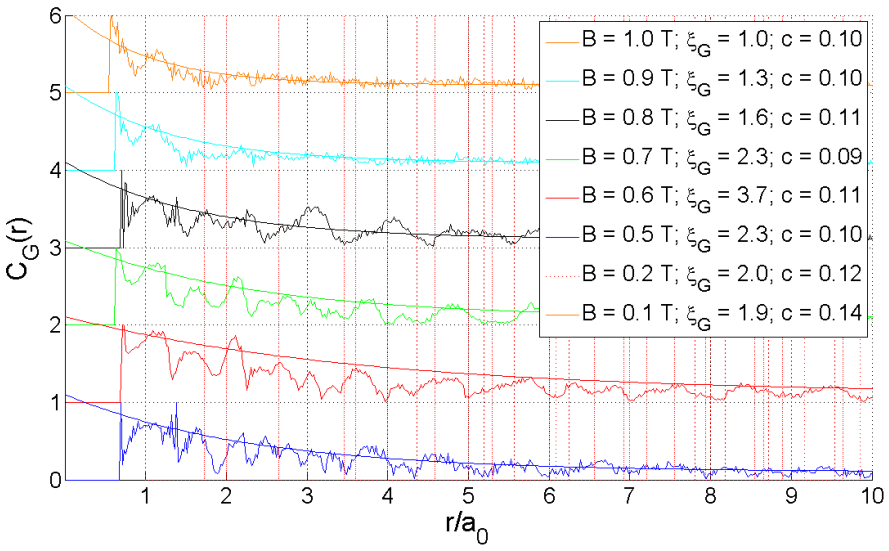

Fig. 5.2.4: Translation correlation functions from 0.5 to 1.0 T (from bottom to top) of the irradiated sample. Vertical lines denote the distances of a perfect lattice (Eq. (4.4.6)). For increasing field values the curves were displaced by 1.0. The results of the fit of Eq. (5.2.1) are also shown in the image. The values of the fit-parameters are given in the legend.

long order in C_6 [34] and is, for instance, found at the transition from a liquid to a solid state in many materials.

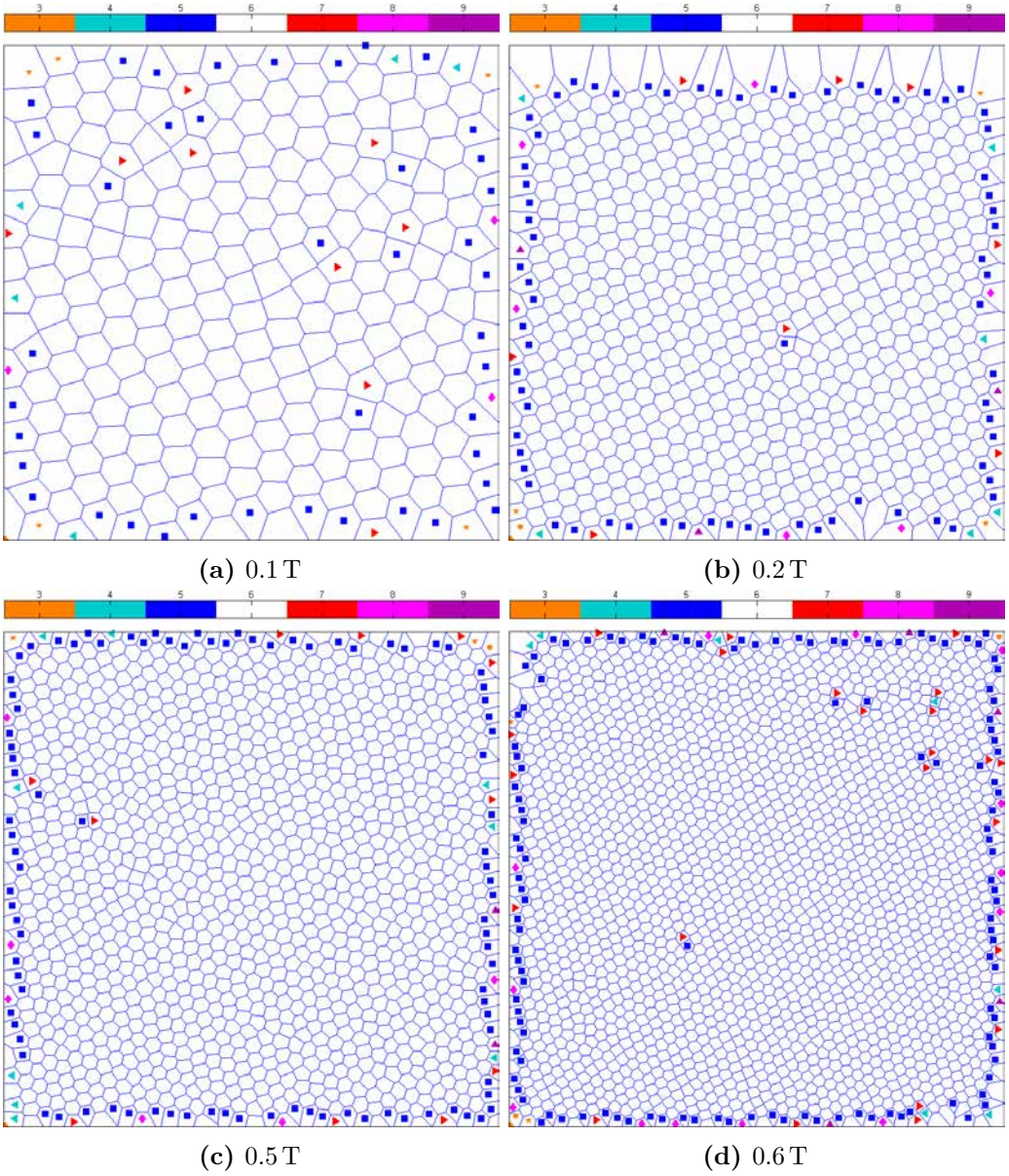

(a) 0.1 T **(b)** 0.2 T

(c) 0.5 T **(d)** 0.6 T

Fig. 5.2.5: Vortex lattice of an irradiated $NbSe_2$ sample. Each vortex sits in the center of a closed area. ◀ indicates four, ■ indicates five, ▶ indicates seven and ◆ indicates eight nearest neighbors. No symbol is shown for vortices with six neighbors.

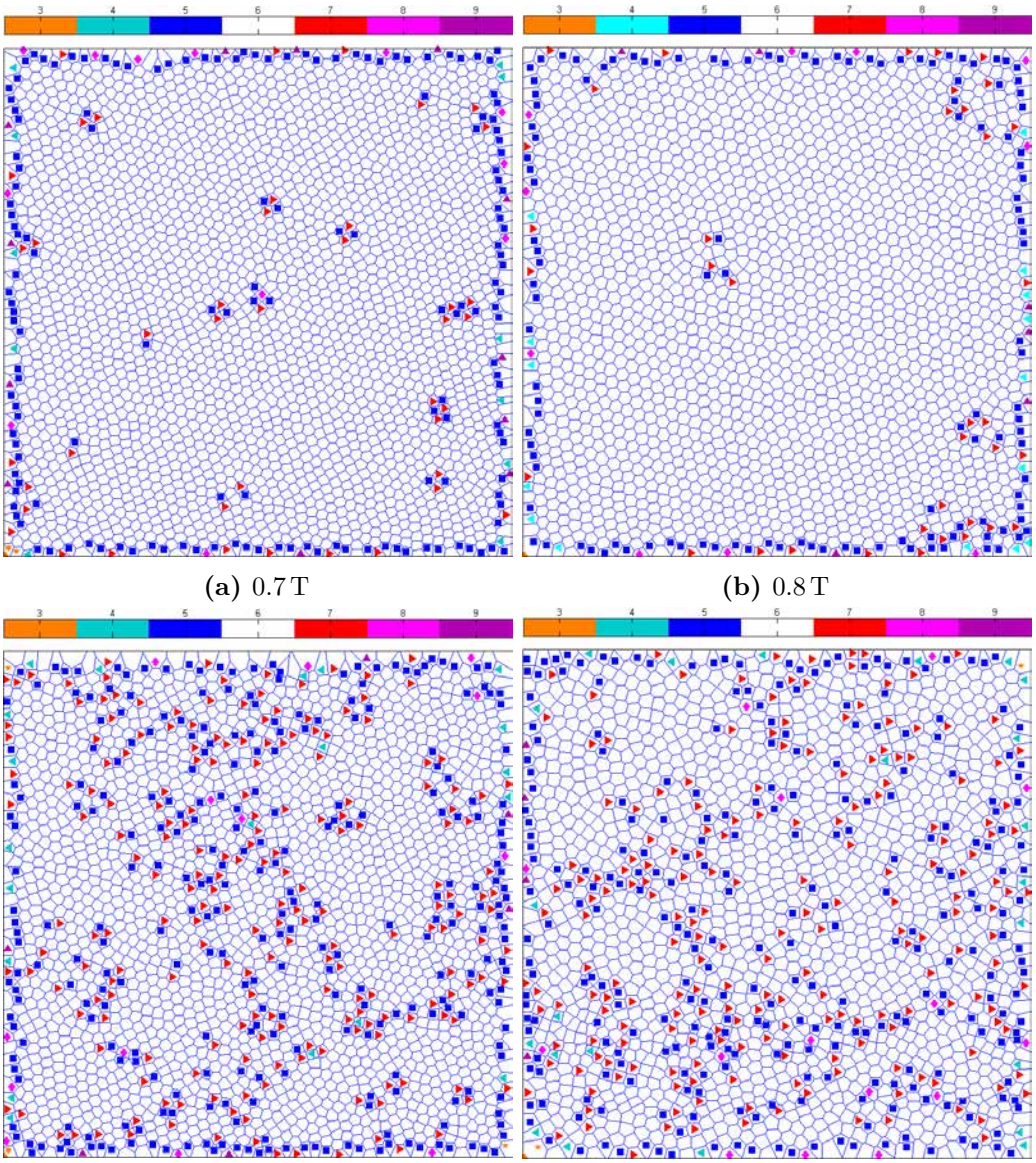

(a) 0.7 T **(b)** 0.8 T

(c) 0.9 T **(d)** 1.0 T

Fig. 5.2.6: Vortex lattice of an irradiated $NbSe_2$ sample. Each vortex sits in the center of a closed area. ◀ indicates four, ■ indicates five, ▶ indicates seven and ◆ indicates eight nearest neighbors. No symbol is shown for vortices with six neighbors.

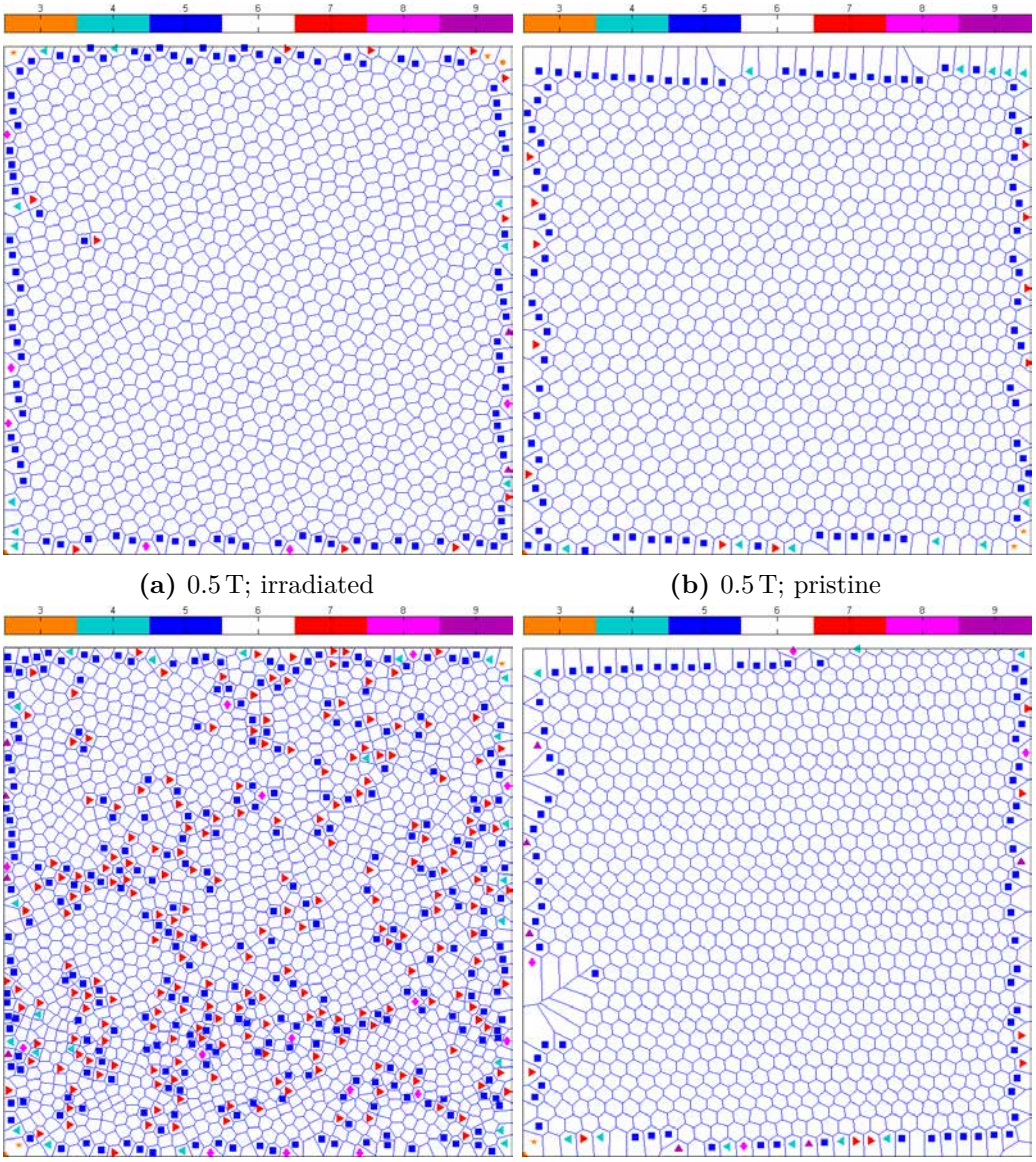

(a) 0.5 T; irradiated **(b)** 0.5 T; pristine

(c) 1.0 T; irradiated **(d)** 1.0 T; pristine

Fig. 5.2.7: Comparison of the Voronoi diagram at certain fields between pristine and irradiated sample.

6 Summary

In this work a study of the so-called flux vortex lattice of conventional type II superconductors was carried out. Various energies are responsible for the vortex matter behavior in a superconductor, most important are the vortex-vortex repulsion favoring an ordered vortex lattice and the pinning energy favoring a disordered lattice. Each energy dominates in a distinct area of the phase diagram. By exposing a sample to neutron irradiation material defects are introduced, which act as pinning centers for the vortices. An important effect is observed in neutron irradiated samples is the increase of the macroscopic critical current and in some cases the emergence of a second peak at high fields.

Scanning tunneling microscopy was used to detect vortices (i. e. the positions of the vortex cores) by recording the density of states over a scan area of up to $4 \times 4\,\mu\text{m}$. In this diploma thesis a C++ program was written allowing to controll the magnet power supply via a computer program. Aside from the control program of the power supply, algorithms for *MATLAB* were developed or integrated to process, filter and evaluate the scanning tunneling microscope data.

The sample chosen for this work was niobium diselenide ($NbSe_2$) because of a surface that is easy to prepare and very clean as well as smooth. The phase transition from the normal conducting to the superconducting phase occurs at a temperature of about 7 K and the upper critical field is about 4 T perpendicular and 12 T parallel to the Nb planes of the crystal. In this work one pristine and one irradiated sample (irradiation time: 220 min) were measured. The pristine sample was measured at 0.5 and 1.0 T, the irradiated sample at 0.05, 0.1 and 0.2 T, as well as from 0.5 to 1.0 T in 0.1 T steps.

To achieve a high statistical significance a large number of vortices were detected. We succeeded in imaging about 2000 vortex cores at high fields, a number much larger than reported in other papers [35], which allowed relatively well-founded statements on the correlations and other attributes of the lattice. The main focus was placed on the region, where the macroscopic critical current of the irradiated sample shows a second peak at a rather high magnetic field.

In order to get a more detailed understanding of the vortex lattice structure, and to compare theory and experiment, the correlation functions, the defect density and the critical current in the irradiated sample were examined. Correlation functions (e. g. pair, translation and orientation correlation functions) help to find the behavior of variables that describe the lattice.

In the second peak region of the irradiated sample the correlation functions indicate a highly disordered vortex lattice, while in regions where the macroscopic current vanishes the lattice was found to be rather well ordered. In the pristine sample the vortex lattice was found to be close to perfectly ordered. The pair correlation function of the irradiated sample showed an oscillating behavior in the region of a remanent magnetization, but did not have as distinct peaks as the pristine sample in the same region.

The lattice defect density showed the same behavior as the critical current density, namely an increase in the region of macroscopic critical currents. The correlation length showed a decrease in this region.

Additionally a study of the nearest neighbor distance was made. This study showed relatively good agreement between the theoretical and measured distances of the nearest neighbors. Another observation made in this work was that the angle between an axis (e. g. x-axis) and the orientation of the lattice is similar at all fields, which indicates an alignment of the vortices with border like structures in the sample, e. g. the sample borders or grain boundaries.

The evaluation of the Lindemann criterion was realized by looking at the angular and the spatial distribution of the relative vortex displacement as well as a combination of both. The results showed that at the onset of the second peak region, associated with the order disorder transition of the vortex lattice, the relative vortex displacement increases strongly, indicating a Lindemann number of roughly 0.12.

References

[1] D. van Delft and P. Kes, *Physics Today* **63**, 38 (2010).

[2] Autor unbekannt, *Skriptum* (Jahr unbekannt).

[3] H. Eschrig, (2008).

[4] G. Hilscher, H. Michor, and M. Reissner, *Skriptum* (2009).

[5] H. W. Weber and O. Hittmair, *Supraleitung*, Karl Thiemig, München, 1979.

[6] Wikipedia, General information on various chapters.

[7] M. Zehetmayer, *Skriptum* (2011).

[8] W. Meissner and R. Ochsenfeld, *Naturwissenschaften* **21**, 787 (1933), 10.1007/BF01504252.

[9] F. London and H. London, *Proceedings of the Royal Society of London. Series A, Mathematical and Physical Sciences* **149**, pp. 71 (1935).

[10] V. L. Ginzburg, *Nobel Lecture* (2003).

[11] L. N. Cooper, *Phys. Rev.* **104**, 1189 (1956).

[12] J. Bardeen, L. N. Cooper, and J. R. Schrieffer, *Phys. Rev.* **108**, 1175 (1957).

[13] C. J. Chen, *Introduction to scanning tunneling microscopy*, Number 2, Oxford University Press, 1993.

[14] T. Fauster, Scanning Tunneling Microscopy (STM).

[15] E. Meyer, H. J. Hug, and R. Bennewitz, *Scanning Probe Microscopy*, Springer-Verlag, 2004.

[16] G. Binnig and H. Rohrer, *Rev. Mod. Phys.* **59**, 615 (1987).

[17] G. Binnig and H. Rohrer, *Rev. Mod. Phys.* **71**, S324 (1999).

[18] H. F. Hess, R. B. Robinson, R. C. Dynes, J. M. Valles, and J. V. Waszczak, *Phys. Rev. Lett.* **62**, 214 (1989).

[19] J. S. Villarrubia, R. D. Young, F. Scire, E. C. Teague, and J. W. Gadzuk, *National Institute of Sandards and Technology* .

[20] W. Demtröder, *Experimentalphysik 3*, Springer, 2006.

[21] H. Lin, J. M. C. Rauba, K. S. Thygesen, K. W. Jacobsen, M. Y. Simmons, and W. A. Hofer, *Front. Phys. China* **5**, 369 (2010).

[22] J. Bardeen, *Phys. Rev. Lett.* **6**, 57 (1961).

[23] O. Fischer, M. Kugler, I. Maggio-Aprile, C. Berthod, and C. Renner, *Rev. Mod. Phys.* **79**, 353 (2007).

[24] J. Tersoff and D. R. Hamann, *Phys. Rev. B* **31**, 805 (1985).

[25] J. Tersoff and D. R. Hamann, *Phys. Rev. Lett.* **50**, 1998 (1983).

[26] I. Giaever, *Phys. Rev. Lett.* **5**, 147 (1960).

[27] I. Giaever, *Phys. Rev. Lett.* **5**, 464 (1960).

[28] B. M. Murphy, An X-ray diffraction investigation of the charge density wave transition at the $NbSe_2$ surface, 2003.

[29] M. Marz, Spektroskopische Untersuchungen an Supraleitern mittels Punktkontaktspektroskopie und Rastertunnelmikroskopie, 2009.

[30] M. Zehetmayer and H. W. Weber, *Phys. Rev. B* **82**, 014524 (2010).

[31] C. Trauner, Einfluss künstlicher Verankerungszentren auf das Flusslinien-gitter von V_3Si Einkristallen, 2010.

[32] P. D. Kovesi, MATLAB and Octave Functions for Computer Vision and Image Processing, Centre for Exploration Targeting, School of Earth and Environment, The University of Western Australia.

[33] J. Kierfeld and V. Vinokur, *Phys. Rev. B* **69**, 024501 (2004).

[34] M. V. Marchevsky, *Magnetic Decoration Study of the Vortex Lattice in Superconductors*, 1997.

[35] M. Iavarone, R. Di Capua, G. Karapetrov, A. E. Koshelev, D. Rosenmann, H. Claus, C. D. Malliakas, M. G. Kanatzidis, T. Nishizaki, and N. Kobayashi, *Phys. Rev. B* **78**, 174518 (2008).

A Appendix

All measurements were carried out at 4.22 K.
Space values were scaled with a factor 1.2895, to take into account the difference of the distance of the scanner and the theoretical value.
Values divided by 100 indicate the use of a voltage divider.
The following lock-in settings were used for all measurements:

Frequency: 12215.545 Hz
Time constant: 100 ms
Amplitude: 11 mV/100
Sensitivity: 5 mV

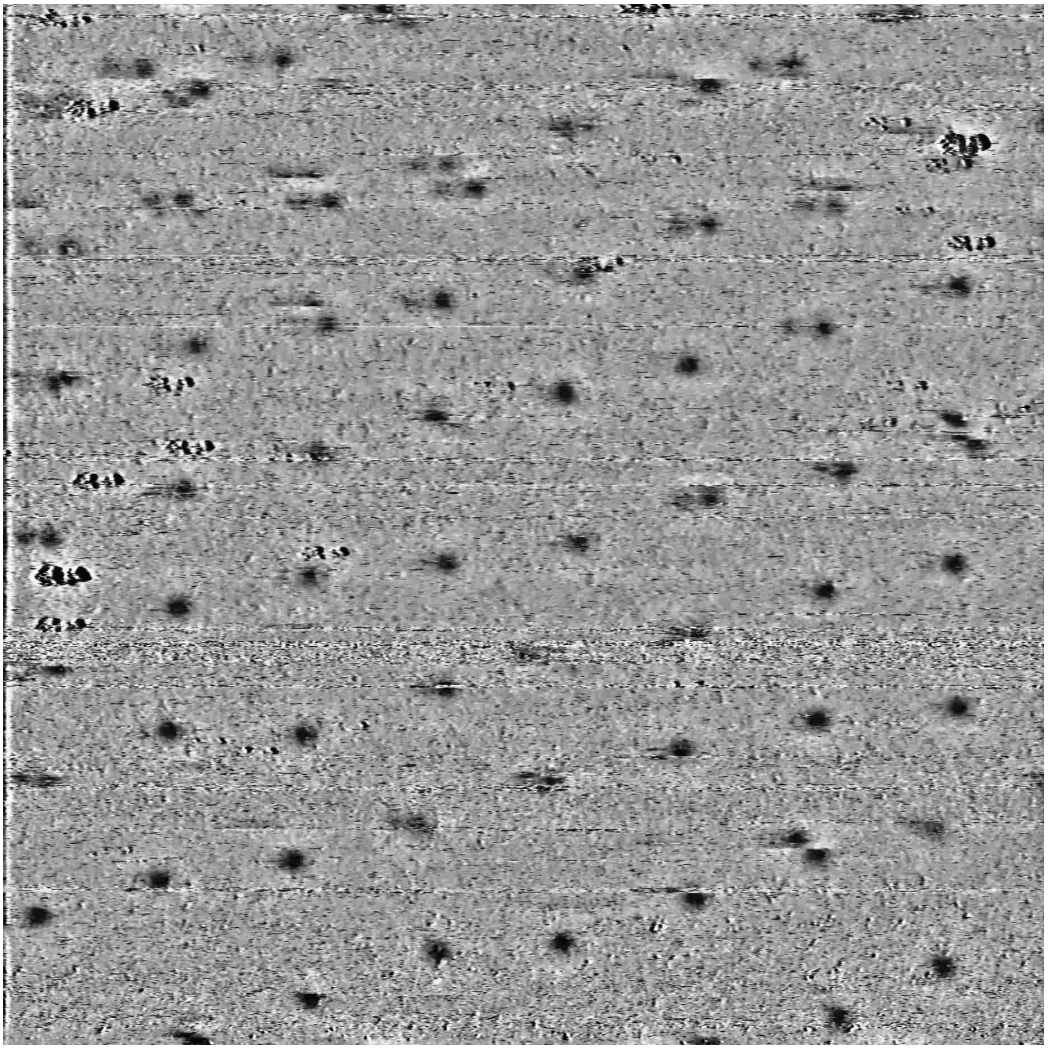

Fig. A.1:
Field: 0.0 T
Range: $2.87 \times 2.87\,\mu m^2$
Pixel size: 1.55 nm
Sample time: 30 ms
P | I: 1 m | 1.5 Hz
Tunneling current: 500 pA
Bias voltage: -60 mV/100

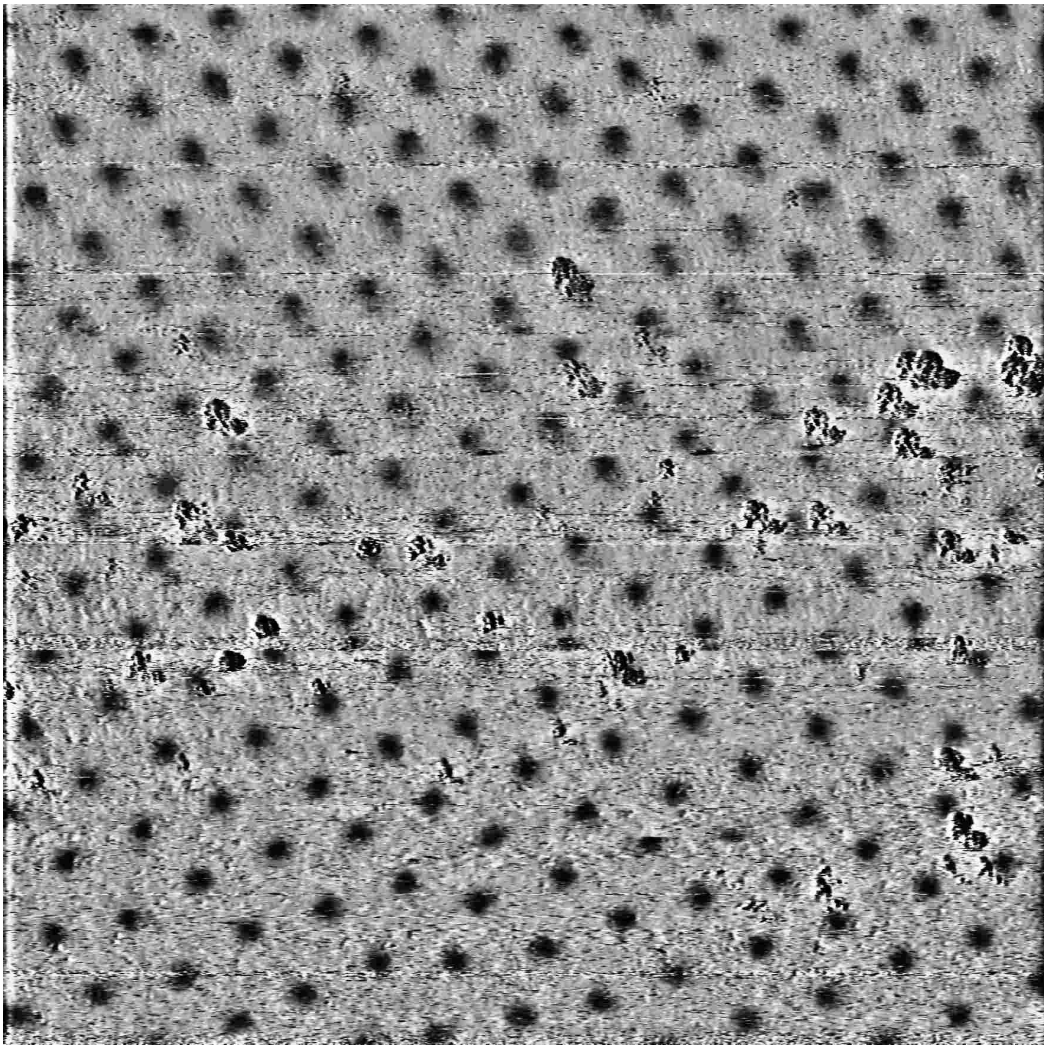

Fig. A.2:
Field: 0.05 T
Range: $2.87 \times 2.87\,\mu m^2$
Pixel size: 1.63 nm
Sample time: 35 ms
P | I: 1 m | 1.5 Hz
Tunneling current: 500 pA
Bias voltage: -60 mV/100

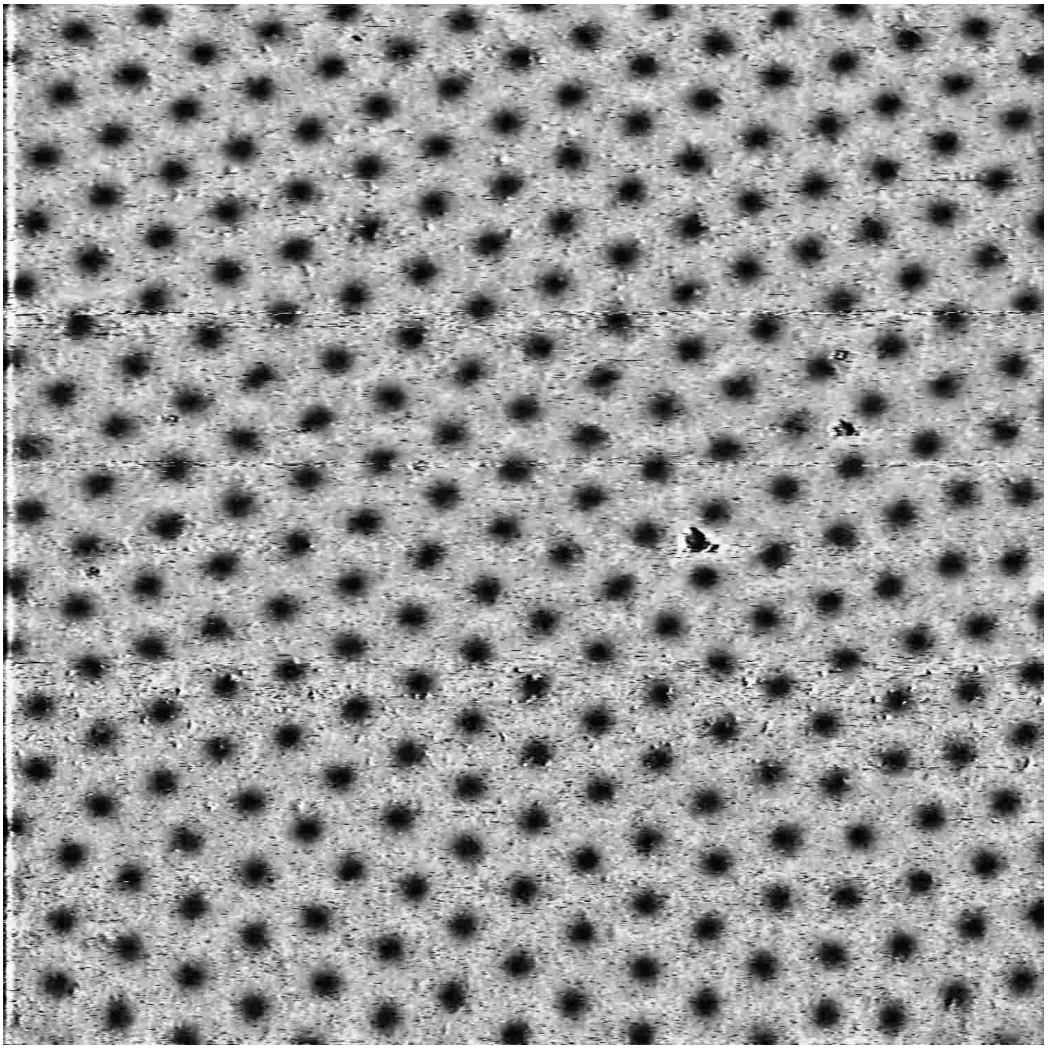

Fig. A.3:
Field: 0.1 T
Range: $2.33 \times 2.33\,\mu m^2$
Pixel size: 1.55 nm
Sample time: 25 ms
P | I: 1 m | 1.5 Hz
Tunneling current: 500 pA
Bias voltage: -60 mV/100

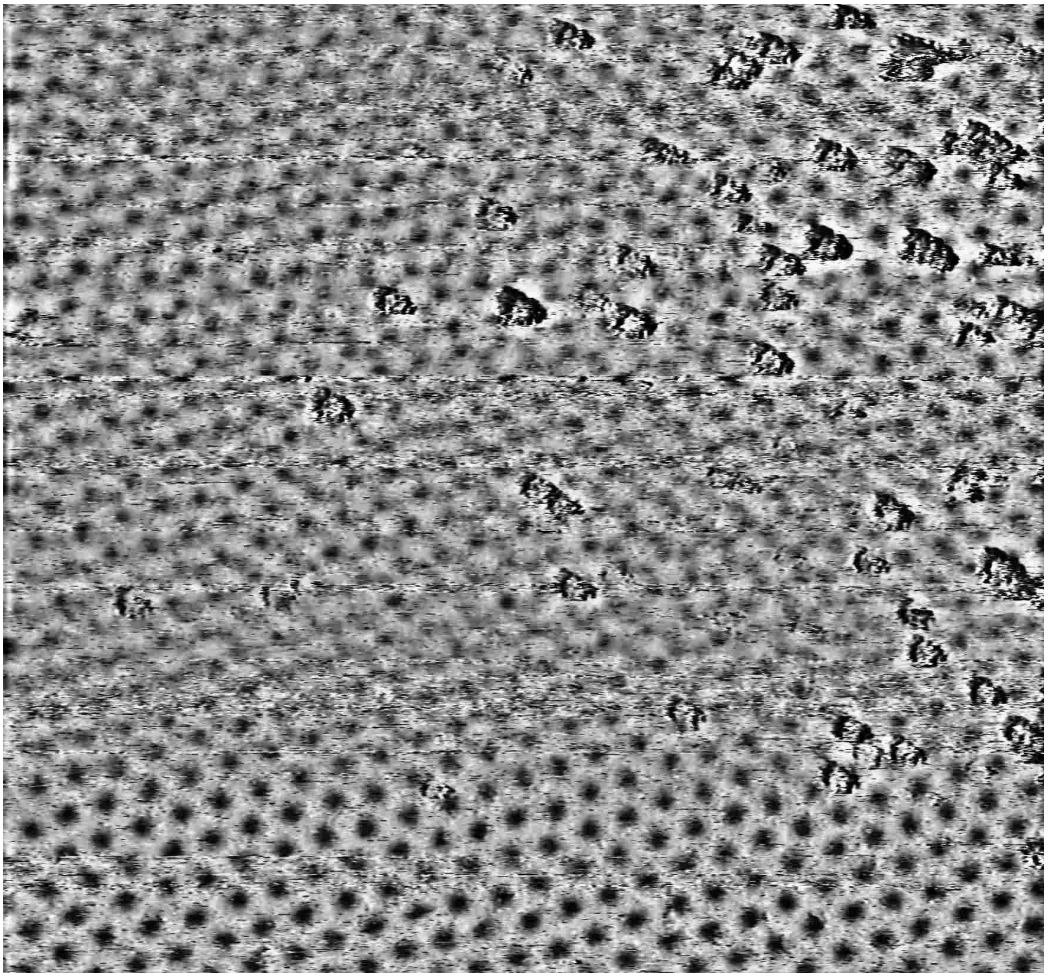

Fig. A.4:
Field: 0.2 T
Range: $2.87 \times 2.87\,\mu m^2$
Pixel size: 1.63 nm
Sample time: 30 ms
P | I: 1 m | 1.5 Hz
Tunneling current: 500 pA
Bias voltage: -60 mV/100

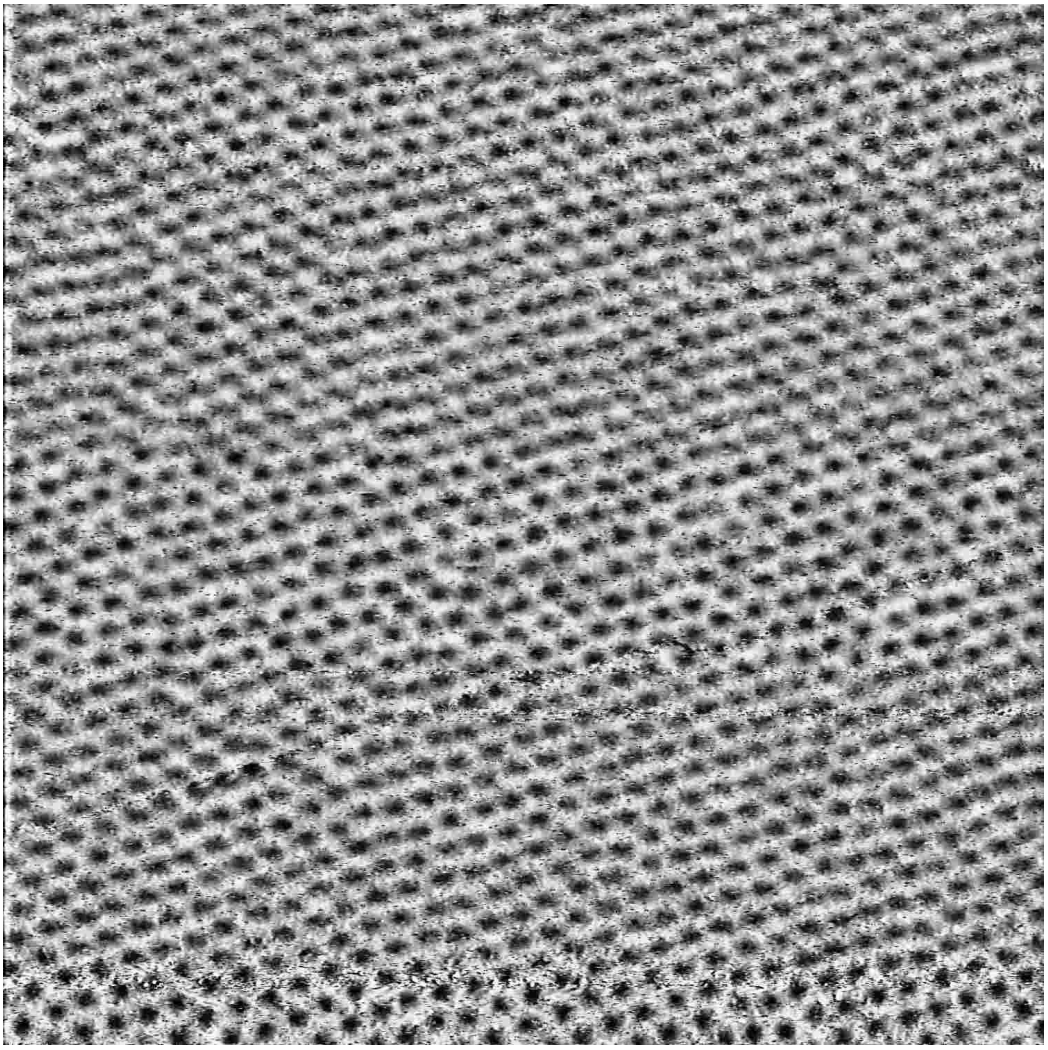

Fig. A.5:
Field: 0.5 T
Range: $1.16 \times 1.16\,\mu m^2$
Pixel size: 1.55 nm
Sample time: 50 ms
P | I: 1 m | 1 Hz
Tunneling current: 500 pA
Bias voltage: -70 mV/100

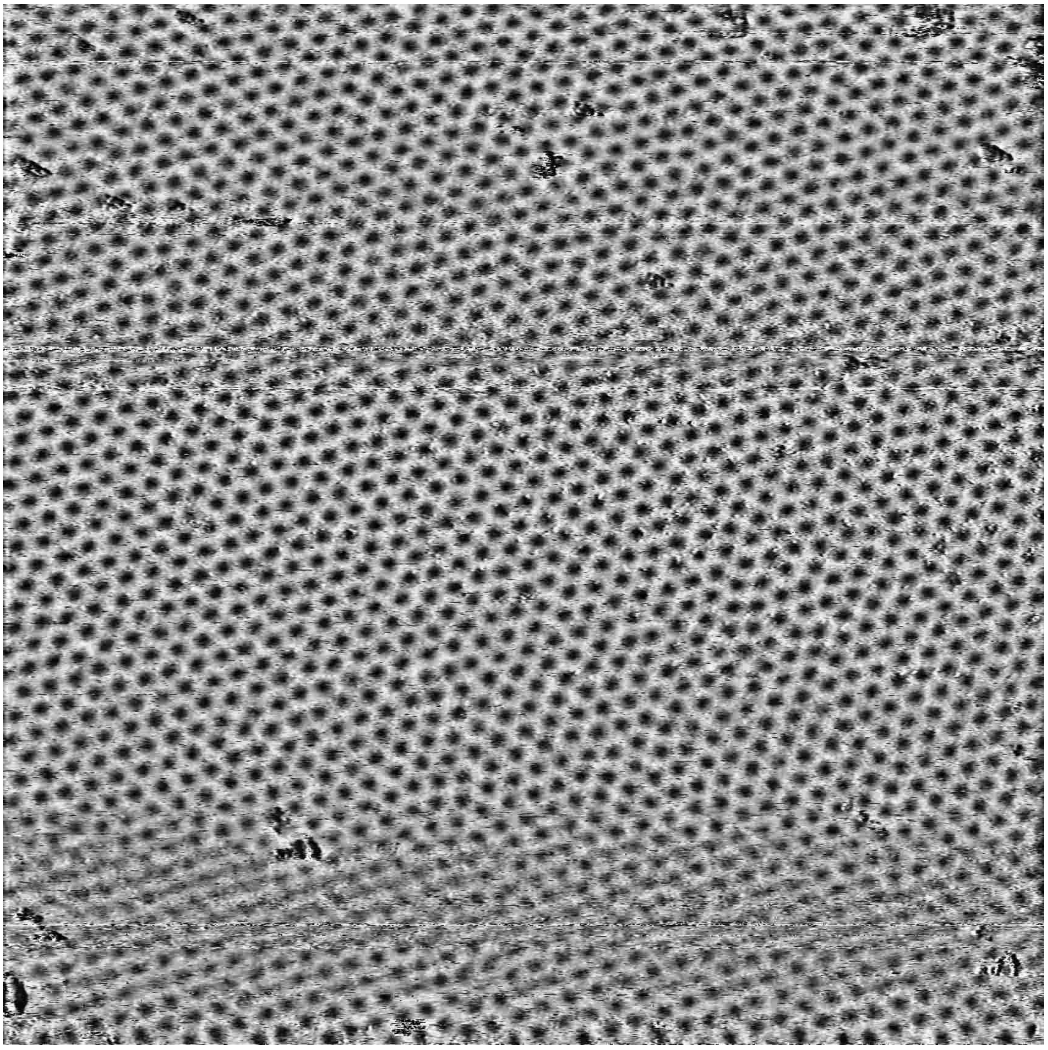

Fig. A.6:
Field: 0.6 T
Range: $2.64 \times 2.64\,\mu m^2$
Pixel size: 1.55 nm
Sample time: 40 ms
P | I: 1 m | 1.5 Hz
Tunneling current: 500 pA
Bias voltage: -80 mV/100

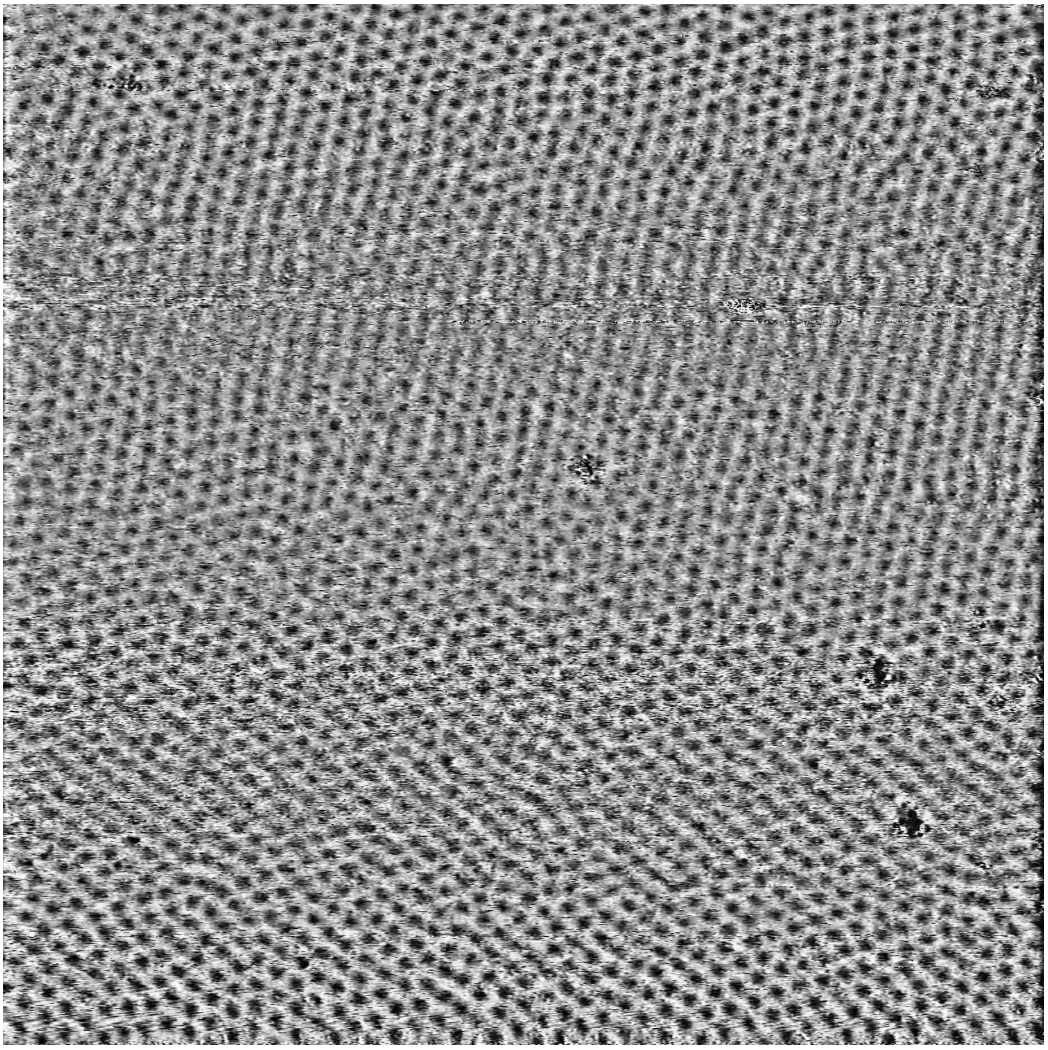

Fig. A.7:
Field: 0.7 T
Range: $2.71 \times 2.71\,\mu m^2$
Pixel size: 1.47 nm
Sample time: 40 ms
P | I: 1 m | 1.5 Hz
Tunneling current: 500 pA
Bias voltage: -80 mV/100

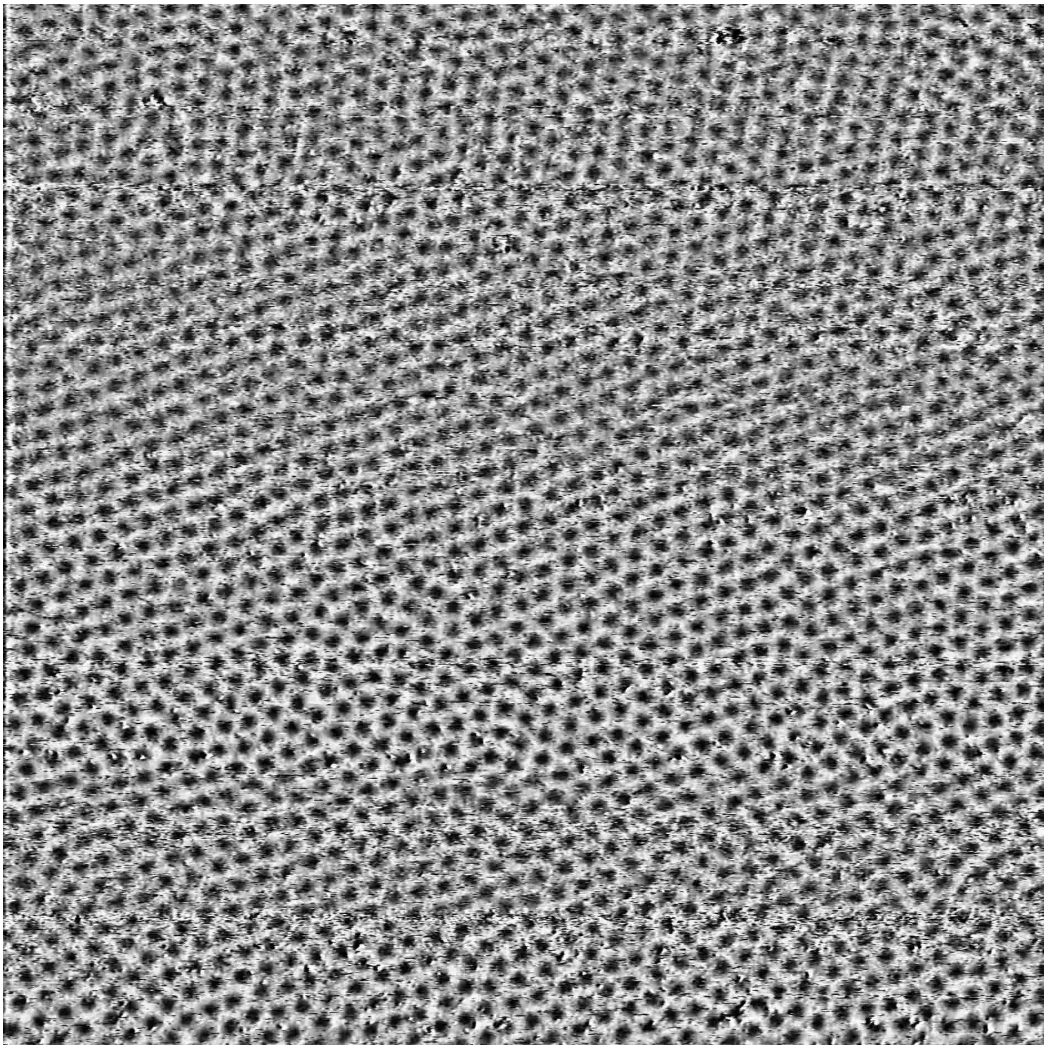

Fig. A.8:
Field: 0.8 T
Range: $2.33 \times 2.33\,\mu m^2$
Pixel size: 1.24 nm
Sample time: 37 ms
P | I: 1 m | 2 Hz
Tunneling current: 500 pA
Bias voltage: -60 mV/100

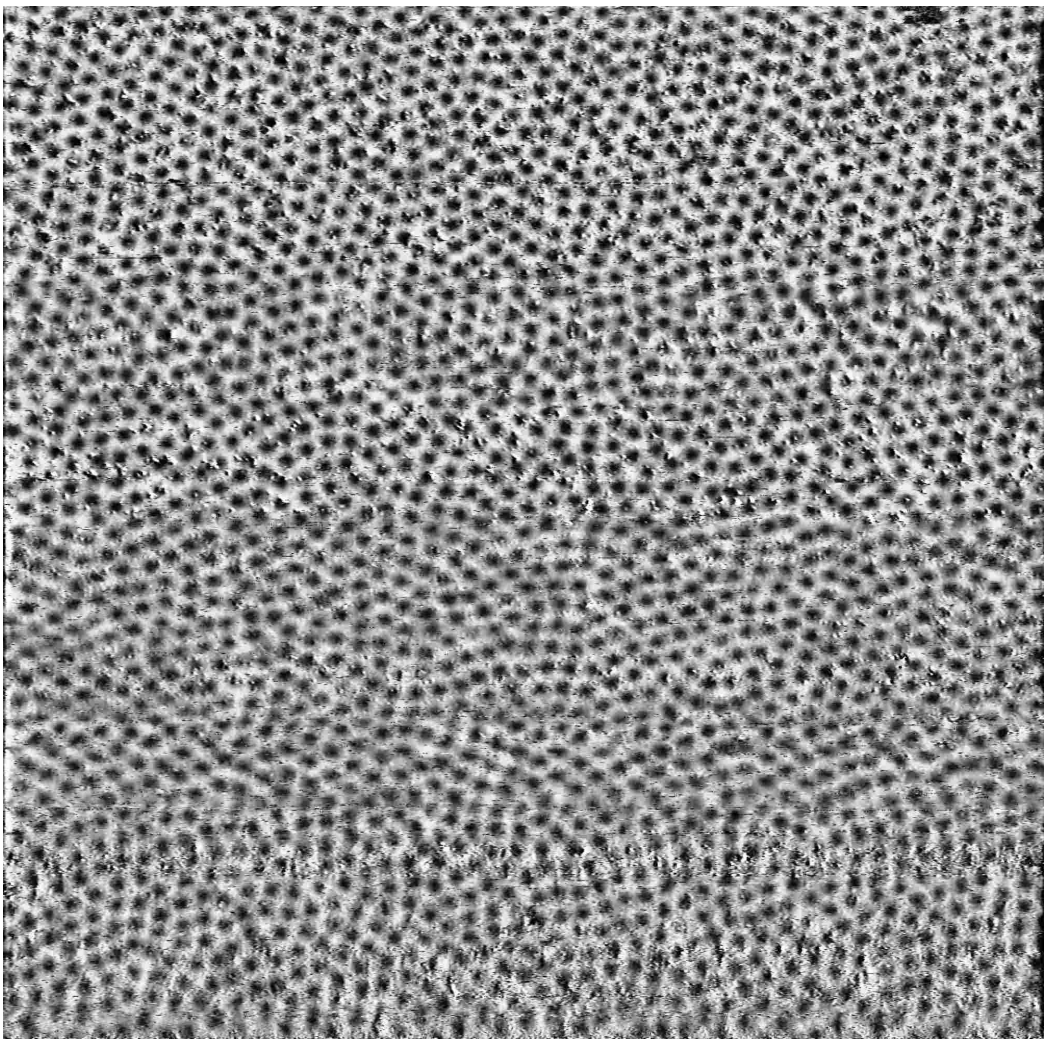

Fig. A.9:
Field: 0.9 T
Range: $2.33 \times 2.33\,\mu m^2$
Pixel size: 1.16 nm
Sample time: 40 ms
P | I: 1 m | 1 Hz
Tunneling current: 500 pA
Bias voltage: -80 mV/100

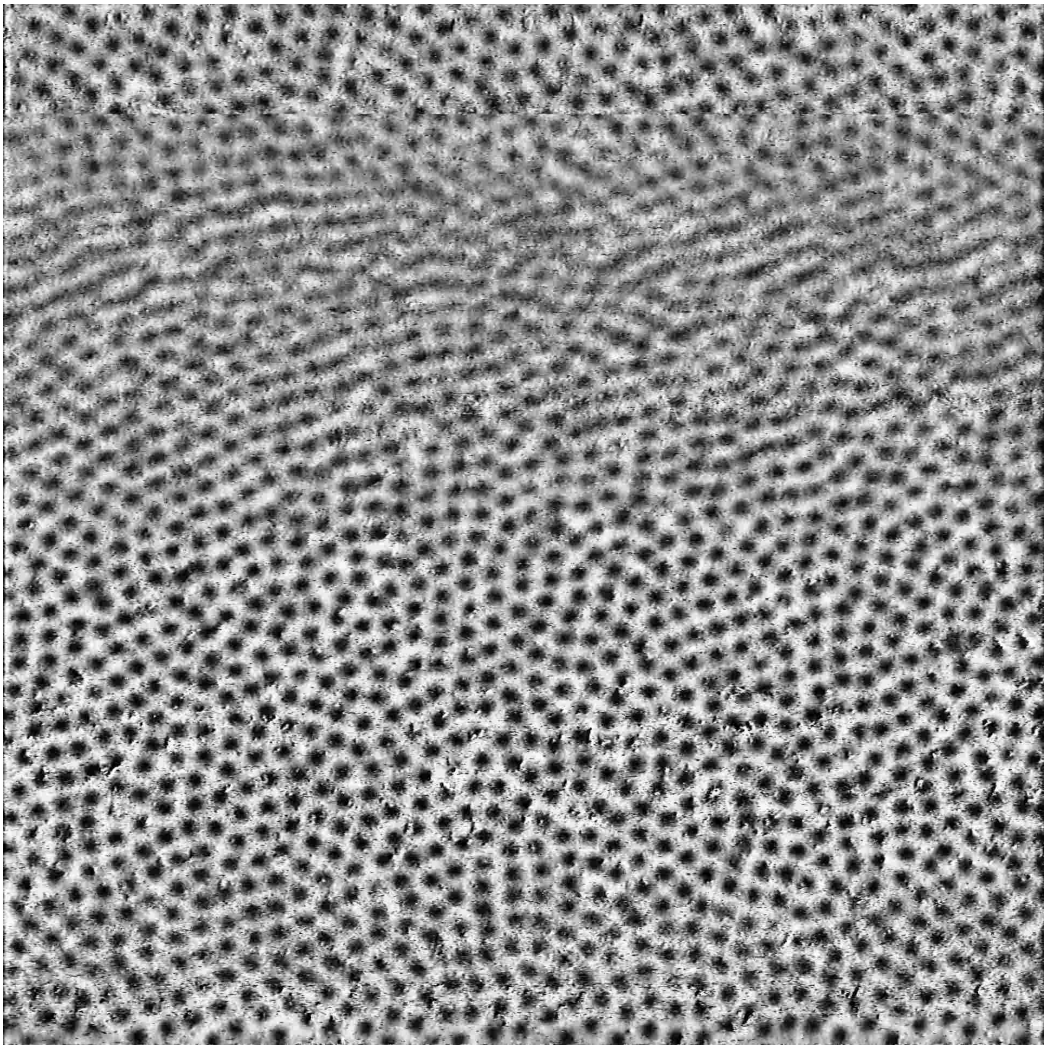

Fig. A.10:
Field: 1.0 T
Range: $1.94 \times 1.94\,\mu m^2$
Pixel size: 1.01 nm
Sample time: 50 ms
P | I: 1 m | 1 Hz
Tunneling current: 500 pA
Bias voltage: -80 mV/100

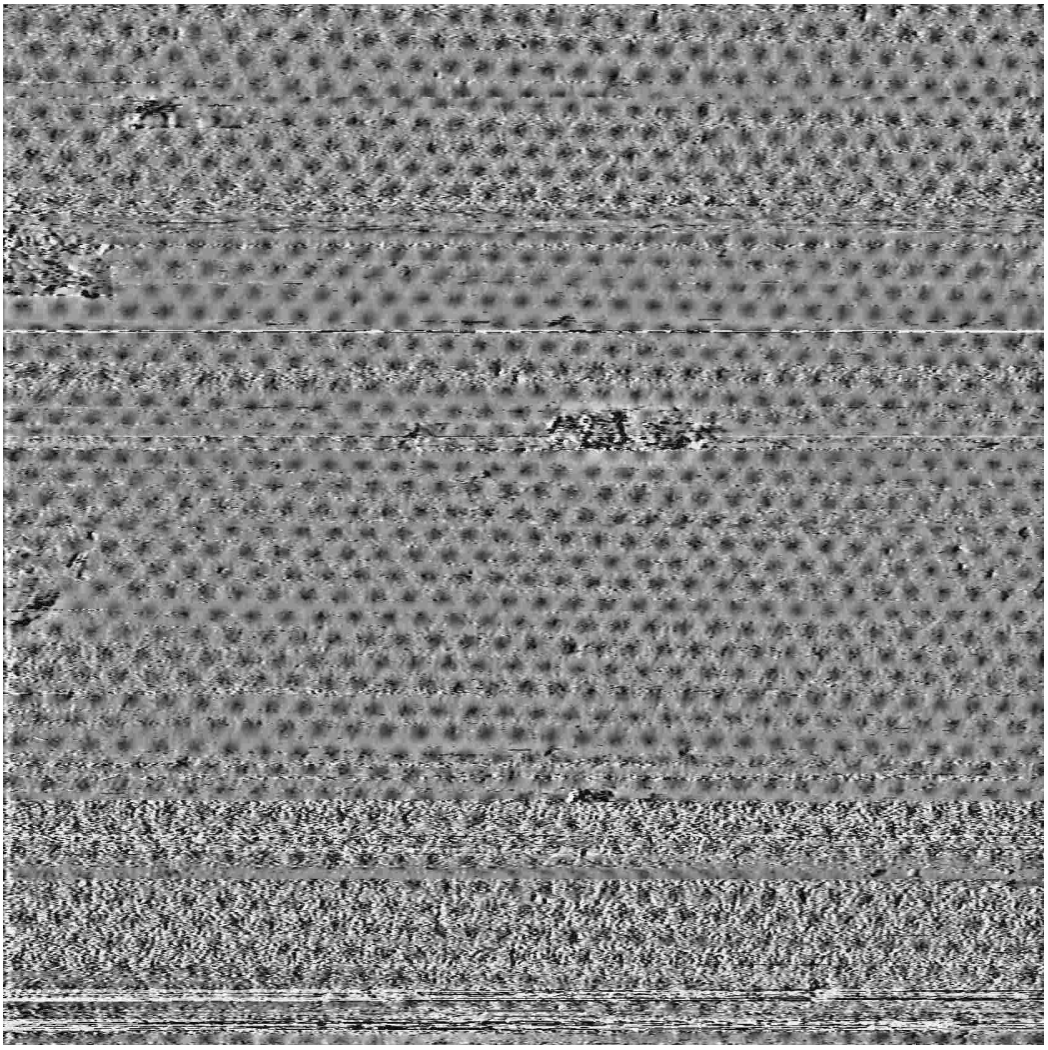

Fig. A.11: Pristine sample
Field: 0.5 T
Range: $1.94 \times 1.94\,\mu m^2$
Pixel size: 1.16 nm
Sample time: 35 ms
P | I: 1 m | 3 Hz
Tunneling current: 500 pA
Bias voltage: -80 mV/100

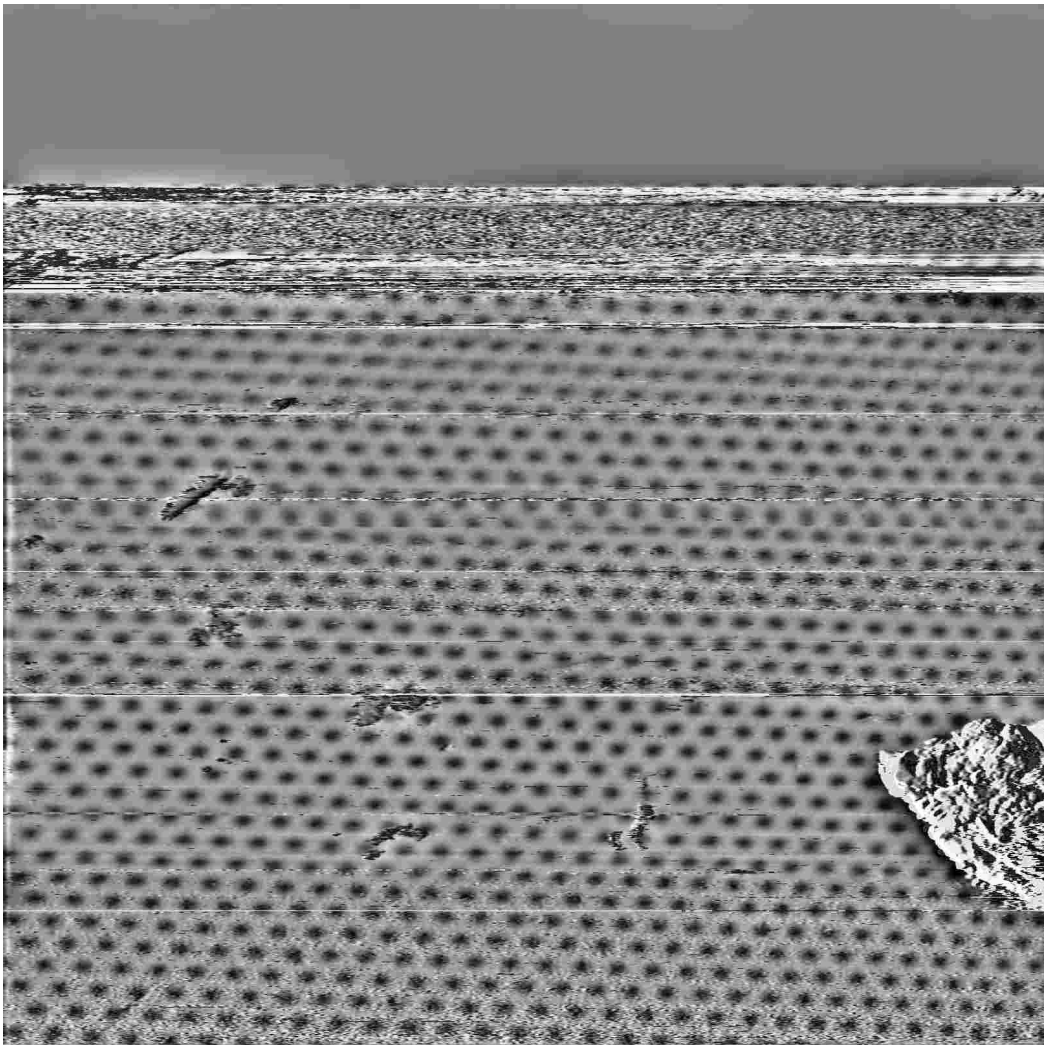

Fig. A.12: Pristine sample
Field: 1.0 T
Range: $2.84 \times 2.84\,\mu m^2$
Pixel size: 1.78 nm
Sample time: 40 ms
P | I: 1 m | 3 Hz
Tunneling current: 500 pA
Bias voltage: -80 mV/100

Acknowledgments

Some persons have to be mentioned here without whom this work would not have been written:*

Most importantly I want to thank DDr. Harald Weber, who first inspired me to engage myself in superconductivity and who showed much patience with a student who was not always on schedule. Many thanks!

Another person important for this work was Martin Zehetmayer, who was always at hand when he was needed (and he was needed often) and with whom working was very enjoyable.

Of course I have to thank my family, especially my parents for their backup and my brother for his "IT related support".

Finally, I want to thank my physic friends and all my other friends for some great years.

And lastly, thanks to all those great physicist, who did and do an excellent job in making my life interesting (some I may have mentioned earlier).

*Unfortunately, only I did the writing.